2001

Subthreshold Photoionization in Molecular Dopant/Perturber Systems.

Cherice Marie Evans
Louisiana State University and Agricultural & Mechanical College

INFORMATION TO USERS

This manuscript has been reproduced from the microfilm master. UMI films the text directly from the original or copy submitted. Thus, some thesis and dissertation copies are in typewriter face, while others may be from any type of computer printer.

The quality of this reproduction is dependent upon the quality of the copy submitted. Broken or indistinct print, colored or poor quality illustrations and photographs, print bleedthrough, substandard margins, and improper alignment can adversely affect reproduction.

In the unlikely event that the author did not send UMI a complete manuscript and there are missing pages, these will be noted. Also, if unauthorized copyright material had to be removed, a note will indicate the deletion.

Oversize materials (e.g., maps, drawings, charts) are reproduced by sectioning the original, beginning at the upper left-hand corner and continuing from left to right in equal sections with small overlaps.

Photographs included in the original manuscript have been reproduced xerographically in this copy. Higher quality 6" x 9" black and white photographic prints are available for any photographs or illustrations appearing in this copy for an additional charge. Contact UMI directly to order.

ProQuest Information and Learning
300 North Zeeb Road, Ann Arbor, MI 48106-1346 USA
800-521-0600

UMI®

SUBTHRESHOLD PHOTOIONIZATION IN MOLECULAR DOPANT/PERTURBER SYSTEMS

A Dissertation

Submitted to the Graduate Faculty of the
Louisiana State University and
Agricultural and Mechanical College
in partial fulfillment of the
requirements for the degree of
Doctor of Philosophy

in

The Department of Chemistry

by
Cherice Marie Evans
B.S., University of Louisiana at Monroe, 1996
M.S., University of Louisiana at Monroe, 1998
May, 2001

Acknowledgments

I would like to thank Dr. John D. Scott, my Major Professor, for his guidance, support and encouragement throughout this work. I also wish to express my appreciation to Dr. Gary L. Findley, who served as my research advisor.

Dr. Ruben Reininger graciously provided equipment and supplies (NSF CHE-9506508), as well as needed encouragement and insight when difficulties arose. Dr. Fred H. Watson and Dr. Eizi Morikawa provided many stimulating discussions. Finally, I would like to thank Dr. Hartmut Höchst and the staff of the University of Wisconsin Synchrotron Radiation Center for their many kindnesses, and for maintaining the endstation that was used in this work.

All of the measurements presented here were carried out at the University of Wisconsin Synchrotron Radiation Center (NSF DMR 98-31009) in Stoughton, WI. This work was supported by a grant to G. L. Findley from the Louisiana Board of Regents (LEQSF (1997-00)-RD-A-14). Special thanks are also extended to the Louisiana State University Center for Advanced Microstructures and Devices for providing me with a research assistantship for the duration of this project, and to the LSU Department of Chemistry.

Table of Contents

Acknowledgments ii

Abstract v

Chapter 1. Introduction 1

Chapter 2. Rydberg States of Atoms and Molecules 4
A. Introduction 4
i. Rydberg States 4
ii. Generation of Rydberg Molecules 8
B. Photoabsorption 9
C. Photoionization 13

Chapter 3. Perturber Effects on Rydberg States 15
A. Perturber-induced Energy Shifts 16
i. The Fermi Model 16
ii. Impact Approximation 18
iii. Polarization Distribution Model 22
B. Spectral Broadening 24
C. Subthreshold Photoionization Mechanisms 25
i. Collisional Ionization 26
ii. Rotational and Hot-band Autoionization 26
iii. Electron Attachment 28
iv. Associative Ionization 30
v. Other Mechanisms 32

Chapter 4. Experiment 33
A. Experimental Apparatus 33
i. Monochromator and Endstation 33
ii. Sample Cells 35
iii. Gas Handling System 36
B. Sample Preparation 37
C. Dopant and Perturber Information 40
D. Data Acquisition and Analysis 41

Chapter 5. Electron Scattering Lengths of Fluorinated Compounds 44
A. Introduction 44
B. Electron Scattering Length of Ar [14] 46
C. Electron Scattering in Fluorinated Gases 48
i. CF_4 [15] 48
ii. c-C_4F_8 [15] 49
iii. SF_6 [16] 51
D. Summary of Results 52

Chapter 6. Subthreshold Photoionization 54
A. Introduction 54
B. Electron Scattering Lengths of Fluorinated Gases 56
C. Temperature Studies 60
D. Photochemical Rearrangement 64
E. Density Studies [14,17-20] 65
i. C_2H_5I [14,20] 69
ii. C_6H_6 [14,20] 73
iii. CH_3I [17-20] 78
F. Summary of Results 100

Chapter 7. Conclusion 102

References 106

Appendix 1. Energy Positions of High-*n* Rydberg States 119
A. Photoabsorption and Autoionization [14-16] 119
B. Subthreshold Photoionization [14,17] 121

Appendix 2. Exponential Background Data from Subthreshold Photoionization 124
A. Regression Coefficients 124
B. Area of Exponential Background 125

Appendix 3. Subthreshold Photoionization Peak Areas 126
A. C_2H_5I/SF_6 [14,20] 126
B. C_6H_6/SF_6 [14,20] 128
C. CH_3I/P 131
i. CH_3I/Ar [18,20] 131
ii. CH_3I/CF_4 [19] 133
iii. CH_3I/CO_2 and N_2 [18] 135
iv. $CH_3I/c\text{-}C_4F_8$ [19] 136
v. CH_3I/SF_6 [17,20] 138

Vita 141

Abstract

The use of atomic and molecular Rydberg states to investigate dopant/perturber interactions is a well established research area. In this Dissertation, photoionization spectroscopy is used to probe the interactions between various dopants (D = CH_3I, C_2H_5I and C_6H_6) and perturbers (P = Ar, N_2, CO_2, CF_4, *c*-C_4F_8 and SF_6) in a static gas-phase system. One overall goal is a better understanding of the nature of dopant/perturber interactions in the gas phase which, in turn, can lead to a better understanding of solvation in the condensed phase.

Two separate perturber effects are investigated in this work: the perturber-induced energy shift of high-*n* dopant Rydberg states, and the appearance of photoionization structure below the first dopant ionization threshold (i.e., subthreshold photoionization) in some dopant/perturber systems. From the perturber-induced energy shifts, the zero-kinetic-energy electron scattering lengths and cross-sections of Ar, CF_4, *c*-C_4F_8 and SF_6 are evaluated. (To the best of our knowledge, this represents the first experimental determination of the zero-kinetic-energy electron scattering lengths of CF_4 and *c*-C_4F_8, and the first determination of the zero-kinetic-energy electron scattering length of SF_6 using the shift of dopant high-*n* Rydberg states.)

The appearance in various dopant/perturber systems of subthreshold photoionization structure, which tracks the absorption of discrete dopant Rydberg states in the same energy region, is reported and analyzed. This subthreshold photoionization structure is explained by invoking two separate pathways, both of which involve the excited-state processes of electron attachment and associative ionization. From the measurements reported here, subthreshold photoionization in C_2H_5I/SF_6 and C_6H_6/SF_6 is shown to proceed through

electron attachment to SF_6, and through the formation of heteromolecular dimers. Subthreshold photoionization in CH_3I/P is shown to proceed through electron attachment to CH_3I and to the perturber, and through the formation of both homomolecular and heteromolecular dimers.

Finally, the effective rate constants for these processes are determined from the variation in the subthreshold photocurrent as a function of dopant number density ρ_D and perturber number density ρ_P. These constants are then analyzed with respect to the properties of the excited dopant Rydberg state. For the dopant CH_3I, the variation in the effective rate constants is discussed in terms of ground-state perturber properties (such as electron affinity and polarizability).

Chapter 1. Introduction

Rydberg states are highly sensitive to the "environment" (where environment implies an external electric or magnetic field, or perturber molecules) and, therefore, Rydberg atoms and molecules have been used extensively as interaction probes [1-10]. In this Dissertation, dopant/perturber interactions are investigated by observing the effects of a perturber on dopant Rydberg states using photoabsorption and photoionization spectroscopy. Two separate perturber effects are examined: perturber-induced energy shifts of dopant Rydberg states, and the appearance of subthreshold photoionization in some dopant/perturber systems. One overall goal of this study is to gain a better understanding of certain gas-phase molecular interactions that can yield new insights into molecular solvation and clustering in condensed-phase systems.

Since this work focuses on the interaction of molecular Rydberg states with perturber atoms and molecules, a brief discussion of Rydberg states, along with a description of techniques used to generate and study these states, is presented in Chapter 2. Of the techniques mentioned in Chapter 2, however, only photoabsorption and photoionization are reviewed in detail, since these are the methods employed in the research reported here.

In Chapter 3, a description of different types of perturber effects is presented. This description begins with a review of the various theoretical models [5,6,11-13] developed to explain perturber-induced energy shifts of discrete high-n dopant Rydberg states. Chapter 3 then continues with a brief discussion of spectral broadening and concludes with an explanation of some of the mechanisms which can lead to subthreshold photoionization in dopant/perturber systems.

A detailed description of the experimental apparatus used throughout this work is given in Chapter 4, along with information about the dopants and perturbers employed. This chapter also includes a discussion of the procedures applied in correcting and analyzing the data presented here.

In Chapter 5, the perturber-induced energy shifts of dopant high-n Rydberg states are used to evaluate the zero-kinetic-energy electron scattering lengths and cross-sections of Ar [14], CF_4 [15], c-C_4F_8 [15] and SF_6 [14,16,17]. To the best of our knowledge, these measurements represent the first experimental determination of the zero-kinetic-energy electron scattering lengths of CF_4 and c-C_4F_8, and the first evaluation of the zero-kinetic-energy electron scattering length of SF_6 from high-n dopant Rydberg states.

Chapter 6 provides a more detailed investigation of subthreshold photoionization, which is the primary focus of this work. Following a brief review of subthreshold photoionization mechanisms, the subthreshold photoionization structure of CH_3I in the presence of various perturbers, and that of C_2H_5I and C_6H_6 in the presence of SF_6, is shown to arise from high-n Rydberg states by the evaluation of the zero-kinetic-energy electron scattering lengths of CF_4, c-C_4F_8 and SF_6 from the perturber-induced energy shifts of this subthreshold structure, and by the demonstration that these scattering lengths agree well with those obtained in Chapter 5 from the photoabsorption and autoionization spectra of the same dopant/perturber systems.

Next, a temperature study of the subthreshold photoionization structure in the chosen dopant/perturber systems is presented. From this study, the mechanisms of hot-band and rotational autoionization are dismissed as possible explanations for the observed subthreshold structure. Furthermore, the mechanisms of collisional transfer of translational energy from the perturber to the excited-state dopant, and photochemical rearrangement

producing charged products, are ruled out on the basis of energetics. The collisional transfer of rotational and vibrational energy from the perturber to the excited state dopant is also ruled out due to the appearance of subthreshold structure in CH_3I/Ar [3,18,20] and CH_3I/Xe [21].

In the remainder of Chapter 6, the focus switches to probing the behavior of subthreshold photocurrent for variable dopant number density ρ_D [17,19,20] and perturber number density ρ_P [14,17-20]. The analysis presented leads to the conclusion that two general mechanisms, namely electron attachment and associative ionization, are sufficient to model the density dependence of the subthreshold structure. However, the pathways involving these processes differ depending on the nature of the perturber [14,17–20]. For instance, if the perturber has a large electron attachment cross-section and a large ground-state polarizability, subthreshold photoionization can proceed through direct dopant/perturber interactions [14,17,19,20]. On the other hand, if the electron attachment cross-section and ground-state polarizability of the perturber are small, the pathway generating subthreshold structure involves only indirect dopant/perturber interactions [14,17-20].

By systematically varying both ρ_D and ρ_P, the effective rate constants for electron attachment, k_{ea}, and associative ionization, k_{ai}, are determined from the variation in the peak areas of the subthreshold structure as a function of ρ_D and ρ_P. The electron attachment rate constants k_{ea} are shown to depend linearly on the principal quantum number n of the dopant Rydberg state, whereas the associative ionization rate constants k_{ai} are shown to scale with the dopant Rydberg state polarizability, or as n^7. Finally, the variation in k_{ea} is discussed in terms of the electron affinity of the dopant (or perturber), and the variation in k_{ai} is discussed in terms of the ground-state polarizability of the perturber (or dopant).

Chapter 2. Rydberg States of Atoms and Molecules

A. Introduction

Since this research uses perturber effects on high-n dopant Rydberg states to probe various dopant/perturber interactions, a brief review of Rydberg states is provided below. This discussion also examines the special properties of Rydberg states that make these highly excited states ideal for probing the effects of external fields, and of perturber molecules on the electronic structure of the dopant. Finally, a survey of some of the various techniques used to generate and study Rydberg atoms and molecules is presented.

i. Rydberg States

A Rydberg state of an atom or molecule is a highly excited state in which the Rydberg electron (optical electron) is so distant from the cationic core that the core appears to this electron as a massive point charge. Rydberg states were first observed in 1885, during the study of the visible spectrum of the sun [23]. During this investigation [23], a series of intense lines at wavelengths

$$\frac{1}{\lambda} = \frac{4}{3645.6\,\text{Å}}\left(\frac{1}{4} - \frac{1}{n^2}\right),$$

where $n > 2$ is a positive integer, was observed. This series, also known as the Balmer series, was later recognized to arise from the electronic transitions from the $n = 2$ Rydberg state of atomic hydrogen to higher lying Rydberg levels. Further studies [1,2,23-25] showed that other atoms and molecules possess similar series, the excitation energies of which could be fitted to the more general equation

$$E_n = I - \frac{Ry}{(n - \delta_\ell)^2}, \qquad (2.1)$$

where I is the series limit (i.e., the ionization energy), Ry is the Rydberg constant (13.606 eV), n is the principal quantum number, and δ_ℓ is the quantum defect. (The quantum defect δ_ℓ embodies the influence of a nonhydrogenic core, and depends on the orbital angular momentum quantum number ℓ of the optical electron [26-28].)

The presence of a molecular core leads to several notable differences between Rydberg molecules and Rydberg atoms [1,4,29]. One of these differences is the amount of structure present in high-resolution optical spectra of Rydberg molecules. This structure is due to the many different rotational/vibrational levels of the molecular core, all of which can have converging Rydberg series [2-4,10]. (This increase in structure is discussed for the specific cases of HI, CH_3I and C_2H_5I in the next Section.)

One core ion effect is observed when the core ion is electronically excited with enough energy to cause the core to dissociate [29,30]. If the Rydberg electron happens to be far away from the core during the dissociation, this electron is not influenced by the dissociation process. As the fragments separate, one of the fragments remains in a high Rydberg state while the other fragment is neutral (cf. Fig. 2.1). A short list of molecules which undergo

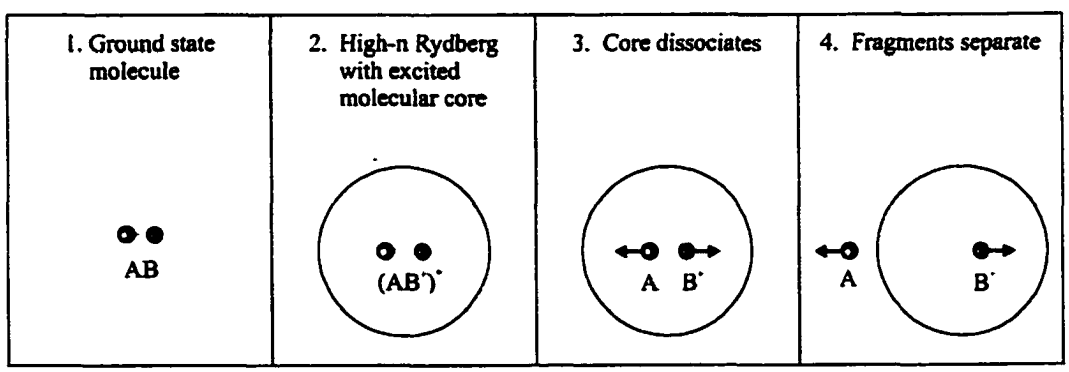

Fig. 2.1. The core ion model: schematic illustration of dissociation of a molecule AB to give a Rydberg atom fragment B and a neutral fragment A. (Adapted from [29].)

this type of dissociation process, which generally requires a two-electron excitation [29], is given in Ref. [29].

When the Rydberg electron passes close to the core while the core is either vibrationally or rotationally excited, the motion of the core ion can effect the behavior of this electron. In one instance, the Rydberg electron can collide superelastically with the core and thereby gain sufficient kinetic energy to ionize at the expense of the vibrational/rotational energy of the core. This type of ionization is known as vibrational or rotational autoionization [7,29-31] and is discussed in more detail in Chapter 3.C.ii. Predissociation may also occur as the Rydberg electron passes through the ionic core. In predissociation, however, the Rydberg state couples to the potential curve of a repulsive valence state which, in turn, causes the molecule to dissociate into non-Rydberg fragments [29,30,31].

Although the differences between Rydberg atoms and molecules are many, the similarities between the properties of these highly excited atoms and molecules at high-n are also extensive. These similarities arise from the small size of the ionic core with respect to the classical orbit of the Rydberg electron, as diagrammed in Fig. 2.2. Since the Rydberg electron is far from the core, the long-range potential energy between the ionic core and the Rydberg electron is

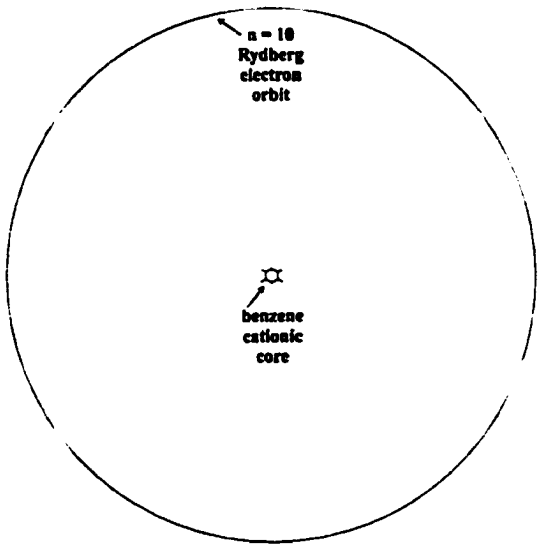

Fig. 2.2. Drawing of a n = 10 orbit of a Rydberg electron around a benzene core. The radius of the benzene molecule is 2.48Å, and the radius of the Rydberg orbital is 53 Å. (This drawing is to scale.)

Coulombic. The eigenenergies obtained from the solution to the Coulombic Schrödinger equation are $E_n = -1/n^2$ (in atomic units) and, therefore, it follows from the virial theorem that the radius of a Rydberg orbital is proportional to n^2.

The large orbital nature of the Rydberg electron (cf. Fig. 2.2) means that, for molecular Rydberg states, this electron is largely decoupled from the rotational or vibrational transitions of the core. This large orbit also makes a Rydberg state extremely sensitive to the presence of perturber molecules (cf. Chapter 3), and the low binding energy of these states increases the perturbational effectiveness of external fields. The presence of an electric field can cause Stark splitting [9,32,34-37] or field ionization [9,32,34,36,38]. Magnetic fields generally affect the Rydberg state in the form of diamagnetic energy shifts [9,32,34,36,39]. The magnetic analog to the Stark effect, namely the Zeeman effect, is not easily observable even in atoms. Therefore, probing the Zeeman effect generally takes the form of studying changes in the bandshapes of an absorption spectrum, as a function of the magnetic field strength, using magnetic circular dichroism for example [32,34,36,40,41].

In general, the n-scaling of many of the properties of Rydberg molecules can be developed from an analysis of the transition dipole matrix elements, which scale as n^2, and the eigenenergy separations, which scale as n^{-3} [9]. For example, from second-order perturbation theory, the polarizability α of a Rydberg state is approximated by [42]

$$\alpha = \sum_{\substack{m \\ n<m}} \frac{|\mu_{nm}|^2}{E_m - E_n},$$

where μ_{nm} are the electronic transition dipole matrix elements, and E_i ($i = m, n$) are the state energies. Since μ_{nm} is proportional to n^2, and $E_m - E_n$ is proportional to n^{-3}, the excited-state polarizability scales as n^7. Some of the other n-scaling laws are listed in Table 2.1.

Table 2.1. Properties of Rydberg atoms and molecules. (Adapted from [9].)

Property	n dependence
Binding energy	n^{-2}
Energy between adjacent n states	n^{-3}
Orbital radius	n^{2}
Geometric cross-section	n^{4}
Dipole moment $\langle nd\|er\|nf\rangle$	n^{2}
Polarizability	n^{7}
Radiative lifetime	n^{3}
Fine-structure interval	n^{-3}
Excitation cross-section	n^{-3}

ii. Generation of Rydberg Molecules

Rydberg atoms and molecules can be created using a variety of methods. However, these methods fall into three broad categories, namely charge exchange, electron impact or photo-excitation. Regardless of the excitation process, the cross-section for the production of Rydberg atoms or molecules always scales as n^{-3} [3,9]. Below, a description of these three general methods for generating Rydberg states is discussed along with the advantages and disadvantages of each technique.

Generating a Rydberg molecule via electron impact begins by crossing a molecular beam with a beam of electrons having a set kinetic energy. The impact of the high-energy electrons creates a few Rydberg molecules along with molecular ions. The molecular beam then passes through an ion extractor to remove the molecular ions, proceeds through analyzer plates set to a specific voltage (which can be varied), and finally enters the detector (which ionizes all remaining Rydberg states via a preset electric field and detects the ions). By assuming that ionization within the analyzer will occur at the classical electric field $F = 1/16\ n^{4}$ [9], the analyzer plates can be used to change the n distributions of Rydberg states reaching the detector [9,43,44,45]. The advantages of electron impact excitation are the relative

simplicity and generality of the method. However, this method is inefficient and non-selective, since all of the energetically possible states are produced.

In charge exchange, a molecular ion beam, usually generated by a plasma source, impinges on a solid (foil) or on a neutral gas and captures electrons into highly excited Rydberg orbitals. The Rydberg molecules are then separated from the ion beam using an ion deflector, and the molecular Rydberg states are studied farther downstream in the beam. The disadvantages of this type of production method are excitation inefficiency and non-selectivity. Therefore, as in the case of electron impact, a method for filtering the states of differing n values must be used for studying individual n-states [9,45,46].

Generation of a Rydberg state by optical excitation is highly selective, since excitation to a Rydberg level requires a specific energy. Therefore, one limiting factor for studying Rydberg states by optical means is the resolution of the light used for excitation, which is determined either by the resolution of the monochromator or of the laser. Some of the various ways to detect Rydberg atoms and molecules include fluorescence, transmission, field ionization, photoionization, and optogalvanic methods [3,8,9]. Below, two methods for studying Rydberg states via optical excitation are reviewed.

B. Photoabsorption

In photoabsorption spectroscopy, the intensity of monochromatic light passing through a sample is measured, as a function of wavelength (or energy), using a photosensitive detector like a photomultiplier or a photodiode. A decrease in this transmitted intensity, which appears as a dip in the baseline of incident intensity when intensity is plotted versus wavelength, indicates the occurrence of an electronic or molecular transition in the sample.

(A transmission spectrum, which is a plot of transmitted intensity versus wavelength (or energy), can be converted to an absorption spectrum via absorption = 1 - transmission.)

The width, intensity and position of a band (or peak) in an absorption spectrum depend on the nature of the transition and on the properties of the sample. For example, absorption bands in gas-phase samples are much sharper than the same bands in condensed-phase samples due to many factors, including the increase in collisional depopulation of the excited state in the condensed-phase sample. Electronic transitions in atoms are generally sharper than similar electronic transitions in molecules due, in part, to the effects of the molecular core. As mentioned above, the width of the absorption band also depends on the type of transition. High-*n* Rydberg transitions are usually sharper than low-*n* Rydberg and valence transitions because of core ion effects.

The energy position of an absorption band is indicative of the type of transition giving rise to that band. Molecular transitions like rotations and vibrations fall within the microwave and infrared energy regions, whereas electronic transitions occur in energy regions above and including the visible energy region. The type of electronic transition can also be inferred from the energy region where the transition occurs, with Rydberg transitions generally falling within the vacuum ultraviolet (VUV) region. The VUV absorption spectra of HI, CH_3I and C_2H_5I (measured in this work) are presented and discussed below in order to illustrate some of the various properties of Rydberg states that can be observed using absorption spectroscopy.

In Fig. 2.3, the assigned absorption spectra of HI, CH_3I and C_2H_5I are presented. (The details leading to these assignments can be found elsewhere (HI [47-49], CH_3I [49-54] and C_2H_5I [54-56]) and, therefore, are not repeated here.) The similarities among these spectra

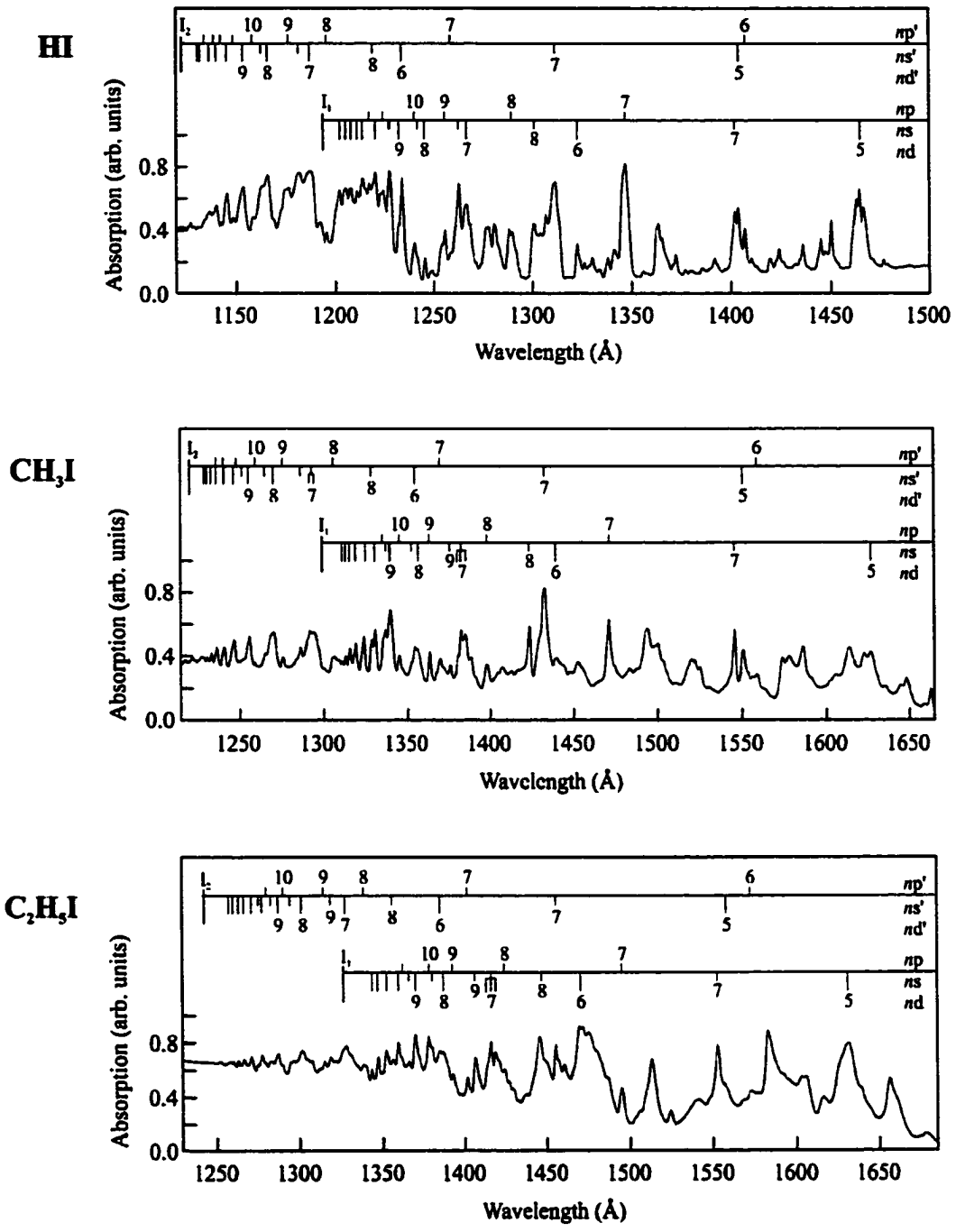

Fig. 2.3. Absorption spectra of HI (1.0 mbar), CH_3I (0.10 mbar) and C_2H_5I (0.50 mbar). The resolution for each spectrum is 0.9 Å. For HI, $I_1 \equiv I\ (^2\Pi_{3/2}) = 10.386$ eV [48] and $I_2 \equiv I\ (^2\Pi_{1/2}) = 11.050$ eV [48]. For CH_3I, $I_1 \equiv I(^2E_{3/2})$ and $I_2 \equiv I(^2E_{1/2})$. For C_2H_5I, $I_1 \equiv I\ (\tilde{X}_1\ ^2E_{1/2})$ and $I_2 \equiv I\ (\tilde{X}_2\ ^2E_{1/2})$. See Chapter 4 for the experimental details.

imply that the Rydberg electron is located in an electronically similar environment for each of these gases. Furthermore, the sharpness of the absorption bands indicates that each of these molecules contains a quasi-atomic Rydberg chromophore. Together, these two observations suggest that the hole left by the Rydberg electron after excitation is localized on the iodine atom in these molecules.

The absorption spectra of these molecules should become more complicated progressively from HI to CH_3I to C_2H_5I, due to the decrease in molecular symmetry (from $C_{\infty v}$ to C_{3v} to C_s, respectively), and to the increase in vibrational (and rotational) degrees of freedom. While this fact holds for the change from CH_3I to C_2H_5I, the absorption spectrum of HI (cf. Fig. 2.3a) appears to be more complicated than that for CH_3I (cf. Fig 2.3b). This increased complexity arises from the occurrence of rotational structure in HI which can be resolved [47,48] because of the large rotational constant exhibited by this molecule. Furthermore, HI possesses a broad photodissociation band underlying all spectral features between 1125 and 1240 Å.

In Chapter 5, the perturber-induced energy shifts of high-*n*d and -*n*d′ Rydberg states of CH_3I and C_2H_5I will be used to determine the electron scattering length of the perturber. However, the use of photoabsorption spectroscopy to monitor perturber effects on dopant Rydberg states has a serious drawback: Namely, in order to observe the absorption spectrum of the dopant molecule, the perturber cannot absorb in the same energy region. This seriously limits the number of dopant/perturber systems which can be studied. A solution to this problem presents itself in the form of photoionization spectroscopy, since perturber effects on dopant Rydberg states can also be monitored using the autoionization structure of the dopant molecule.

C. Photoionization

A simple form of photoionization spectroscopy results from the measurement of the current produced from a sample by the absorption of monochromatic light, as a function of energy (or wavelength), using an applied voltage across a pair of parallel-plate electrodes as a detector. Direct photoionization occurs when the energy of the incident light is greater than the first ionization threshold of the molecule, causing an excitation of an electron into the ionization continuum (cf. Fig. 2.4a). However, if the atom or molecule possesses more than one electron and, therefore, more than one ionization threshold, other processes such as autoionization and "shake-off" [57] can occur.

In autoionization, a Rydberg state lying above an ionization threshold is populated by optical excitation, and this state subsequently ionizes (cf. Fig. 2.4b). The intensity of the autoionization structure depends on many factors [9,30]. For example, if autoionization from a given excited state is slower than other decay processes, such as fluorescence or predissociation, then the intensity of the autoionization structure will be small. While autoionization, fluorescence and predissociation are (to a first approximation) independent and competitive, strong interactions among these separate processes can lead to interference effects [9,30] and to changes in the overall intensity of the autoionization features.

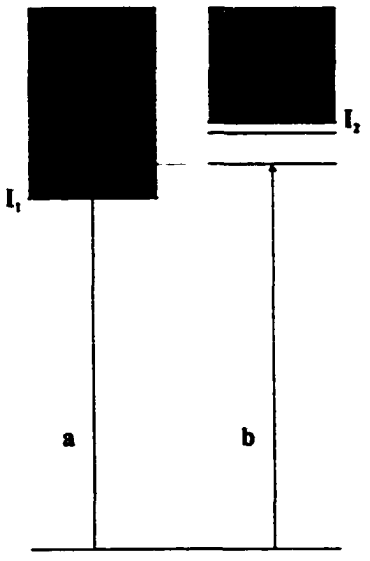

Fig. 2.4. A general schematic of (a) direct photoionization and (b) autoionization.

In the presence of a strongly absorbing perturber, photoionization spectroscopy will still give rise to a

signal even in the case of near total optical absorption by the perturber. Therefore, photoionization spectroscopy allows one to study perturber effects on Rydberg energy positions in a broader range of dopant/perturber systems than does photoabsorption spectroscopy. Furthermore, photoionization spectroscopy can also be used to probe dopant/perturber interactions that lead to the observation of photocurrent below the first ionization threshold of the dopant (i.e., subthreshold photoionization).

Chapter 3. Perturber Effects on Rydberg States

The large orbital nature of high-n Rydberg states makes these states highly sensitive to perturber molecules. One reason for this sensitivity is the large number of perturber atoms or molecules which can occupy the space between the ion core and the Rydberg electron. For example, assuming that the perturber Ar is a perfect gas, the number of Ar atoms between the $n = 15$ Rydberg electron and the ion core of a dopant is 10^2. If the Rydberg electron is in the $n = 30$ orbital, this number increases to 10^4. The large number of perturbers between the ion core and the Rydberg electron indicates that high-n Rydberg states will broaden and shift differently than do valence or low-n Rydberg states due to Rydberg electron collisions with the perturber, and to the polarization of the perturbers by the ion core.

Similarly, the binding energy for the $n = 15$ orbital is approximately 0.06 eV. Thus, a high-n Rydberg electron can be easily removed from an atom (or molecule) by direct electron attachment to a perturber molecule (assuming that the perturber molecule has a high electron attachment cross-section), or by other dopant/perturber interactions such as associative ionization.

In this Chapter, the energy shift and spectral broadening of high-n Rydberg states are discussed in terms of two independent interactions, namely the interaction of the Rydberg electron with the perturbers and the interaction of the positive ion core with the perturbers. Using these interactions, the energy shift of high-n Rydberg states is modeled in Section A, while the broadening of spectral lines is discussed in Section B. Some of the various mechanisms leading to subthreshold photoionization are then presented in Section C.

A. Perturber-induced Energy Shifts

i. The Fermi Model

In the 1930s, Amaldi and Segrè [58] observed a shift of the high-*n* Rydberg states of alkali metals in the presence of a rare gas. These energy shifts were later explained by Fermi [11] within a simple model which assumed that, due to the large size of the Rydberg state, the perturbers interacted separately with the Rydberg electron and with the ionic core. (This approximation is not valid for low-*n* Rydberg states.)

As a result of this assumption, the shift of the high-*n* Rydberg states arises from two independent phenomena, namely the scattering of the Rydberg electron off of the perturber, and the polarization of the perturbers due to the ionic core. In other words [11],

$$\Delta = \Delta_{sc} + \Delta_{pol} , \tag{3.1}$$

where Δ is the total energy shift, Δ_{sc} is the "scattering" shift and Δ_{pol} is the "polarization" shift.

Since the Rydberg electron can be regarded as quasi-free, the analysis of Δ_{sc} is an electron scattering problem. Thus, a Rydberg electron with a given kinetic energy is scattered by the potential of the perturber, which is negligible for distances $r > r_0$ (where r_0 is a minimum scattering radius of the perturber). In order to obtain a formula for Δ_{sc}, the long-range Schrödinger equation for the Rydberg electron must be solved. By decomposing the radial wave function R(r) of the electron into partial waves $R_l(r)$ corresponding to different angular momenta, and by assuming that the scattering of the electron is s-wave (i.e., low-energy scattering), the Schrödinger equation for the Rydberg electron can be solved to give a scattering shift of [11]

$$\Delta_{sc} = - \left(\frac{2 \pi \hbar^2}{m_e} \right) A \rho_P , \tag{3.2}$$

where m_e is the electron mass, A is the zero-kinetic-energy electron scattering length of the perturber, $\hbar$ is the reduced Plank constant, and ρ_P is the number density of the perturber. The electron scattering cross-section is then $\sigma = 4\pi A^2$ [11], if the kinetic energy of the electron is close to zero. From Eq. (3.2), one can see that the energy shift due to the scattering of the Rydberg electron from the perturber can be either to the blue or to the red depending on the sign of A.

In order to deal with the polarization shift Δ_{pol}, Fermi [11] reasoned that the positive core of the Rydberg molecule polarizes the perturber atoms (or molecules), thus yielding an energy shift of

$$\Delta_p = -\frac{1}{2}\alpha e^2 \sum_N R_N^{-4} ,$$

where α is the ground-state electronic polarizability of the perturber and R_N is the distance between the core and the Nth perturber. If the Rydberg state has a large radius, implying that $N >> 1$, the sum can be replaced with an integral to give [11]

$$\Delta_p = -\frac{1}{2}\alpha e^2 4\pi \rho_P \int_{R_0}^{\infty} R^{-4} R^2 \, dR , \tag{3.3}$$

where the upper integration limit is justified by the large extent of the orbital, and the lower integration limit indicates the minimum distance between the core and the perturber. For R_0, Fermi chose the Wigner-Seitz radius of $R_0 = (3/4\ \pi\ \rho_P)^{1/3}$ since, at a given density ρ_P, no perturber atoms can lie at a distance less than R_0 from the core. Substituting the Wigner-Seitz radius into the previous equation and integrating gives a polarization shift of [11]

$$\Delta_{pol} \approx -10\ \alpha e^2 \rho_P^{4/3} . \tag{3.4}$$

Therefore, the total perturber-induced energy shift becomes

$$\Delta = -\left(\frac{2\pi\hbar^2}{m_e}\right) A\,\rho_P - 10\,\alpha\,e^2\,\rho_P^{4/3} \qquad (3.5)$$

within Fermi's original model.

Although the Fermi model accurately predicts the fact that the total energy shift does not depend on n, this model does not accurately describe the ρ_P dependence of the total energy shift, which experimentally scales linearly with ρ_P [59-62] (cf. Fig. 3.1). This, in turn, caused serious doubt about the Fermi model, and led to a direct treatment of the total energy shift from impact theory by Alekseev and Sobel'man [5,67].

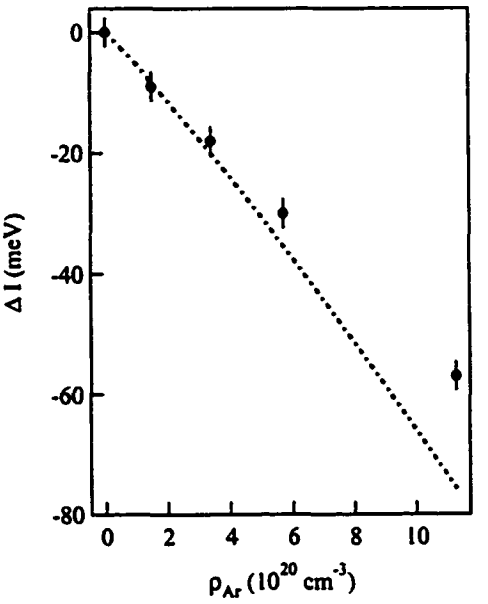

Fig. 3.1. Shift in the first vertical ionization energy ΔI of CH_3I in varying Ar number densities ρ_{Ar}. ●, data from [63]; -·--·, total perturber-induced energy shift from the Fermi model (i.e., Eq. (3.5)) with A = -0.896 Å [64] and $\alpha = 1.64 \times 10^{-24}$ cm^{-3} [65,66].

ii. Impact Approximation

Alekseev and Sobel'man [5,67] studied perturber pressure effects on dopant Rydberg states in terms of the impact approximation, which assumes that the time between collisions is long in comparison to the collision time (thus implying low perturber number densities). These authors [5,67] maintained Fermi's assumption concerning the independence of Δ_{sc} and Δ_{pol}. However, by approaching the solution of the Schrödinger equation for the Rydberg electron through the impact approximation, a generalized expression for the scattering shift Δ_{sc} could be determined [5,67]. This expression, namely

$$\Delta_{sc} = -\left(\frac{2\pi\hbar^2}{m_e}\right)\rho_P \int \left[\frac{\pi}{k}\sum_{\ell}(2\ell + 1)\sin 2\delta_\ell\right] W(k)\,dk\ ,$$

reduces to Eq. (3.2) when the scattering is s-wave (which holds for high-n Rydberg states). In the above equation, $\hbar k$ is the momentum of the scattered electron, δ_ℓ is the ℓ-wave phase shift of the scattered electron, and $W(k)$ is a (momentum-dependent) excited-state distribution function.

Alekseev and Sobel'man [5,67] also assumed the same form for the polarization potential as did Fermi [11], namely

$$V(R) = -\frac{\alpha e^2}{2R^4}\ . \tag{3.6}$$

However, in this approach, the Rydberg atom is regarded as a classical oscillator having an emitting frequency which is perturbed by collision with a perturber. The distance between the cationic core and the perturber at time t is [5,67]

$$R = \sqrt{b^2 + v(t - t_0)^2}\ , \tag{3.7}$$

where b is the impact parameter at the time of nearest approach t_0, and v is the velocity of the perturber. Thus, the frequency shift $\chi(R)$ produced by a large number of perturbers having different impact parameters can be derived by substituting Eq. (3.7) into Eq. (3.6) and summing over all of the perturbers. The total frequency shift, therefore, is [5,67]

$$\chi(R) = -\sum_{i}\frac{\alpha e^2}{2\hbar}\left[b_i^2 + v(t - t_{0i})^2\right]^{-2}\ .$$

During the perturbation caused by the collision, the phase of the oscillation is modified. This phase shift $\eta(b,v)$, which is determined by the passage of a perturber at a distance b, can be written as [5,67]

$$\eta(b,v) = -\left(\frac{\alpha e^2}{2\hbar}\right) \int_{-\infty}^{\infty} (b^2 + v^2 t^2)^{-2}\, dt$$
$$= -\left(\frac{\alpha e^2}{2\hbar}\right) \frac{\pi}{2} \frac{1}{v b^3} . \qquad (3.8)$$

Weisskopf [68,69] assumed that a collision occurred when the phase shifts $\eta(b) \geq \eta_0 = 1$. If one substitutes this value of η_0 in Eq. (3.8), one obtains the maximum radius b for which collisions are still effective. This radius, namely [5,67-69]

$$b_w = \left(\frac{\pi \alpha e^2}{4\hbar v}\right)^{1/3} , \qquad (3.9)$$

is known as the Weisskopf radius. The polarization shift Δ_{pol} is then determined from the phase shift by [5,67]

$$\Delta_{pol} = 2\pi v \rho_p \int_0^{\infty} \sin\eta(b)\, b\, db ,$$

which leads to the final expression for Δ_{pol} [5,67]

$$\Delta_{pol} = -9.87 \left(\frac{\alpha e^2}{2}\right)^{2/3} (\hbar v)^{1/3} \rho_p . \qquad (3.10)$$

Therefore, the total perturber-induced energy shift under the impact approximation is

$$\Delta = -\left(\frac{2\pi\hbar^2}{m_e}\right) A \rho_p - 9.87 \left(\frac{\alpha e^2}{2}\right)^{2/3} (\hbar v)^{1/3} \rho_p . \qquad (3.11)$$

Eq. (3.11) accurately predicts both the n independence and the linear perturber number density dependence of the perturber-induced energy shifts of CH_3I in the rare gases (cf. Fig. 3.2 and [63]).

Later studies [11,70] showed that choosing the Weisskopf radius (i.e., Eq. (3.9)) as the lower integration limit for the polarization equation of the Fermi model (i.e., Eq. (3.3)) yields a polarization shift of

$$\Delta_{pol} \approx -10.78\left(\frac{\alpha e^2}{2}\right)^{2/3}(\hbar v)^{1/3}\rho_p, \quad (3.12)$$

which is almost identical to Eq. (3.10). Thus, the key to accurately modeling perturber-induced energy shifts lies with the choice of the cut-off radius for the interaction between the ionic core and the perturber molecule.

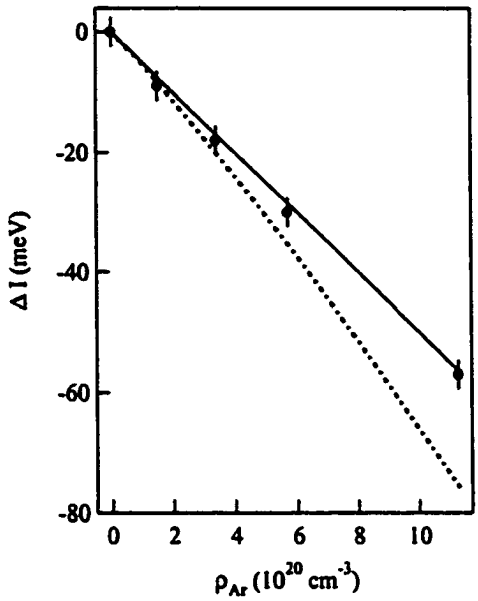

Fig. 3.2. Shift in the first vertical ionization energy ΔI of CH_3I in varying Ar number densities ρ_{Ar}. ●, data from [63]; -·-·-, total perturber-induced energy shift from the Fermi model (i.e., Eq. (3.5)), ——, shift from the Alekseev and Sobel'man model (i.e., Eq. (3.11)) with A = -0.896 Å [64], v = 4.0 x 10^4 cm/s and α = 1.64 x 10^{-24} cm^{-3} [65,66]. (Adapted from [63].)

The near equality of Eq. (3.10) and Eq. (3.12) also explains the reason why Eq. (3.11) continues to hold once the impact approximation fails [70]. The Alekseev and Sobel'man model was shown to be capable of accurately predicting the energy shifts of high-n Rydberg states caused by a perturber number density of up to 2 x 10^{21} cm^{-3} [63]. Once Eq. (3.11) was shown to be valid for high density measurements, this equation was used to evaluate the zero-kinetic-energy electron scattering lengths of a wide variety of atomic and molecular perturbers [21,70-75]. A summary of the scattering lengths and cross-sections determined from the perturber-induced energy shifts of high-n Rydberg states is given in Table 3.1. In Chapter 5, Eq. (3.1) is used, with the scattering shift defined by Eq. (3.2) and the polarization shift defined by Eq. (3.12), to

Table 3.1. Total shift rates Δ/ρ_P, zero-kinetic-energy electron scattering lengths and zero-kinetic-energy electron cross sections determined from Eq. (3.11).

Perturber	Δ/ρ_P (10^{-23} eV cm^3)	A (nm)	σ (10^{-14} cm^2)	Ref.
Ar	-4.75	-0.082	0.084	[71]
CH_4	-7.86	-0.138	0.238	[72]
C_2H_6	-10.1	-0.176	0.389	[72]
C_3H_8	-12.9	-0.228	0.653	[72]
CO_2	-11.8	-0.224	0.631	[73]
H_2	1.62	0.049	0.030	[74]
He	2.44	0.057	0.041	[70]
Kr	-8.60	-0.160	0.322	[70]
N_2	0.00	0.019	0.0045	[75]
Ne	0.09	0.0090	0.0010	[70]
Xe	-16.8	-0.324	1.32	[21]

reevaluate the zero-kinetic-energy electron scattering length of Ar [14], and to evaluate the zero-kinetic-energy electron scattering lengths of CF_4 [15], c-C_4F_8 [15] and SF_6 [14,16,17].

iii. Polarization Distribution Model

Recently, Al-Omari, Reininger and Huber [13] have reexamined the theory behind perturber-induced energy shifts, using a polarization energy distribution. This approach begins by writing the polarization energy distribution in the static limit as [13,38]

$$P(W) = \frac{1}{Z} \int e^{-\beta U(r_1, \ldots, r_2)} \, \delta(W - w(r_1, \ldots, r_2)) \, dr_1 \cdots dr_2 \, ,$$

where Z denotes the partition function, $\beta = 1/k_B T$, k_B is the Boltzmann constant, $U(r_1, \ldots, r_N)$ is the multidimensional potential representing the ground-state interactions among the molecules, and $w(r_1, \ldots, r_N)$ is the ion-medium polarization energy. Under the steepest descent approximation (infinite temperature limit), the location of the maximum of $P(W)$, W_M, was shown to be [13]

$$W_M = -\left(\frac{(3 J_k / k)^{k/(k-3)} \, (2k - 6)}{2k - 3} \right)^{(k-3)/3} \, ,$$

where J_k is a function of ρ_P and k is a positive integer. This expression simplifies to [13]

$$W_M = -\frac{18.9}{2}\,\alpha\, e^2 \rho_P^{4/3}$$

which, similar to the original Fermi model, predicts a $\rho_P^{4/3}$ dependence of the polarization shift. Al-Omari, et al. [13] found that the above expression compared favorably to finite-temperature Monte-Carlo calculations for NO in Ar [13,76], and they concluded that their results should remain quantitatively valid for $\rho_P \leq 1.6 \times 10^{22}$ cm^{-3}.

If one assumes that the maximum in $P(W)$ gives the polarization shift, Eq. (3.1) becomes

$$\Delta = -\left(\frac{2\pi\hbar^2}{m_e}\right) A\,\rho_P - 9.45\,\alpha\, e^2 \rho_P^{4/3}\,. \qquad (3.13)$$

This derivation has called into question Eq. (3.11) and, therefore, the scattering lengths determined using the impact approximation for the polarization shift. In order to assess the continued applicability of Eq. (3.11), Eq. (3.13) was used to determine the zero-kinetic-energy electron scattering length of Ar [16]. In Fig. 3.3, the shift in the first vertical ionization energy ΔI of CH_3I, obtained from [63], is plotted versus the Ar number density ρ_{Ar}, along with the results of least-square fits to Eq. (3.13) and Eq. (3.11). The nonlinear least-square fit to

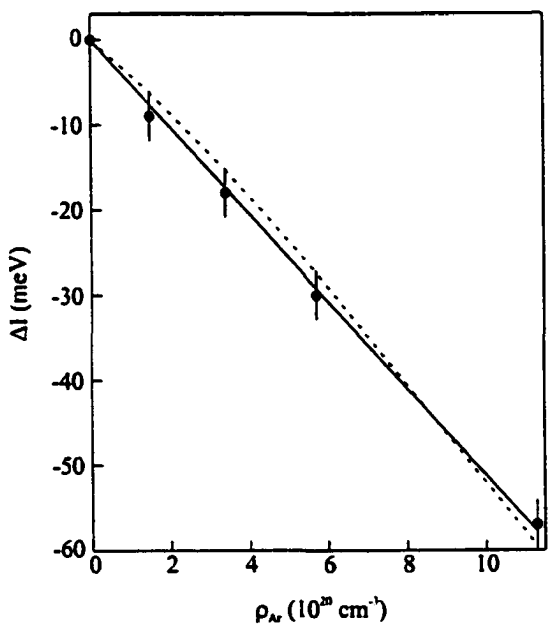

Fig. 3.3. Shift in the first vertical ionization energy of CH_3I in varying Ar number densities ρ_{Ar}. ●, data from [63]; – – –, nonlinear least-squares fit to Eq. (3.13); ——, linear least-squares fit to Eq. (3.11). See text for discussion. (Adapted from [16].)

Eq. (3.13) yields an electron scattering length of A = - 0.061 nm [16], while the linear least-square fit to Eq. (3.11) yields a scattering length of A = - 0.091 nm [16]. While both fits are within the error bars of Fig. 3.3, the scattering lengths differ by more than 30%. Moreover, the scattering length obtained from Eq. (3.11) compares favorably to the value A = -0.089 nm determined by the electron swarm method [64].

Therefore, from Fig. 3.3, one can conclude that Eq. (3.11) provides a better description of the energy shift in the low-density region than does Eq. (3.13). Thus, the use of Eq. (3.11) later in this work to determine the electron scattering lengths of CF_4, c-C_4F_8 and SF_6 is justified. (One possible problem with Eq. (3.13) is that Δ_{pol} was identified with the polarization energy that maximizes $P(W)$, rather than with that which would result from first convoluting $P(W)$ with the pure dopant spectrum, as discussed in [77] for the case of field ionization of CH_3I in Ar.)

B. Spectral Broadening

Rydberg states, in contrast to valence states, show a characteristic asymmetric broadening as a function of perturber number density (cf. Fig. 3.4). This asymmetric broadening was explained in the statistical theory of pressure broadening developed by Margenau [78] and by Jablonski [79], and subsequently reviewed by various authors [5,80-84].

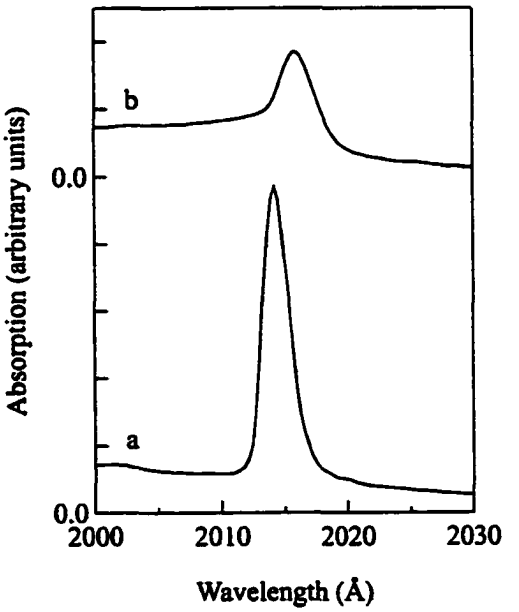

Fig. 3.4. The 6s Rydberg state of (a) 0.100 mbar CH_3I and (b) 0.100 mbar CH_3I perturbed by 0.98 x 10^{21} cm^{-3} CF_4. These spectra were measured in this work.

In a qualitative explanation of this statistical theory, spectral broadening is assumed to arise from a two-body process characterized by a shift in the dopant-perturber potential energy curves for each of the electronic states of the dopant [5,78-84]. When a Rydberg state is populated, the repulsive exchange forces between the dopant and the perturber become important at a much larger distance than in the ground-state potential [5,78-84] of the dopant/perturber pair. If the probability of a vertical transition from all points of the ground-state potential curve is equal, then the details of the perturbed band shape will depend on the relative convexities of the two potential curves, and on the statistical distribution of the dopant-perturber pairs along the internuclear coordinate [5,78-84]. This generally leads to the development of a wing on the blue side of the unperturbed line. As the pressure increases, the pair distribution function grows in the region of smaller dopant-perturber distances, thus causing a broadening in the blue wing [5,78-84]. Therefore, the broadening effect is very sensitive to the interaction potentials of the ground state and of the excited state of the dopant/perturber pair [5,78-84].

C. Subthreshold Photoionization Mechanisms

In the previous two sections, the shift and broadening of dopant Rydberg states due to the presence of a perturber were introduced and discussed. However, dopant/perturber interactions can also lead to the appearance of photoionization structure at energies less than the first ionization threshold of the dopant molecule [6,7,14,17-21,48,73,75,85-115]. Since this work focuses on dopant/perturber interactions in a static gas-phase system, this Section discusses mechanisms which can lead to subthreshold structure.

i. Collisional Ionization

Collisional ionization arises from the transfer of translational, rotational or vibrational energy from the perturber to the excited state dopant. Assuming that the collision is elastic, the translational exchange of energy ΔE is given by [9]

$$\Delta E = 4 k_B T v / V \tag{3.14}$$

where T is the temperature, v is the velocity of the Rydberg electron and V is the velocity of the perturber. Since the velocity of the high-n Rydberg electron scales as $1/n$, the translational exchange of energy between dopant and perturber will generally be less than $k_B T/100$, or less than 0.2 meV at room temperature [9].

If the perturber is a molecule, vibrational and rotational energy can be exchanged between the perturber and the dopant. The total amount of energy that can be transferred from the perturber to the Rydberg molecule due to the rotation and vibration of the perturber depends upon the population of the rotational and vibrational levels of the perturber at a given temperature.

In general, all of these interactions are closely spaced and therefore only appear as part of the unresolved exponential background of the ionization threshold [9,85,87].

ii. Rotational and Hot-band Autoionization

Unlike collisional ionization, rotational and hot-band (or vibrational) autoionization do not involve dopant/perturber interactions. Instead, these subthreshold mechanisms involve the interactions of the Rydberg electron with the molecular core and arise when the electron passes through the rotationally or vibrationally excited core and collides superelastically with the core, thereby gaining enough kinetic energy to ionize [29]. Since this effect is due to

vibrations and rotations in the molecular core, the photoionization structure will be temperature dependent.

While studying subthreshold photoionization in CH_3I, Ivanov and Vilesov [87,88] proposed the mechanism of hot-band autoionization as a possible explanation for subthreshold photoionization at low CH_3I number densities. This process was later verified by Meyer, Asaf and Reininger [85]. These authors [85] observed a weak subthreshold photoionization structure (cf. Fig. 3.5) with peak intensities that show a Boltzman-like temperature distribution (cf. Fig. 3.6). CH_3I has C_{3v} symmetry with three totally symmetric vibrations (ν_1, ν_2, ν_3) and three degenerate vibrations (ν_4,ν_5,ν_6) [1]. Using the ground-state

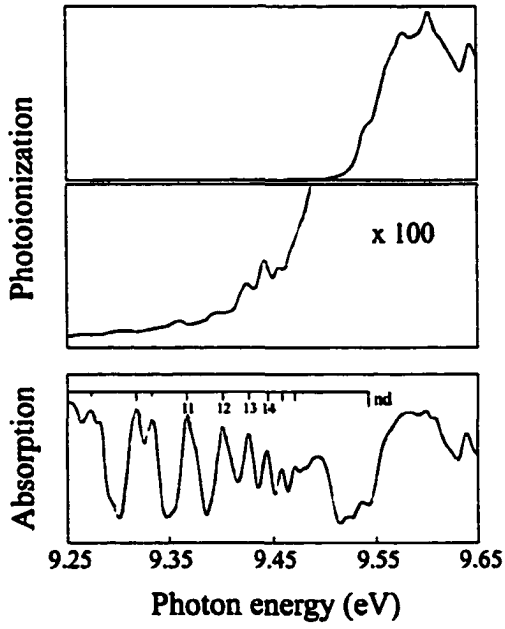

Fig. 3.5. Absorption (bottom) and photoionization (middle and top) spectra of 0.015 mbar CH_3I at 300 K. The middle spectrum shows the prethreshold range amplified by a factor of 100. The resolution is 7 meV. (Adapted from [85].)

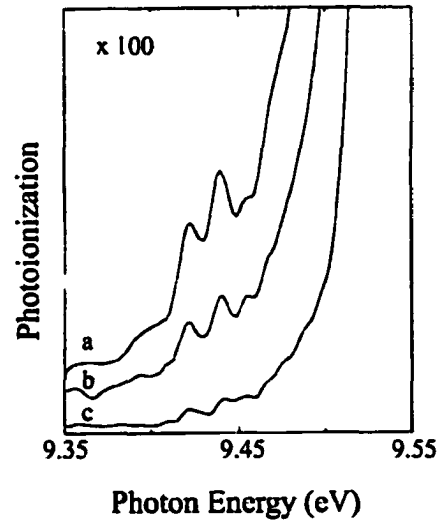

Fig. 3.6. Photoionization spectra of 0.025 mbar CH_3I at (a) 371 K, (b) 296 K and (c) 212 K. The spectra, normalized at 9.597 eV, are shown with a one-hundred magnification and staggered vertically. (Adapted from [85].)

energies of the symmetric vibrations [1] (ν_1 = 366 meV, ν_2 = 155 meV, ν_3 = 66 meV), Meyer and co-workers [85] showed that the first subthreshold peak observed in low-pressure photoionization of CH_3I (cf. Fig. 3.6) corresponds to the excitation of an electron from the ground-state $^1A_1$ (0,1,1) vibrational level into Rydberg states beginning at the 11d (0,1,1) state. The subsequent peaks have contributions from the hot-band autoionization of the *n*d(0,1,1) and (*n*+1)d(0,1,0) Rydberg states originating in the $^1A_1$ (0,1,1) and $^1A_1$ (0,1,0) levels, respectively. The first hot-band autoionizing Rydberg state, arising from the ground-state $^1A_1$ (1,0,0) vibrational level, could not be resolved due to the strongly increasing background [85] in the 9.472 eV region (cf. Fig. 3.6 and [85]). Similar types of effects have been seen in many diatomic and small polyatomic molecules, such as H_2 [89], PF_3 [90], K_2 [91], NH_3 [92], N_2 [93], NO_2 [94] and HBr [95]. HBr [95], N_2 [93] and H_2 [89] also show strong rotational autoionization structure. A good quantum mechanical model of these effects can be found in [86]. Hot-band and rotational autoionization have also been proposed as the mechanisms leading to subthreshold photoionization in HI [48].

Later in this work, the subthreshold photoionization of CH_3I described above is shown to be supplanted by a stronger subthreshold photocurrent (cf. Chapter 6 and [17-20]) as the number density of CH_3I is increased. This new subthreshold structure is not temperature dependent (cf. Chapter 6.C and [17-19]), but is dependent on the CH_3I number density. These measurements also accord with the behavior of the subthreshold photoionization structure observed in CH_3I by Ivanov and Vilesov [87,88].

iii. Electron Attachment

Electron attachment results when a dopant, excited to a high-*n* Rydberg state, collides with a perturber which has a large electron attachment cross-section. During this collision,

an electron is transferred from the dopant to the perturber, thus generating a perturber anion, which can then be detected. This electron attachment can take the form of simple attachment, dissociative attachment, or attachment followed by autodetachment.

Simple electron attachment, or [96]

$$D^* + P \rightarrow D^+ + P^- , \tag{3.15}$$

occurs when the Rydberg electron from the excited dopant D^* attaches directly to the perturber P (such as SF_6 [97-101]). Dissociative attachment, namely [96]

$$D^* + P \rightarrow D^+ + R_1 + R_2^- , \tag{3.16}$$

arises when the attaching electron causes the perturber (such as CCl_4 [97,102]) to dissociate into two or more separate atoms or molecules. Attachment followed by autodetachment occurs when the perturber anion is relatively unstable (such as C_6F_6 [102,103]) and proceeds through the reaction sequence [96]

$$D^* + P \rightarrow D^+ + P^- \rightarrow D^+ + P + e^- . \tag{3.17}$$

The type of electron attachment which a perturber molecule can undergo is usually monitored by observing the anions formed during the electron attachment process [96].

The electron attachment cross-section σ_{ea} is inversely proportional to the root mean square electron velocity [9], which for a Rydberg electron scales as $1/n$. Therefore, $\sigma_{ea} \propto n$ (cf. Fig. 3.7). Since the electron attachment rate constant k_{ea} is directly proportional to σ_{ea}, k_{ea} should also scale as n. Thus, as will be shown in Chapter 6, the n scaling of the rate constant can be used to investigate the process of electron attachment in dopant/perturber systems, where subthreshold photoionization can occur through more than one type of mechanism.

iv. Associative Ionization

Associative ionization, or [9]

$$D^* + P \rightarrow DP^+ + e^- , \qquad (3.18)$$

occurs when the collision between the excited state dopant D^* and the perturber P results in a dopant/perturber heteromolecular dimer cation and a free electron. Recently, Rosa and Szamrej [104] showed that the presence of a perturber could also act to stabilize the formation of dopant/dopant homomolecular dimers, which can then lead to the formation of a homomolecular dimer cation and a free electron:

$$D^* + D + P \rightarrow D_2^+ + P + e^- . \qquad (3.19)$$

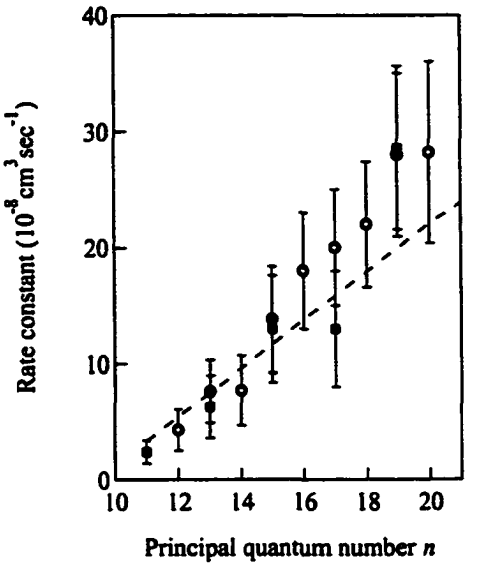

Fig. 3.7. The n dependence of the rate constant for electron attachment to SF_6 from collisions with K nd Rydberg states. O from [100], □ from [98]. – – –, rate constants calculated with postattachment electrostatic interactions (from [100]). (Adapted from [9].)

Associative ionization was originally discovered by Hornbeck and Molnar [105] while studying Rydberg states in the rare gases. These authors observed that ionization occurred at an energy onset lower than the first ionization threshold in the rare gases. By measuring the ionic products being produced from the impact of high-energy electrons with an atomic beam, these authors [105] concluded that the lower onset energy was due to rare gas dimer formation. Later studies by P. M. Dehmer and co-workers [106-113] showed several trends in the formation and ionization of rare gas dimers. One of these trends is a larger dissociation energy for homomolecular dimers in comparison to heteromolecular dimers [113], implying an increase in stability for homomolecular dimers. These authors [113] also showed that the dissociation energy

increases as the polarization of the perturber in the dopant/perturber pair increases. This fact was explained by assuming that a substantial part of the binding is due to the ion-induced dipole interaction, which is given by - $\alpha\ e^2$ / 2 R^4 [113], where α is the ground-state polarizability of the perturber, and R is the distance between the dopant core and the perturber. Thus, the rate constant for associative ionization k_{ai} should scale linearly with the ground state polarizability of the neutral partner in the dimer pair. Furthermore, dimerization is indicative of molecular interactions which, in turn, should depend upon the excited state polarizability of the Rydberg molecule [42]. This polarizability scales as n^7 (cf. Table 2.1) and, therefore, the rate constants for associative ionization, k_{ai}, should depend linearly on n^7.

During later photoionization studies of methyl halides, Ivanov and Vilesov [87,88] observed subthreshold photoionization in CH_3I corresponding to high-*n*d Rydberg states which could not be explained by hot-band autoionization (cf. Section C.ii) or photochemical rearrangement (cf. Section C.v). Due to the observed quadratic dependence of this structure on CH_3I number density, these authors [87,88] attributed the appearance of this structure to either electron attachment or associative ionization. However, since these measurements were made in a static gas-phase system, the exact mechanisms leading to the subthreshold photocurrent structure could not be determined. In further probes of subthreshold photoionization in CH_3I, A. M. Köhler [6] showed that, at high number densities of Ar (> 4.8 x 10^{19} cm^{-3}), the subthreshold photoionization decreased with increasing perturber number density. This observation was used to substantiate the existence of the associative ionization mechanism in CH_3I [6], since increasing the pressure of the perturber (at very high number densities) decreases the probability of collisions between the excited dopant and the

ground state dopant which, in turn, leads to a decrease in the intensity of the subthreshold photocurrent.

v. Other Mechanisms

Although the mechanisms discussed in Sections C.i - C.iv are the common ones used to explain subthreshold photoionization, several other mechanisms can also occur in static systems.

One of these mechanisms, namely Penning ionization, occurs when two electronically excited atoms or molecules collide with enough energy to create a neutral atom (or molecule) and a cation [9]:

$$D^* + D^{*\prime} \rightarrow D + D^+ + e^- . \qquad (3.20)$$

Photochemical rearrangement, on the other hand, depends on the stability of the molecule after electronic excitation. If the molecule is promoted into an unstable excited state, this molecule can dissociate into various products. For example, CH_3Cl is known to photodissociate into CH_3^+ and Cl^-, and thereby produce subthreshold photoionization 14 meV below the first ionization threshold of CH_3Cl. The intensity of this subthreshold photoionization structure is linearly dependent upon the CH_3Cl number density [88]. A similar process has also been observed in CH_3Br [88].

Two other types of collisional processes which can lead to subthreshold photocurrent are n-changing and ℓ-changing collisions [9,114-115]. Both of these processes involve the interaction of a very high-n Rydberg state ($n > 25$) with a perturber molecule and, therefore, are generally associated with the study of Rydberg atoms.

Chapter 4. Experiment

The requirements for the measurements presented in this work are (1) monochromatic light in the energy range of 6 – 11 eV with a resolution of < 15 meV, (2) a sample cell capable of withstanding high pressures, (3) the ability to control the temperature of the sample to within ± 1 K, (4) a method for accurately and reproducibly preparing samples, and (5) the ability to acquire, store and analyze data. In the following, each of the points mentioned above is discussed in more detail. This Chapter also includes information about the dopants and perturbers used in these experiments.

A. Experimental Apparatus

i. Monochromator and Endstation

The monochromator used for this work was the Aluminum Seya-Namioka monochromator [116] (cf. Fig. 4.1) located on bending magnet 8 of Aladdin, the electron storage ring at the University of Wisconsin Synchrotron Radiation Center in Stoughton, WI.

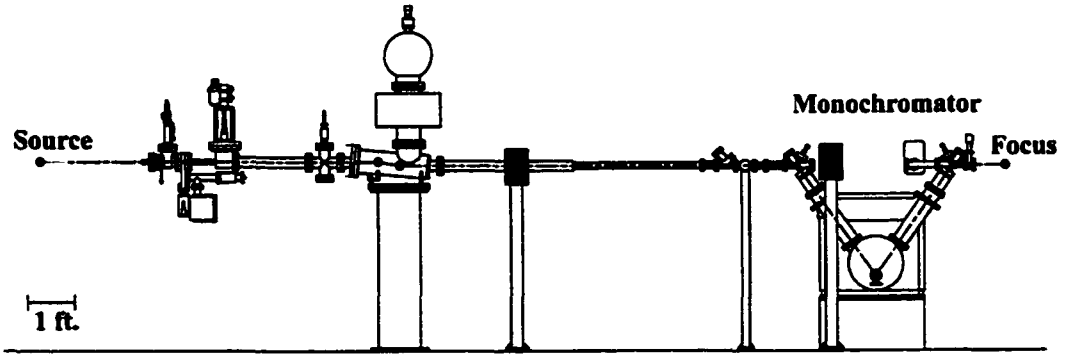

Fig. 4.1. The Aluminum Seya-Namioka Beamline (Al-Seya) at SRC. ● symbolizes an optical element in the beamline. A scale bar is given in the lower left hand corner of the figure. (This drawing is reproduced with permission from Bob Julian, beamline manager.)

This monochromator accepts 30 mrad of radiation from the Aladdin storage ring and focuses this radiation to a spot 2 mm wide by 5 times the width of the exit slit tall (usually 0.5 mm tall in these experiments), with a horizontal divergence of 60 mrad and a vertical divergence of 30 mrad. The Seya monochromator covers the energy range of 5 – 35 eV with a resolution determined by [117] $\Delta\lambda$ (Å) ≈ 9 × slit width (mm), which translates to a resolution of ~8 meV (for 100 μm slits) in the energy region of interest in the present work. The grating used during these measurements was a MgF_2 coated aluminum grating having 1200 lines/mm. The flux through this monochromator at standard SRC operating conditions is shown in Fig. 4.2. After monochromatization, the light passes through a nickel mesh (which was used to monitor beam intensity) and into the sample chamber (cf. Fig. 4.3) where the sample cells are located. The pressure in the sample chamber was maintained in the high 10^{-9} Torr region with a 25 L/s Perkin Elmer ion pump. When open to the monochromator, the pressure in the monochromator and sample chamber was in the low 10^{-8} Torr range.

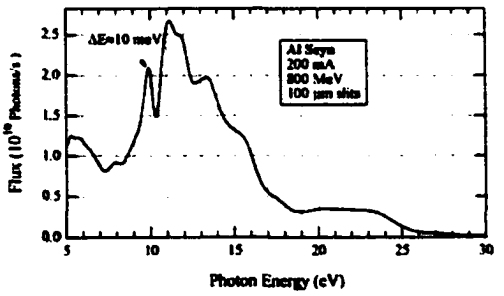

Fig. 4.2. Flux through the Al-Seya beamline with an $AlMgF_2$ grating under normal SRC operating conditions and at 100 μm slits. (This figure is reproduced with permission from Bob Julian, beamline manager.)

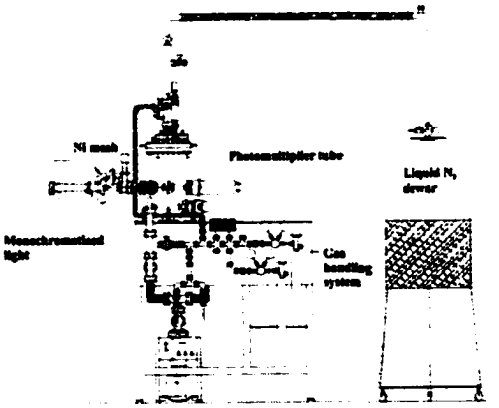

Fig. 4.3. Schematic of the endstation used throughout these experiments.

ii. Sample Cells

Two different sample cells were used in these experiments. Both of these cells are fabricated from copper, allowing for fast temperature equilibration, and are capable of withstanding pressures of up to 100 bar. In order to accurately control the temperature during temperature studies, these cells were attached to a cryostat which was simultaneously cooled with a liquid nitrogen flow (maintained at a constant rate with a manual flow meter) and heated with a resistive heater. The temperature in the cryostat was measured with a calibrated Pt resistor, while the temperature in the cell was measured with a silicon diode. Both temperatures were monitored and regulated with a digital temperature controller (Lakeshore 330 Autotuning Temperature Controller). This digital temperature controller maintains the cryostat temperature by varying the current applied to the resistive heater and can hold the temperature to within ± 1 K.

The first cell (cf. Fig. 4.4a), which (unless otherwise indicated) was the cell used for the experiments reported here, is designed to allow for the simultaneous measurement of transmission and photoionization spectra. This cell is equipped with entrance and exit MgF_2 windows (2 mm thick) and a pair of stainless steel parallel-plate electrodes with a 3 mm spacing oriented perpendicular to the windows. The light path inside this cell is 1.0 cm.

The second cell (cf. Fig. 4.4b) is equipped with an entrance LiF window (2 mm thick) coated with a thin (7 nm) layer of gold to act as an electrode. A second stainless steel electrode is placed parallel to the window with a spacing of 1 mm. When this cell was used, the negative electrode was always the LiF window.

The voltage applied to the electrodes was generated by a Bertan Series 225 High Voltage Power Supply with the current limit set to 3 mA to prevent damage to the detector (Keithley

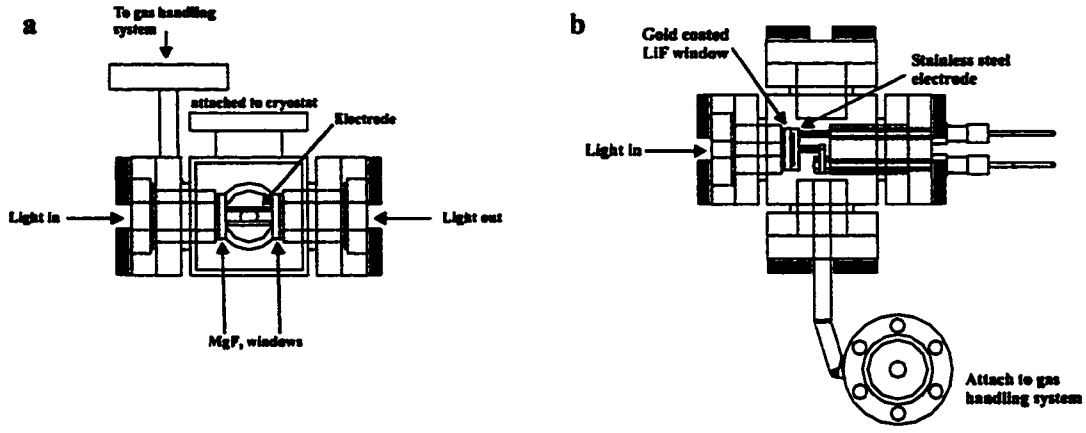

Fig. 4.4. (a) Side view of cell 1. (b) Top view of cell 2. See text for discussion.

486 picoammeter) in the event of an arc in the cell. The voltage applied to the electrodes was 100 V, and all reported spectra are current saturated. (Current saturation was verified by measuring selected spectra at different applied voltages.) Photocurrents within the cells were of the order of 10^{-10} A.

iii. Gas Handling System

The gas handling system (GHS) consists of stainless steel components (except for the sample cells) which are ultrahigh vacuum compatible and bakeable to 100°C. The base pressure of the GHS was in the high 10^{-8} Torr range before the addition of the first sample, and was maintained in the low 10^{-7} Torr range throughout the course of a measurement series by using a 50 L/s Pfieffer Balzers Turbo Molecular Pumping Station. The GHS was tested for leaks after the initial bake and before the insertion of the first sample by flowing He around the joints of the GHS and monitoring the vacuum with a Leybold Inficon Transpector Residual Gas Analysis System. The regulators which control the flow of the perturber gas are single stage high purity regulators (Matheson Gas Products Ultraline 9300 Series) capable of reducing a pressure of 3000 psi to 0–100 psi. The addition of the dopant or the

perturber into the gas handling system was monitored with two MKS capacitance manometers having pressure ranges of 10 mbar and 1 bar. High pressure in the sample cell was monitored with a Setra diaphragm pressure transducer having a pressure range of up to 200 bar.

B. Sample Preparation

A general schematic for a typical arrangement of the GHS is shown in Fig. 4.5. The preparation of a sample was performed in three steps: (1), the addition of the dopant; (2), the addition of the perturber; and (3), the mixing of the sample.

(1) Addition of the dopant: Valve V3 is closed after the GHS has been pumped to a base pressure of high 10^{-8} Torr. Then V2 is opened slightly to allow the desired amount of the dopant into the GHS and subsequently into the sample cell. Once the desired pressure is reached (which is determined from MKS1 and MKS2), V2 and then V6 are closed. V3 is opened to pump the remaining dopant from the GHS. The addition of the perturber is not begun until after the pressure in the GHS has returned to the low 10^{-7} Torr range.

(2) Addition of the perturber: When the GHS has returned to a suitable pressure, the perturber bottle is opened briefly and then closed. After ensuring that V1 is closed, R1 is set to allow 30 psi on the low pressure side of the regulator. V3 is closed and V1 is slowly opened to fill the GHS system to the desired amount, or to 1 bar. (The limit of 1 bar is due to the bellows tube between V4 and V5.)

At this point, if the desired perturber pressure is below 1 bar, V6 is opened to fill the sample cell. The opening of V6 decreases the total pressure to below that desired. Therefore, more perturber is added to bring the total pressure back to the desired pressure.

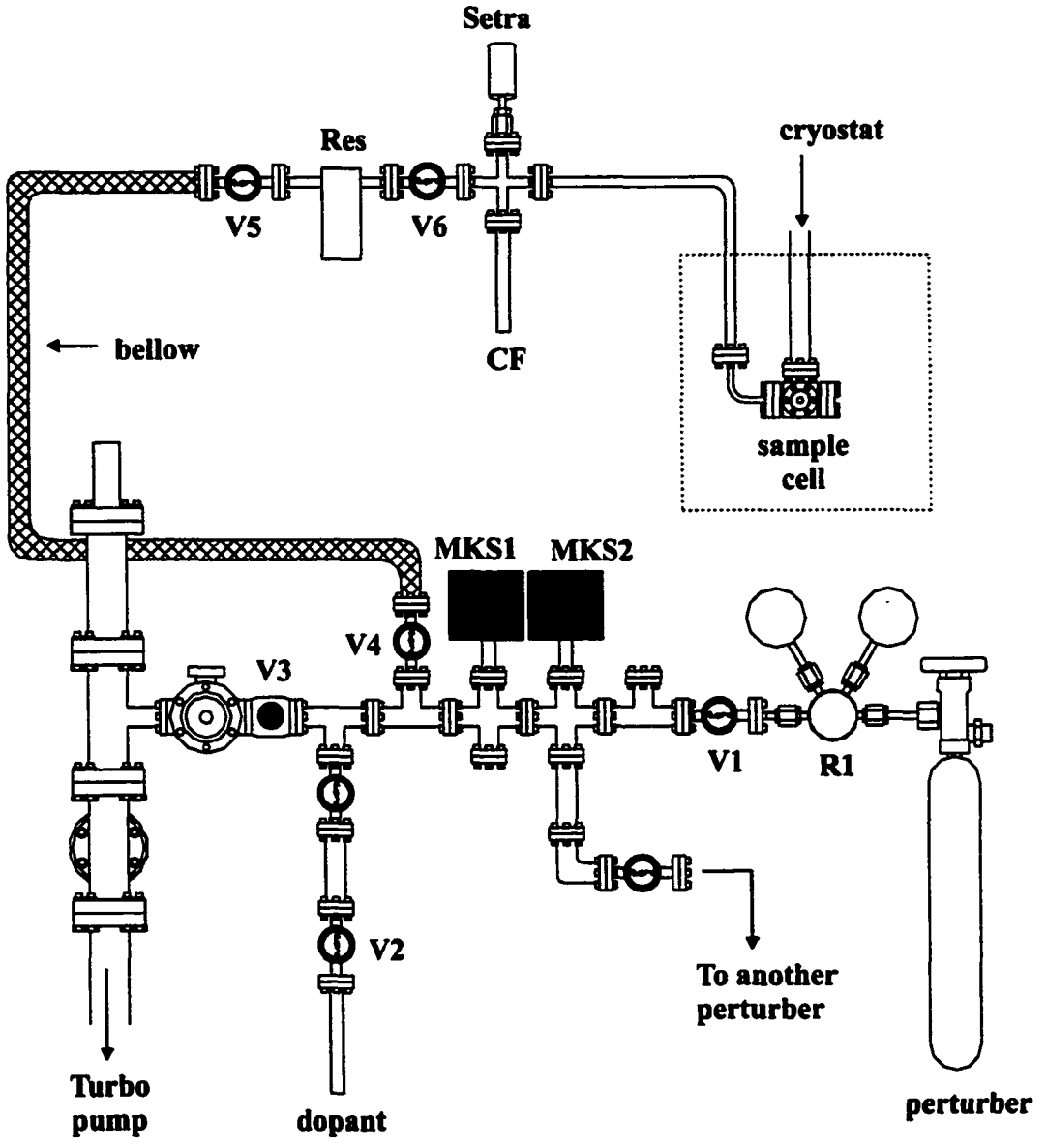

Fig. 4.5. Schematic representation for a typical arrangement of the gas handling system. V1-V6: valves; R1: dual stage regulator; MKS1: pressure manometer (maximum range: 10 mbar); MKS2: pressure manometer (maximum range: 1 bar); Res: reservoir; Setra: pressure manometer (maximum range: 200 bar); and CF: cold finger.

Once the desired pressure is reached, V1 and then V6 are closed. V3 is opened to remove the remaining perturber from the GHS. The sample can then be mixed (cf. step 3).

On the other hand, if the desired perturber pressure is above 1 bar, V6 is opened to fill the sample cell. Again, the opening of V6 decreases the total pressure to below that desired and, therefore, more perturber is added to bring the total pressure back to 1 bar before closing V1 and V6. The reservoir (Res) to cell volume ratio is approximately 3:1. Therefore, the amount needed in the reservoir to achieve the desired pressure in the sample cell can be easily calculated. By either releasing gas using V3 or adding gas using V1, the pressure in the GHS is brought to the calculated amount, and V5 is closed. Liquid N_2 is then placed around the cold finger (CF) to collect the sample. Once the sample is collected, gas stored in Res is collected by opening V6. After the collection process is finished, V6 is closed and V5 is reopened in case continued additions are needed. If the desired pressure needed in Res is above 1 bar, the above filling procedures may have to be repeated several times. Once the final amount of gas has been collected, the liquid N_2 is removed from the cold finger and the sample is thawed using a heat gun. The total pressure in the cell can then be read using the Setra, and the sample can be mixed (cf. step 3).

(3) Mixing of the sample: Steps 1 and 2 do not ensure a homogeneous mixing of the dopant and perturber, since the dopant is added before the perturber. The perturber diffusion from the finger to the cell is slow, thus manual mixing of the dopant and perturber is necessary. This manual mixing is accomplished by collecting all of the sample into CF using liquid N_2 and then releasing the sample back into the cell by warming CF with a heat gun. This freeze-thaw process is repeated at least three times to guarantee homogeneous mixing.

C. Dopant and Perturber Information

The measurement of dopant/perturber interactions with a high perturber number density necessitates the use of crystal windows in the cells. In turn, these windows limit the VUV energy range that can be accessed since the windows also absorb light in this energy region. In these experiments, both MgF_2 windows and occasionally LiF windows are used. The MgF_2 energy cutoff is at 10.8 eV and the LiF energy cutoff is at 11.8 eV. Therefore, the dopants chosen for these experiments must have Rydberg states and ionization thresholds below 11.8 eV. With these limitations in mind, CH_3I, C_2H_5I and C_6H_6 were chosen as dopants.

CH_3I, with the first ($^2E_{3/2}$) ionization threshold at 9.538 eV and the second ($^2E_{1/2}$) ionization threshold at 10.164 eV, has been extensively used as a dopant molecule in the study of molecular Rydberg states [6,7,15-21,38,49-54,63,70-75,85,87,88]. One of the main reasons for the popularity of CH_3I in Rydberg state research is the atomic-like Rydberg absorption and photoionization spectra (cf. Chapter 2).

C_2H_5I was chosen because of its similarity to CH_3I. Moreover, the C_2H_5I first ($\tilde{X}_1\ ^2E_{1/2}$) and second ($\tilde{X}_2\ ^2E_{1/2}$) ionization thresholds [1,118] of 9.349 eV and 9.932 eV, respectively, also fall below the energy cutoffs of the windows in both cells. C_6H_6 was chosen because of a *lack* of any similarity to the previous two dopants. However, like the other dopants, the first ($^2E_{1g}$) ionization threshold [1,119,120] of 9.244 eV is well below the energy cutoff of the windows.

CH_3I and C_6H_6 were both purchased from Aldrich Chemical Company at a purity of 99.5% and 99.9+%, respectively. C_2H_5I was purchased at a purity of 99% from Sigma. HI (which was studied unsuccessfully, as discussed in Chapter 7) was purchased from Matheson

Gas Products at a purity of 99.9%. These dopants were used without further purification, and the absence of contamination was verified by comparisons with previously published absorption and photoionization spectra. All dopants (with the exception of HI) were degassed with three liquid nitrogen freeze-pump-thaw cycles before the initial addition into the GHS. HI was degassed once with a liquid nitrogen freeze-pump-thaw cycle in order to remove a back pressure of H_2 gas.

All of the perturbers used in these experiments were purchased from Matheson Gas Products. The perturbers chosen for this study, along with the purity of these gases, are as follows: Ar, 99.9999%; N_2, 99.9999%; CF_4, 99.999%; *c*-C_4F_8, 99.98%; CO_2, 99.995% and SF_6, 99.996%. All of the perturber gases were used without further purification. No photocurrent was detected in any of the perturber gases in the spectral region of interest in the absence of a dopant.

D. Data Acquisition and Analysis

The data acquisition system is presented schematically in Fig. 4.6. All data were collected with an Intel 386 SX 25 computer which also controlled the monochromator. Both the monochromator control program and the data acquisition program were supplied and maintained by SRC, and were written using National Instruments LabVIEW software. During an experimental run, up to three measurements were made simultaneously: (1) the current collected at the electrodes, (2) the photomultiplier (Electron tubes model 9813B) output current, and (3) the photoemission current from the nickel grid intercepting the beam prior to the experimental cell. All three measurements were obtained with Keithley 486 picoammeters having built-in GPIB interfaces. These data, once acquired, were transferred through TCP/IP to an Intel 486 laptop computer for storage and initial data analysis.

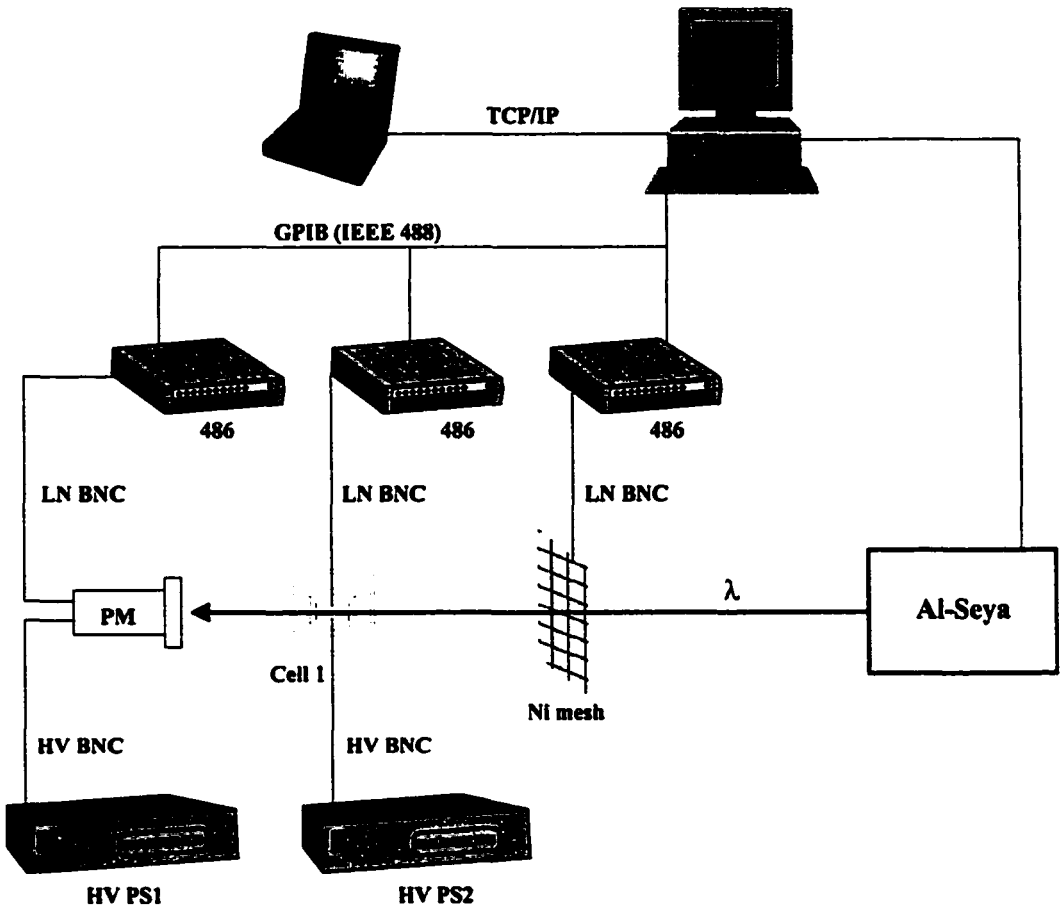

Fig. 4.6. Schematic representation of the data acquisition system. λ, monochromatic synchrotron radiation; PM, photomultiplier; 486, Keithley 486 picoammeter; LN BNC, low noise BNC cable; HV BNC, high voltage BNC cable; HV PS1, Keithley 247 High Voltage power supply; HV PS2, Bertan Series 225 High Voltage power supply.

Since the intensity of the synchrotron radiation entering the monochromator decays over time, all photoionization spectra are normalized to the photoemission current from the Ni grid intercepting the beam prior to the experimental cell. Transmission spectra (which are reported here as absorption = 1 - transmission) are normalized both to the incident light intensity and to the empty cell transmission. All spectra were measured at room temperature, unless otherwise indicated. All photoionization spectra of CH_3I are intensity normalized to unity at the same spectral feature above the $^2E_{3/2}$ ionization threshold; all C_2H_5I photoionization spectra are normalized to unity at the same spectral feature above the $\tilde{X}_1\ ^2E_{1/2}$ ionization threshold; and all C_6H_6 photoionization spectra are normalized to unity at the same spectral feature above the $^2E_{1g}$ ionization threshold. Spectral peak areas were obtained by integrating a gaussian deconvolution of the subthreshold peaks calculated using Wavemetrics Igor 3.1 (cf. Fig. 4.7). The exponential background areas were obtained by integrating an exponential least-square fit (calculated using Wavemetrics Igor 3.1) to the background of the subthreshold spectrum (cf. Fig. 4.7).

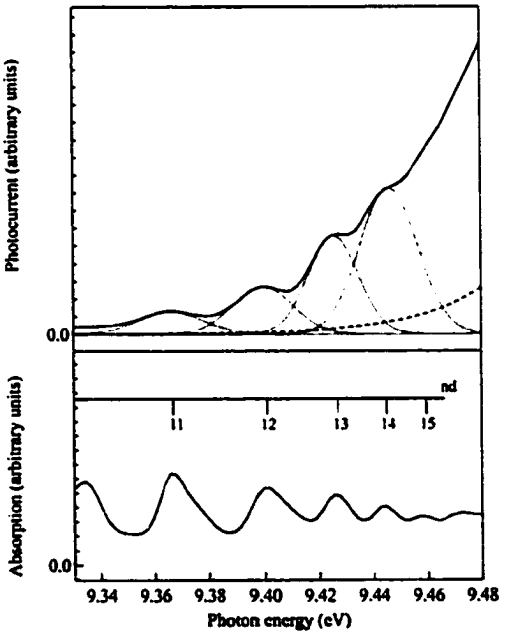

Fig. 4.7. Subthreshold photoionization spectra of 0.1 mbar CH_3I doped into 50 mbar of SF_6 (0.13×10^{19} cm^{-3}). Absorption of pure CH_3I (Cell 1, 200 μm slits): 0.1 mbar. ···· is an example of a gaussian fit used to obtain peak areas. – – – represents a fit to the exponential background. —— is the experimental spectrum, and is equal to the sum of the underlying curves.

Chapter 5. Electron Scattering Lengths of Fluorinated Compounds

In this Chapter, the investigation of dopant/perturber interactions begins with the evaluation of the zero-kinetic-energy electron scattering lengths of fluorinated gases using the perturber-induced energy shifts of high-n Rydberg states. After finishing this determination of electron scattering lengths and cross-sections, an analysis of the subthreshold photoionization structure present in some dopant/perturber systems is used to probe the nature of dopant/perturber interactions in static systems (cf. Chapter 6).

A. Introduction

The interaction of fluorinated gases such as CF_4, c-C_4F_8 and SF_6 with low-energy [121-126] and high-energy electrons [123,127-129] has received increasing attention, primarily due to the importance of these gases to the semiconductor industry [123,130,131], and to the involvement of these gases in stratospheric photochemistry [132,133]. In fact, many fluorinated gases are used as sources for reactive species in plasma etching [134,135]. Furthermore, these gases have been used [136], or have the potential to be used [124] as insulators in high voltage switches.

In order to model accurately the behavior of fluorinated gases in plasma etching processes, the interaction between the gas and low-energy electrons must be better understood. However, the measurement of low-energy electron scattering cross-sections and low-energy electron attachment rates for fluorinated gases can be extremely difficult because of the large electronegativities of these molecules. For example, a typical method for studying electron/gas interactions, the electron swarm method, depends on the electron number density remaining constant throughout the experiment [137]. When a molecule has a large electronegativity, however, the electron number density will vary during the

measurement as a result of electron attachment in addition to electron induced ionization, thus complicating data interpretation [137]. For such molecular species, the measurement of zero-kinetic-energy electron scattering cross-sections is particularly problematic [123,124,126,137].

An alternative method for determining the zero-kinetic-energy electron scattering cross-section, involving the perturber-induced energy shifts of high-n Rydberg states of the dopant molecule, was introduced in Chapter 3.A. In this method, a dopant molecule having a Rydberg series observable in photoabsorption and/or photoionization spectroscopy is mixed with a perturber gas of interest. As the perturber concentration is increased, the dopant high-n Rydberg state energies shift as a result of dopant/perturber interactions. These energy shifts can be modeled using Eqs. (3.1), (3.2), and (3.12), or

$$\Delta = \Delta_{sc} + \Delta_{pol} = -\left(\frac{2\pi\hbar^2}{m_e}\right) A\,\rho_P - 10.78\left(\frac{\alpha e^2}{2}\right)^{2/3} (\hbar v)^{1/3}\,\rho_P\,, \qquad (5.1)$$

obtained from a theory by Fermi [11] (cf. Chapter 3.A.i), as modified by Alekseev and Sobel'man [6,12,70] (cf. Chapter 3.A.ii). By experimentally determining the total energy shift Δ, the electron scattering length A can be evaluated using Eq. (5.1). Once the electron scattering length is known, the zero-kinetic-energy electron scattering cross-section is calculated from [11]

$$\sigma = 4\pi A^2\,. \qquad (5.2)$$

However, as discussed in Chapter 3.A, recent questions [13] have arisen about the ρ_P dependence of the polarization term in Eq. (5.1). Therefore, before using Eq. (5.1) to determine the zero-kinetic-energy electron scattering lengths and cross-sections for the fluorinated gases of CF_4, c-C_4F_8 and SF_6, the zero-kinetic-energy electron scattering length

of Ar was determined from the shift of C_2H_5I high-*n* Rydberg states, and compared to the electron scattering length obtained from swarm methods [64].

B. Electron Scattering Length of Ar [14]

Since Ar is transparent in the region of the first and second ionization energies of C_2H_5I, the perturber-induced energy shifts of C_2H_5I Rydberg states can be monitored using both the autoionization spectra and the photoabsorption spectra of C_2H_5I/Ar. The transparency of Ar also insures that these shifts can be determined for a large range of Ar number densities ρ_{Ar}, which permits one to check the validity of Eq. (5.1) in the density range of interest.

The photoabsorption spectra and autoionization spectra of C_2H_5I doped into varying ρ_{Ar} are presented in Fig. 5.1. The shift in the first and second ionization energies ΔI as a

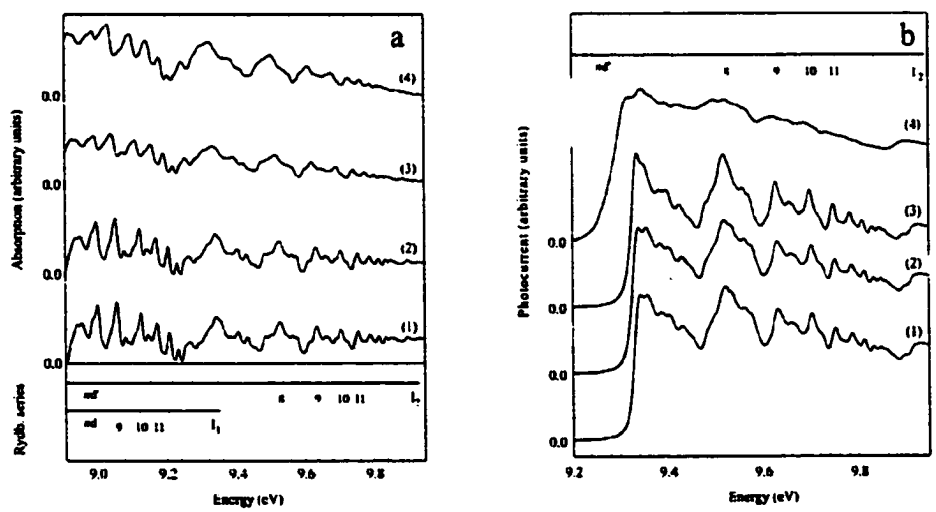

Fig. 5.1. **(a)** Photoabsorption spectra of C_2H_5I/Ar: (1) 0.5 mbar C_2H_5I and C_2H_5I doped into varying Ar number densities ρ_{Ar} (10^{20} cm^{-3}): (2) 0.024, (3) 2.4, and (4) 4.9. The assignment given at the bottom corresponds to the pure C_2H_5I spectrum. **(b)** Autoionization spectra of C_2H_5I/Ar: (1) 0.5 mbar C_2H_5I and C_2H_5I doped into varying ρ_{Ar} (10^{20} cm^{-3}): (2) 0.024, (3) 0.65, and (4) 3.6. The assignment given at the top corresponds to the pure C_2H_5I spectrum. For both **(a)** and **(b)**, the concentration of C_2H_5I was kept below 10 ppm in Ar. See Chapter 4 for experimental details.

function of ρ_{Ar} is shown in Fig. 5.2. (The values for the discrete *n*d and *n*d′ Rydberg states of C_2H_5I along with I_1 and I_2, obtained by fitting these Rydberg states to the Rydberg equation, are listed in Appendix 1.A.) Fig. 5.2 demonstrates that the red shift of the ionization energy depends linearly upon ρ_{Ar} over the entire density range and, therefore, can be modeled using Eq. (5.1). The slope of the linear fit for ΔI (obtained by a linear least-square fit of Fig. 5.2) is $\Delta/\rho_{Ar} = -4.9 \times 10^{-23}$ eV cm^3. Using the value [65,66] $\alpha = 1.64 \times 10^{-24}$ cm^3, one finds from Eq. (5.1) a zero-kinetic-energy electron scattering length of $A = -0.086$ nm. This value agrees well with $A = -0.089$ nm obtained from similar measurements involving CH_3I [6,63] and C_6H_6 [138] doped into Ar, and $A = -0.082$ nm obtained from field ionization measurements of CH_3I doped into dense Ar [71]. Furthermore, this value agrees with the value of $A = -0.090$ nm evaluated from electron swarm experiments [64]. From these measurements, we conclude that Eq. (5.1) can continue to be used to evaluate the zero-kinetic-energy electron scattering lengths of perturbers and, therefore, this equation is applied to obtain the zero-kinetic-energy electron scattering lengths of various fluorinated gases (see below).

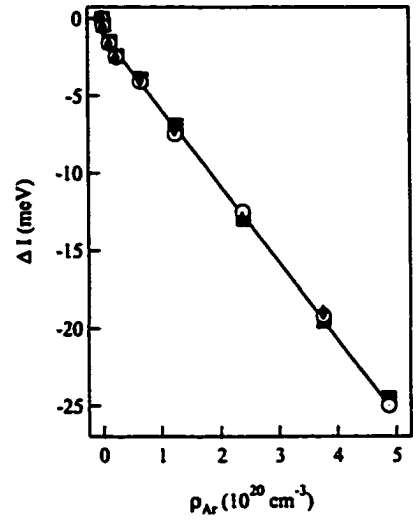

Fig. 5.2. Shifts of the ionization energies ΔI of C_2H_5I obtained from fitting the assigned spectra (e.g., Fig. 5.1) to the Rydberg equation, plotted vs. Ar number density ρ_{Ar}. ■, I_1 from C_2H_5I absorption; ○, I_2 from C_2H_5I absorption; ♦, I_2 from C_2H_5I autoionization. (The error in the energy for each point is ± 3 meV.)

C. Electron Scattering in Fluorinated Gases

i. CF_4 [15]

The autoionization spectra of CH_3I and the photoabsorption spectra of C_2H_5I doped into varying CF_4 number densities ρ_{CF_4} are shown in Figs. 5.3a and 5.3b, respectively. The measured photoionization spectra of C_2H_5I doped into CF_4 and the photoabsorption spectra of CH_3I doped into CF_4 are not shown for brevity. (The values for the discrete *n*d and *n*d′ CH_3I and C_2H_5I Rydberg states as a function of ρ_{CF_4}, along with the values of I_1 and I_2 extracted from these measurements for each dopant, are given in Appendix 1.A.) In Fig. 5.4, the shift in the ionization energy is plotted as a function of ρ_{CF_4}. As was the case for C_2H_5I/Ar (cf. Section B), a red shift which is linearly dependent upon ρ_{CF_4} is observed. The

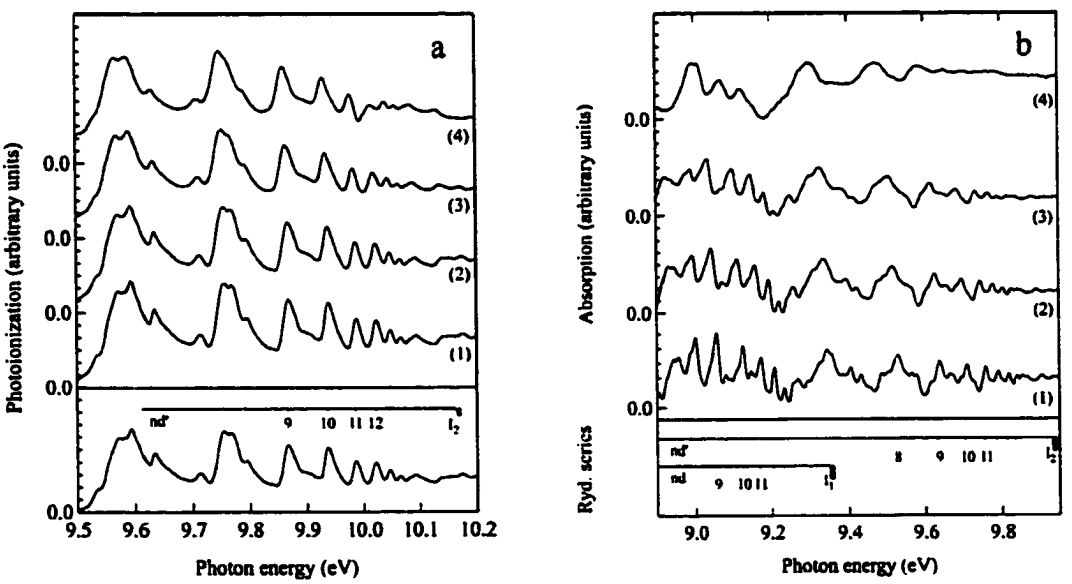

Fig. 5.3. **(a)** Photoionization spectra of pure CH_3I (0.1 mbar) and CH_3I (0.1 mbar) doped into varying CF_4 number densities ρ_{CF_4} (10^{20} cm^{-3}): (1) 0.073, (2) 0.23, (3) 0.74 and (4) 1.30. **(b)** Photoabsorption spectra of C_2H_5I/CF_4: (1) 0.5 mbar C_2H_5I and C_2H_5I doped into varying ρ_{CF_4} (10^{20} cm^{-3}): (2), 1.22, (3) 2.43 and (4) 6.08. The concentration of C_2H_5I was kept below 10 ppm in CF_4. The assignment given at the bottom corresponds to the pure C_2H_5I spectrum. See Chapter 4 for experimental details.

slope of this shift (obtained by a linear least-square regression analysis) is Δ/ρ_{CF_4} = - 8.648 x 10^{-23} eV cm^3. Using the value [139] $\alpha = 3.838 \times 10^{-24}$ cm^3 for CF_4 in Eq. (3.12) gives a polarization shift of Δ_{pol}/ρ_{CF_4} = - 3.38 x 10^{-26} eV cm^3. Substituting Δ_{pol}/ρ_{CF_4} and Δ/ρ_{CF_4} into Eq. (5.1) and solving for A leads to a zero-kinetic-energy electron scattering length of A = - 0.180 ± 0.003 nm. Therefore, from Eq. (5.2), the zero-kinetic-energy electron scattering cross-section for CF_4 is $\sigma = 4.1 \pm 0.2 \times 10^{-15}$ cm^2.

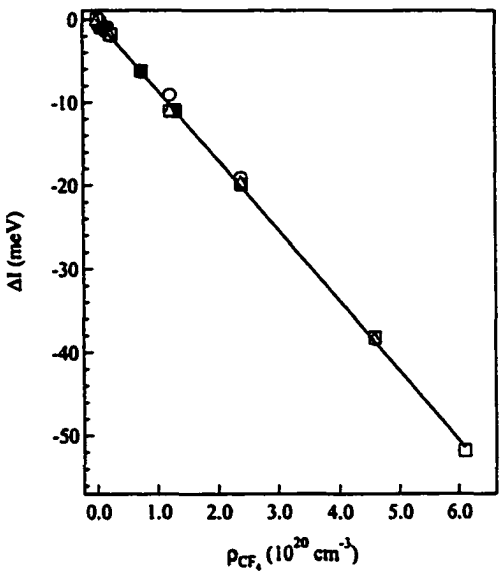

Fig. 5.4. Shifts of the ionization energies ΔI of CH_3I and C_2H_5I, obtained from fitting the assigned spectra (e.g., Fig. 5.3) to the Rydberg equation, plotted vs. CF_4 number density ρ_{CF_4}. ●, I_1 CH_3I photo-absorption; ■, I_2 CH_3I photoabsorption; ▲, I_2 CH_3I photoionization; ○, I_1 C_2H_5I photo-absorption; □, I_2 C_2H_5I photoabsorption; △, I_2 C_2H_5I photoionization. (The error in the energy for each point is ± 3 meV.) The solid line represents a linear least-square fit to the data.

Current estimates of low-energy electron scattering cross-sections for CF_4 range from a low of 1.269 x 10^{-15} cm^2, obtained by averaging all of the currently known low-energy electron scattering cross-section measurements [123], to a high of 8 x 10^{-15} cm^2 [140] computed using the continuum MS-$X\alpha$ method described by Davenport [141]. The value obtained here for the zero-kinetic-energy cross-section, therefore, falls within these two limits.

ii. *c*-C_4F_8 [15]

In Fig. 5.5, the photoionization spectra of CH_3I and of CH_3I doped into various *c*-C_4F_8 number densities $\rho_{c\text{-}C_4F_8}$ are shown. (The energy positions of the discrete nd' Rydberg states

along with I_2 extracted from fitting these assignments to the Rydberg equation are given in Appendix 1.A.) Similar to the analysis given in the previous Section, Fig. 5.6 presents the change in the ionization energy of CH_3I as a function of c-C_4F_8 number density $\rho_{c\text{-}C_4F_8}$. As was the case for CF_4, a red shift which is linearly dependent upon $\rho_{c\text{-}C_4F_8}$ is observed. The slope of the straight line (obtained from a linear least-square regression analysis) is $\Delta/\rho_{c\text{-}C_4F_8}$ = - 29.57 ± 0.51 x 10^{-23} eV cm^3. Using the value [142] α = 7.37 x 10^{-24} cm^3 for c-C_4F_8, and following the same prescription as that described above for Ar and CF_4, gives a zero-kinetic-energy electron scattering length of A = - 0.618 ± 0.012 nm for c-C_4F_8.

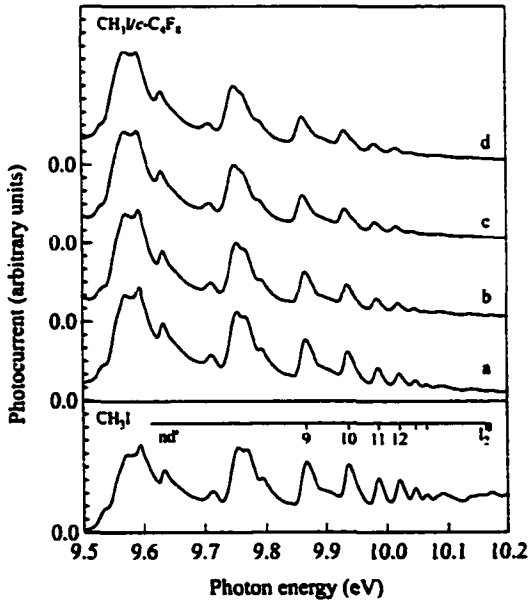

Fig. 5.5. Photoionization spectra of pure CH_3I (0.1 mbar) and CH_3I (0.1 mbar) doped into varying c-C_4F_8 number densities $\rho_{c\text{-}C_4F_8}$ (10^{19} cm^{-3}): (a) 0.12; (b) 0.73; (c) 1.81 and (d) 2.42. See Chapter 4 for experimental details.

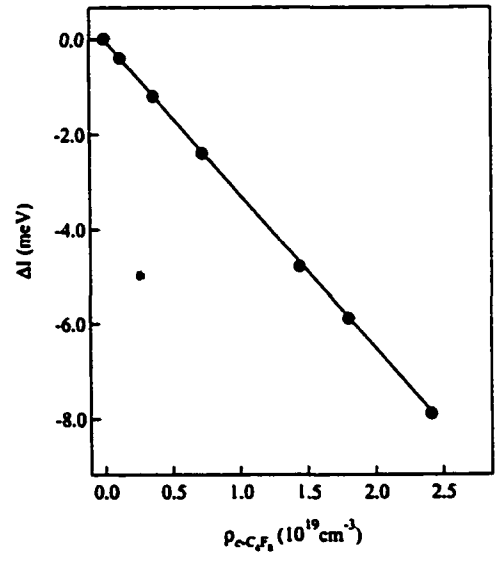

Fig. 5.6. Shift of the second ionization energy ΔI of CH_3I, obtained from fitting the assigned spectra (e.g., Fig. 5.5) to the Rydberg equation, plotted vs. c-C_4F_8 number density $\rho_{c\text{-}C_4F_8}$. (The error in the energy for each point is ± 3 meV.) The solid line represents a linear least-square fit to the data.

Therefore, the zero-kinetic-energy electron scattering cross-section for c-C_4F_8 is $\sigma = 4.8 \pm 0.2 \times 10^{-14}$ cm^2 from Eq. (5.2).

Recent attempts by Sanabia and co-workers [143] to measure the low energy electron scattering cross-section gave $\sigma = 4.8 \times 10^{-15}$ cm^2 for an electron energy of 1 eV, which from our measurements is one order of magnitude too low. However, the sharp increase in the electron scattering cross-section of c-C_4F_8 below 1 eV made these earlier low-energy electron measurements unreliable [143].

iii. SF_6 [16]

Autoionization spectra of CH_3I and CH_3I doped into varying SF_6 number densities ρ_{SF_6} are presented in Fig. 5.7. (The energy positions of the discrete CH_3I nd′ Rydberg states, as well as the values of I_2 extracted from a fit of the assigned spectra to the Rydberg equation, are given in Appendix 1.A.) A plot of the shift in the ionization energy ΔI as a function of SF_6 number density ρ_{SF_6} is shown in Fig. 5.8. The slope of the linear fit for the red-shifting ΔI (obtained by a linear least-square regression analysis of Fig. 5.8) is $\Delta/\rho_{SF_6} = -24.72 \pm 0.46 \times 10^{-23}$ eV cm^3. Similar to the above analyses, using the value of [144] $\alpha = 6.54 \times$

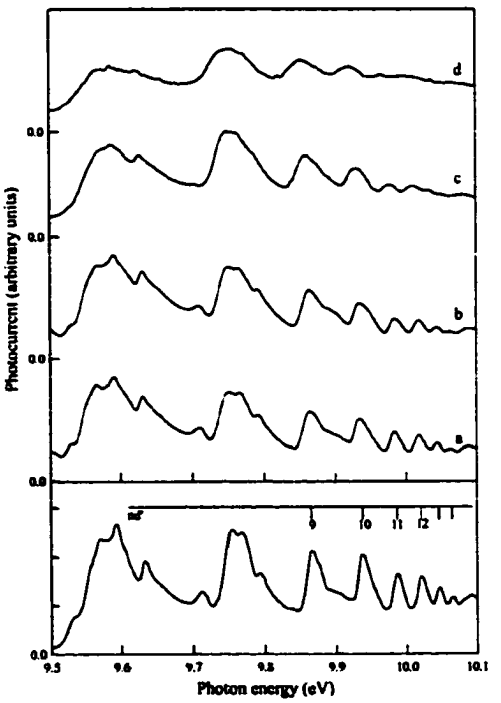

Fig. 5.7. Photoionization spectra of pure CH_3I (0.1 mbar) and CH_3I (5 mbar) doped into varying SF_6 number densities ρ_{SF_6} (10^{19} cm^{-3}): (a) 0.12, (b) 1.97, (c) 5.02 and (d) 9.75. See Chapter 4 for experimental details.

10^{-24} cm^3 to calculate Δ_{pol} and substituting this value along with the value for Δ/ρ_{SF_6} into Eq. (5.1) gives, after rearrangement, a zero-kinetic-energy electron scattering length of A = - 0.484 ± 0.010 nm. Therefore, the zero-kinetic-energy electron scattering cross-section, computed from Eq. (5.2), is σ = 2.94 ± 0.13 x 10^{-14} cm^2. This cross-section value should be compared to the value $\sigma \approx 2 \times 10^{-14}$ cm^2 determined by very slow electron attachment cross-section measurements in an electron beam collision chamber method [145].

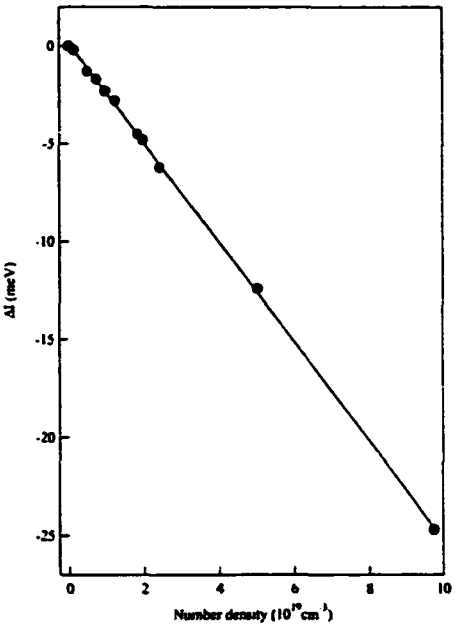

Fig. 5.8. Shift of the second ionization energy ΔI of CH_3I, obtained by fitting the assigned spectra (cf. Fig. 5.7) to the Rydberg equation, plotted vs. SF_6 number density ρ_{SF_6}. (The error in the energy for each point is ± 3 meV.) The solid line represents a linear least-square fit to the data.

D. Summary of Results

In this Chapter, the perturber-induced energy shifts of the high-n Rydberg states of CH_3I and C_2H_5I have been used to evaluate the zero-kinetic-energy electron scattering lengths and cross-sections for several fluorinated gases [15,16]. A summary of the electron scattering lengths and cross-sections determined is given in Table 5.1. Furthermore, CF_4, c-C_4F_8 and

Table 5.1. Summary of the total shift rates Δ/ρ_P, scattering lengths A and cross-sections σ for the fluorinated gases [15,16].

Perturber	Δ/ρ_P (10^{-23} eV cm^3)	A (nm)	σ (10^{-14} cm^2)
CF_4	- 8.648 ± 0.172	-0.180 ± 0.003	0.41 ± 0.02
c-C_4F_8	-29.57 ± 0.51	-0.618 ± 0.012	4.8 ± 0.2
SF_6	-24.72 ± 0.46	-0.484 ± 0.010	2.9 ± 0.1

SF_6 can be added to the growing list of perturbers which have had electron scattering lengths and cross-sections evaluated using perturber-induced energy shifts of high-n Rydberg states (cf. Table 3.1). To the best of our knowledge, this work represents the first determination of the zero-kinetic-energy electron scattering length of SF_6 using high-n Rydberg states, and the first direct determination of the zero-kinetic-energy electron scattering lengths of CF_4 and c-C_4F_8.

Chapter 6. Subthreshold Photoionization

A. Introduction

As mentioned in Chapter 3.C, photoionization structure has been observed to occur at energies lower than the first ionization threshold of the unperturbed dopant in many dopant/perturber systems [6,14,17-21,73,75,85-115]. In this Chapter, subthreshold photoionization spectra for the dopants D = CH_3I, C_2H_5I and C_6H_6 and for the perturbers P = Ar, CF_4, *c*-C_4F_8, CO_2, N_2 and SF_6 are presented and analyzed.

In some instances [14,17-21,73,75,87,88], subthreshold photoionization structure has been shown to track the photoabsorption of discrete dopant Rydberg states in the same energy region which, in turn, permitted the evaluation of electron scattering lengths in highly absorbing perturber media [14,17,21,73,75]. Later, in Section B of this Chapter, the energy shifts of the subthreshold photoionization structure of CH_3I doped into CF_4, *c*-C_4F_8 and SF_6 [17], as well as C_2H_5I and C_6H_6 doped into SF_6 [14], will be used to determine the zero-kinetic-energy electron scattering lengths of these perturbers. Since the scattering lengths determined here agree well with those presented in Chapter 5 (cf. Table 5.1), one may conclude that this subthreshold structure does indeed arise from the ionization of high-*n* Rydberg states. However, the nature of the processes leading to subthreshold photoionization is not well understood.

Subthreshold photoionization in dopant/perturber systems has traditionally been explained as resulting from the collisional transfer of translational, rotational or vibrational energy from a perturber to an excited state dopant (cf. Chapter 3.C.i). However, the photoionization spectra of CH_3I [17,20,85,87,88] and of CH_3I doped into Xe [21], Ar [6,18,20], CF_4 [19], *c*-C_4F_8 [19], CO_2 [18, 73], N_2 [18,75] and SF_6 [17,20] exhibit rich

subthreshold structure beginning at least 0.17 eV below the CH_3I ionization limit, which is much too low an onset to be accounted for by collisional transfer of perturber translational energy to an excited-state CH_3I molecule. (Analogous results have also been obtained for C_2H_5I and C_6H_6 doped into SF_6 [14,20].) In Section C of this Chapter, the exponential background underlying the first ionization threshold of CH_3I is shown to be related to translational collisional ionization [146].

Rotational and vibrational energy transfer from the perturber to the excited-state dopant can be excluded as potential mechanisms because of the observation of similar subthreshold spectra in systems containing atomic and molecular perturbers. A number of temperature dependent measurements of subthreshold photoionization in these systems [14,17-19] has also excluded rotational and hot-band autoionization (cf. Chapter 3.C.ii) as possible mechanisms leading to subthreshold photoionization. Some of these temperature measurements will be reviewed in Section C of this Chapter. Finally, photochemistry can be ruled out as a possible subthreshold photoionization mechanism on the basis of energetics (cf. Section D).

While studying CH_3I, Ivanov and Vilesov [87,88] proposed that subthreshold photoionization in CH_3I could proceed through electron attachment and associative ionization. However, these authors concluded that the actual processes leading to subthreshold photoionization could only be determined by mass analysis of the primary charged species in a molecular beam study. In Section E of this Chapter, a number density study of the subthreshold photoionization structure of CH_3I, C_2H_5I and C_6H_6 perturbed by Ar, CF_4, *c*-C_4F_8, CO_2, N_2 and SF_6 is presented. This study allows one to probe the processes leading to subthreshold photoionization without using mass analysis.

From this systematic number density study, it is shown that subthreshold photoionization involving C_2H_5I and C_6H_6 proceeds through electron attachment to the perturber and dopant/perturber heteromolecular dimerization. CH_3I subthreshold photoionization, on the other hand, is generated by electron attachment either to CH_3I or to the perturber, and by homomolecular CH_3I dimerization or heteromolecular CH_3I/perturber dimerization. By varying ρ_D and ρ_P separately, the effective rate constants for electron attachment and associative ionization are determined. Finally, the effects of electron affinity (of D or P) on the effective rate constant for electron attachment, and the effects of the ground-state polarizability (of D or P) on the effective rate constant for associative ionization are discussed.

B. Electron Scattering Lengths of Fluorinated Gases

As mentioned in the previous Section, the subthreshold photoionization structure in some dopant/perturber systems has been identified as arising from the ionization of high-*n* Rydberg states [14,17-21,73,75,87,88]. If this structure is generated from high-*n* Rydberg states, the subthreshold structure should shift linearly as a function of the perturber number density ρ_P, thus allowing for the determination of the zero-kinetic-energy electron scattering length of the perturber using Eq. (5.1), and the zero-kinetic-energy electron scattering cross-section using Eq. (5.2). In Fig. 6.1a, subthreshold photoionization spectra of CH_3I perturbed by various CF_4 number densities ρ_{CF_4} are presented. The shift in the first ionization energy ΔI of CH_3I as a function of ρ_{CF_4} is plotted in Fig. 6.1b. (The values for the discrete *n*d CH_3I Rydberg states, along with the value of I_t extracted from these measurements, as a function of ρ_{CF_4} are given in Appendix 1.B.) The slope of the red shift observed in Fig. 6.2b, obtained using a linear least-square regression analysis, is $\Delta/\rho_{CF_4} = -8.337 \times 10^{-23}$ eV cm^3. Using the

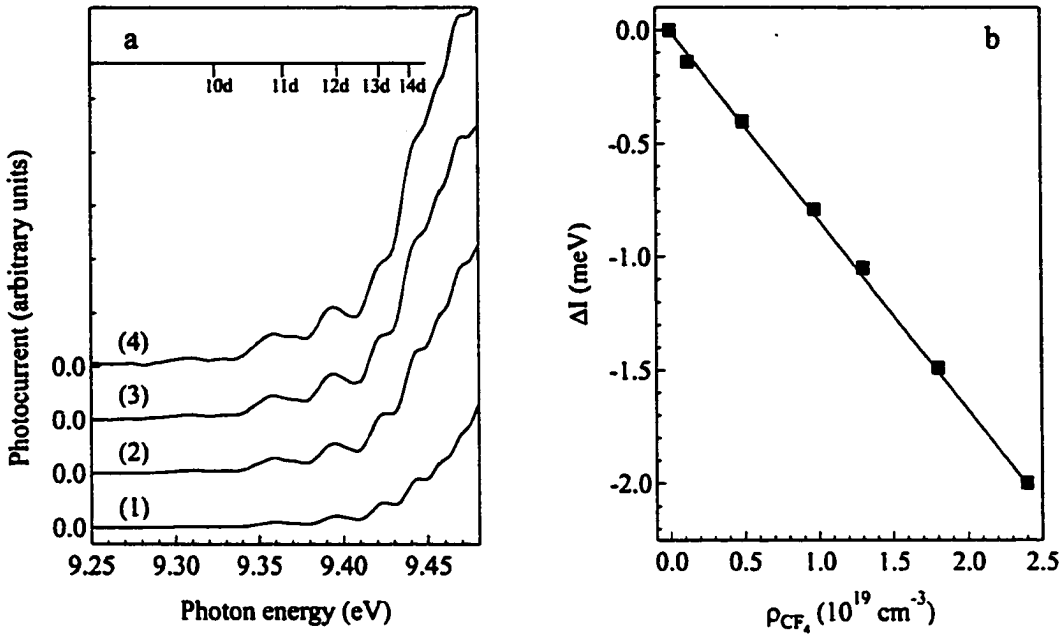

Fig. 6.1. **(a)** Subthreshold photoionization spectra of 0.061 x 10^{19} cm^{-3} CH_3I perturbed by varying CF_4 number densities ρ_{CF_4} (10^{19} cm^{-3}): (1) 0.12, (2) 0.97, (3) 1.8, and (4) 2.4. See Chapter 4 for experimental details. **(b)** Shift of the first ionization energy ΔI of CH_3I obtained from fitting the assigned spectra (e.g., (a)) to the Rydberg equation, plotted vs. ρ_{CF_4}. The solid line represents a linear least-square fit to the data. (The error in the energy for each point is ± 3 meV.)

same procedure described in Chapter 5, the zero-kinetic-energy electron scattering length $A = -0.173 \pm 0.009$ nm and the zero-kinetic-energy electron scattering cross-section $\sigma = 3.8 \pm 0.4 \times 10^{-15}$ cm^2 are obtained.

The subthreshold photoionization spectra of CH_3I perturbed by various c-C_4F_8 number densities $\rho_{c\text{-}C_4F_8}$ are shown in Fig. 6.2a, and the shift in the first ionization energy ΔI of CH_3I as a function of $\rho_{c\text{-}C_4F_8}$ is presented in Fig. 6.2b. (The values for the discrete nd CH_3I Rydberg states, along with the value of I_i extracted from these measurements, as functions of $\rho_{c\text{-}C_4F_8}$ are given in Appendix 1.B.) The slope of the red shift in Fig. 6.2b, obtained using a linear least-square regression analysis, is $\Delta/\rho_{c\text{-}C_4F_8} = -29.46 \pm 0.63 \times 10^{-23}$ eV cm^3.

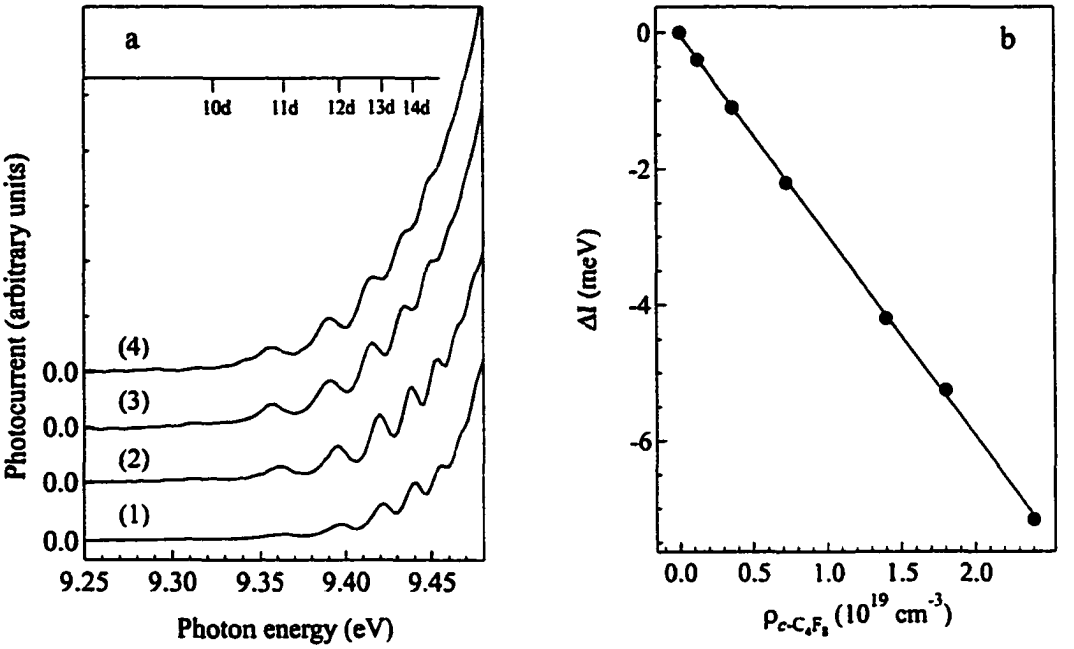

Fig. 6.2. **(a)** Subthreshold photoionization spectra of 0.00024 x 10^{19} cm^{-3} CH_3I perturbed by varying *c*-C_4F_8 number densities $\rho_{c\text{-}C_4F_8}$ (10^{19} cm^{-3}): (1) 0.12, (2) 0.72, (3) 1.8, and (4) 2.4. See Chapter 4 for experimental details. **(b)** Shift of the first ionization energy of CH_3I obtained from fitting the assigned spectra (e.g., (a)) to the Rydberg equation, plotted vs. $\rho_{c\text{-}C_4F_8}$. The solid line represents a linear least-square fit to the data. (The error in the energy for each point is ± 3 meV.)

Therefore, Eq. (5.1) and (5.2) give the zero-kinetic-energy scattering length and cross-section A = - 0.600 ± 0.025 nm and σ = 4.8 ± 0.4 x 10^{-14} cm^2, respectively.

The subthreshold photoionization spectra of CH_3I, C_2H_5I and C_6H_6 perturbed by various SF_6 number densities ρ_{SF_6} are shown in Fig. 6.3a, 6.3b and 6.3c, respectively. The shift in the first ionization energies ΔI of CH_3I, C_2H_5I and C_6H_6 as a function of ρ_{SF_6} are given in Fig. 6.4. (The values for the discrete *n*d Rydberg states of CH_3I, *n*d Rydberg states of C_2H_5I and *n*R′ Rydberg states of C_6H_6 are given in Appendix 1.B, along with the values of I_t extracted from these measurements.) The slope of the straight line (obtained from a linear least-square

regression analysis) is $\Delta/\rho_{SF_6} = -24.90 \pm 0.55 \times 10^{-23}$ eV cm^3. Therefore, from Eq. (5.1) and (5.2), the zero-kinetic-energy electron scattering length and cross-section of SF_6 are A = - 0.487 ± 0.019 nm and $\sigma = 3.0 \pm 0.3 \times 10^{-14}$ cm^2, respectively.

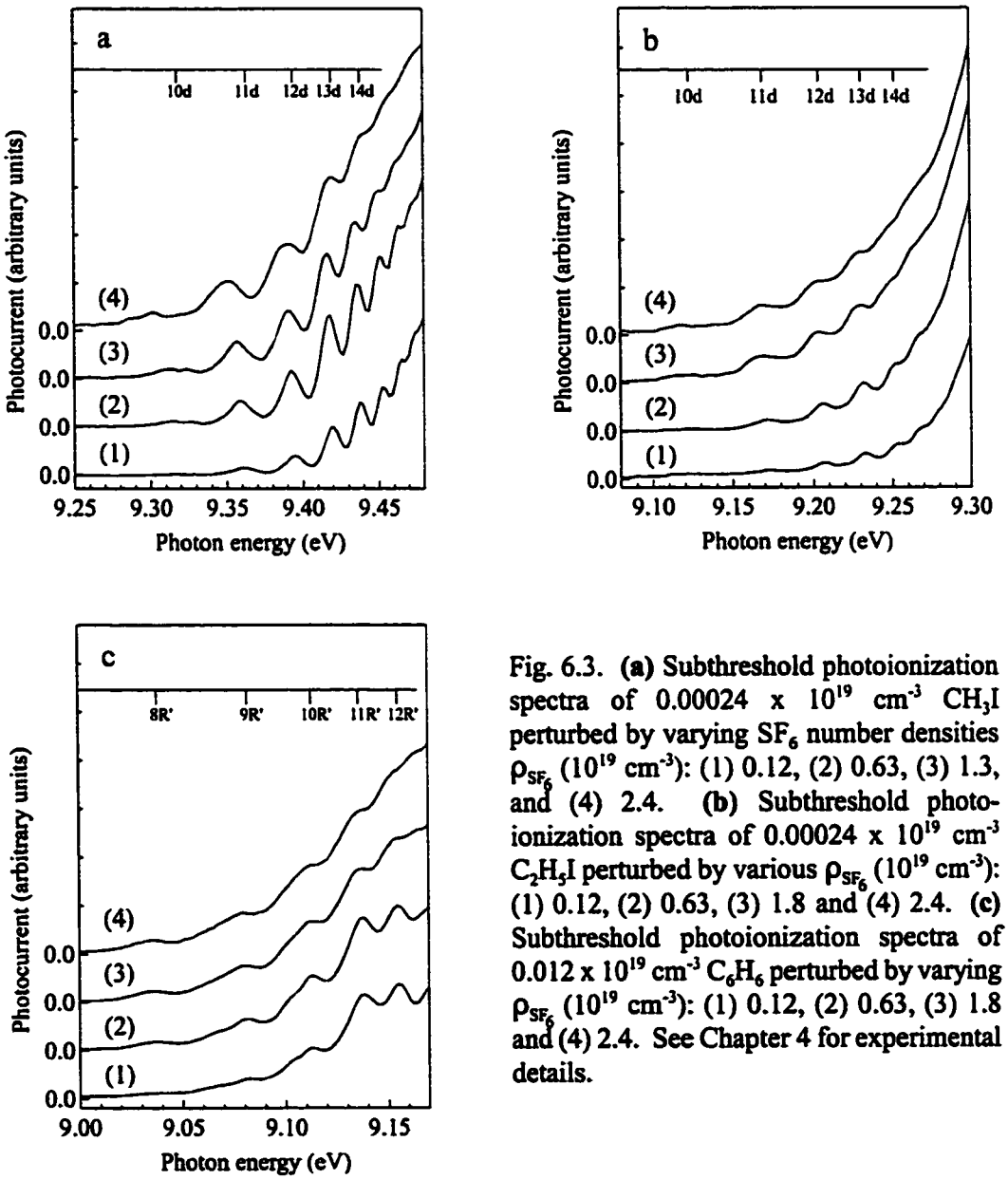

Fig. 6.3. **(a)** Subthreshold photoionization spectra of 0.00024 x 10^{19} cm^{-3} CH_3I perturbed by varying SF_6 number densities ρ_{SF_6} (10^{19} cm^{-3}): (1) 0.12, (2) 0.63, (3) 1.3, and (4) 2.4. **(b)** Subthreshold photoionization spectra of 0.00024 x 10^{19} cm^{-3} C_2H_5I perturbed by various ρ_{SF_6} (10^{19} cm^{-3}): (1) 0.12, (2) 0.63, (3) 1.8 and (4) 2.4. **(c)** Subthreshold photoionization spectra of 0.012 x 10^{19} cm^{-3} C_6H_6 perturbed by varying ρ_{SF_6} (10^{19} cm^{-3}): (1) 0.12, (2) 0.63, (3) 1.8 and (4) 2.4. See Chapter 4 for experimental details.

In Table 6.1, a summary of the scattering lengths determined from the subthreshold photoionization structure is given along with the scattering lengths determined from the absorption and autoionization structure (cf. Table 5.1). Clearly, the scattering lengths from the subthreshold structure agree, to within experimental error, with those obtained from the absorption and autoionization measurements. Therefore, the subthreshold photocurrent observed in these systems arises from the ionization of high-*n* dopant Rydberg states.

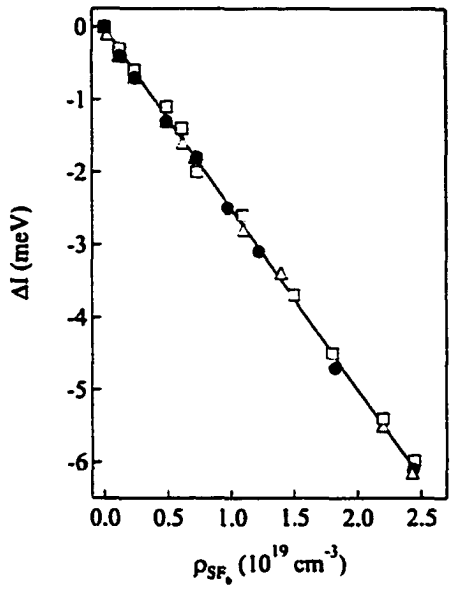

Fig. 6.4. Shift of the first ionization energies ΔI of CH_3I (●), C_2H_5I (□) and C_6H_6 (△) obtained from fitting the assigned spectra (e.g., Fig. 6.3) to the Rydberg equation, plotted vs. ρ_{SF_6}. The solid line represents a linear least-square fit to the data. (The error in the energy for each point is ± 3 meV.)

C. Temperature Studies

The study of temperature effects on subthreshold photoionization can help one to probe the processes leading to subthreshold photoionization. For instance, if subthreshold photoionization proceeds through hot-band autoionization, the relative intensities of the subthreshold peaks should vary as a function of temperature (cf. Fig. 3.6) due to a difference

Table 6.1. Comparison of the zero-kinetic-energy electron scattering lengths obtained from the shift of the subthreshold ionization (ST) structure with those obtained from the absorption and autoionization structure (cf. Table 5.1).

Perturber	A (nm) (ST)	A (nm) (Table 5.1)
CF_4	-0.173 ± 0.009	-0.180 ± 0.003
c-C_4F_8	-0.600 ± 0.025	-0.618 ± 0.012
SF_6	-0.487 ± 0.019	-0.484 ± 0.010

in the distribution of populated dopant vibrational levels. Subthreshold structure arising from this type of effect has been observed in very low number densities of CH_3I [85], as well as in other molecules [89-95]. Collisional transfer of translational, vibrational and rotational energy from the perturber to the excited state dopant are also mechanisms which are temperature dependent. In this Section, the temperature dependence of the subthreshold photoionization structure of CH_3I perturbed by Ar, CF_4, *c*-C_4F_8, CO_2, N_2 and SF_6, and of C_2H_5I and C_6H_6 perturbed by SF_6, is presented.

In Fig. 6.5a, the subthreshold photoionization spectra of 0.12×10^{19} cm^{-3} CH_3I at various temperatures are presented. The subthreshold photoionization spectra of 0.012×10^{19} cm^{-3} CH_3I perturbed by 0.49×10^{19} cm^{-3} Ar at various temperatures are shown in Fig. 6.5b.

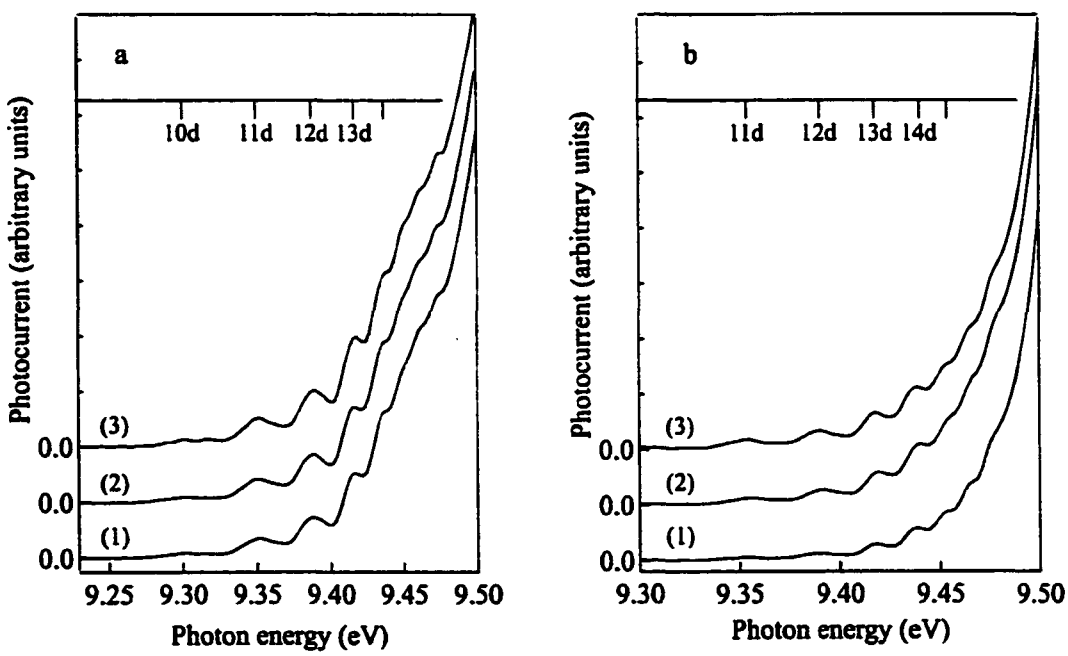

Fig. 6.5. **(a)** Temperature dependence of the subthreshold photoionization of 0.12×10^{-19} cm^{-3} of CH_3I at (1) 273 K, (2) 298 K and (3) 332 K. **(b)** Temperature dependence of the subthreshold photoionization of 0.012×10^{-19} cm^{-3} CH_3I perturbed by 0.49×10^{19} cm^{-3} Ar at (1) 233 K, (2) 398 K and (3) 348 K. Spectra were taken in Cell 2 with a resolution of ~ 10 meV (200 μm slits) in the energy region of interest. See Chapter 4 for experimental details.

(Similar spectra for CH_3I perturbed by CF_4, c-C_4F_8, CO_2, N_2 and SF_6, as well as C_2H_5I and C_6H_6 perturbed by SF_6 were also measured. Since these spectra demonstrate qualitatively similar behavior to those in Fig. 6.5, these spectra are not reproduced here.) Clearly, the observed subthreshold photoionization shows no change in the relative peak intensities indicative of hot-band autoionization (cf. Fig 3.6). Furthermore, this subthreshold structure is approximately two orders of magnitude larger than the structure shown in Fig. 3.6 and, for pure CH_3I (cf. Fig. 6.5a), has a lower onset energy.

However, the overall exponential background increases as the temperature increases. This increase in the exponential background arises from an increase in collisions between the excited-state dopant and the perturber as the temperature increases and, therefore, should be governed by a Boltzmann distribution (i.e., $e^{-\Delta E/k_B T}$). Hence, if the background of the spectra shown in Fig. 6.5 is fitted to an equation having the form $e^{-\chi \Delta E}$, where χ is a regression coefficient, it should follow that $T\,\chi$ is constant over the entire temperature range. In Table 6.2, the regression coefficients χ of the CH_3I/Ar spectra presented in Fig. 6.5a are given along with the values for $T\,\chi$. Since $T\,\chi$ is constant (to within experimental error) for all of the temperatures measured, one may conclude that the temperature-induced change in the exponential background is caused by an increasing collisional ionization as temperature

Table 6.2. The regression coefficients χ from the exponential least-square fit to the background of CH_3I/Ar (cf. Fig. 6.5a) as a function of temperature (K).

Temperature (K)	χ (arbitrary units)	$T\,\chi$ (arbitrary units)
233	0.313	72.9
298	0.245	73.0
348	0.210	73.0

increases. (Similar results for CH_3I were obtained for each perturber. These data are given in Appendix 2.A.)

If the background increase arises solely from the collisional transfer of translation energy, different perturbers should give rise to similar exponential backgrounds. However, an increase in the perturber number density should increase the exponential background due to the increased probability of a collision. In Fig. 6.6, the area of the exponential background of subthreshold photoionization of CH_3I/P (P = Ar, CF_4, *c*-C_4F_8, CO_2, N_2 and SF_6) is plotted as a function of perturber number density ρ_P. Fig. 6.6 shows that the exponential background is linearly dependent on the perturber number density but is independent of the type of perturber, thereby confirming that collisional transfer of translational energy is the cause of the rising exponential background. (The areas obtained from the least-square exponential fit to the background of the subthreshold photoionization spectra of CH_3I doped into each of the perturbers are given in Appendix 2.B.)

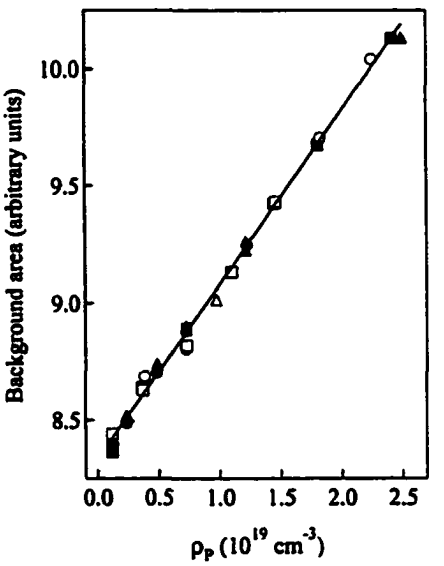

Fig. 6.6. The area of the least-square fits to the exponential background of CH_3I perturbed by Ar (●), CF_4 (○), *c*-C_4F_8 (■), CO_2 (□), N_2 (▲) and SF_6 (△) plotted vs. the perturber number density ρ_P.

Finally, the collisional transfer of rotational or vibrational energy from the perturber to the excited state dopant can be further excluded as a possible mechanism leading to the observed subthreshold photoionization structure (i.e., Figs. 6.1a, 6.2a, 6.3, 6.5) because of

the similarity of this structure as the perturber changes from an atomic perturber (cf. 6.5b) to a molecular perturber (cf. 6.1a).

In Section E, the variation in the peak areas of the subthreshold photoionization structure as a function of dopant and perturber number density is presented. Since the area under the exponential background changes as a function of perturber number density, the subthreshold peak areas were also evaluated after the exponential background was removed. The peak areas which result from a gaussian deconvolution of the background-corrected spectra exhibit no qualitative difference from those peak areas obtained prior to the removal of the exponential background. Therefore, the peak areas presented in Section E are not corrected for the exponential background.

D. Photochemical Rearrangement

In some instances, photochemical rearrangement leading to charged products has been invoked to explain the appearance of subthreshold photoionization [87,88]. As will be shown below, for the dopants in this study photochemical rearrangement is not feasible energetically.

The most common photochemical rearrangement of CH_3I is [6,87,88]

$$CH_3I + h\nu \rightarrow CH_3I^* \rightarrow CH_3^+ + I^-,$$

which has an appearance potential of 12.07 ± 0.07 eV [147]. This threshold is far above the first ionization potential and, therefore, cannot be the process generating subthreshold photoionization. The other known photochemical reactions in CH_3I which generate ionic products also occur at energies above the first ionization threshold [148-150]. Thus, photochemical rearrangement of CH_3I can be ruled out as a potential subthreshold photoionization mechanism.

C_2H_5I can also photodissociate via a similar process, namely

$$C_2H_5I + h\nu \rightarrow C_2H_5I^* \rightarrow C_2H_5^+ + I^- .$$

which has an appearance potential of 10.44 eV [151,152]. Again this value is far above the first ionization threshold of C_2H_5I and, thus, cannot account for the observation of subthreshold photoionization in C_2H_5I/SF_6. Furthermore, the lack of subthreshold photoionization in pure C_2H_5I [14,20] is also indicative of a absence of photochemical rearrangement. Similarly, the lack of subthreshold photoionization in pure C_6H_6 [14,20] indicates an absence of photochemical rearrangements of C_6H_6 at these energies.

E. Density Studies [14,17-20]

In the previous three Sections, the subthreshold photoionization structure in CH_3I/P (P = Ar, CF_4, *c*-C_4F_8, CO_2, N_2, SF_6), C_2H_5I/SF_6 and C_6H_6/SF_6 has been shown to arise from high-*n* Rydberg states of the dopant. This subthreshold structure does not have the temperature dependence indicative of hot-band or rotational autoionization (cf. Section C), and photochemical rearrangement that generates charged particles was ruled out on the basis of energetics (cf. Section D). Once these traditional mechanisms have been dismissed, two other mechanisms leading to subthreshold photoionization, namely electron attachment and associative ionization, must be considered.

In this work, two pathways involving these processes are proposed for the explanation of subthreshold structure. The first pathway requires direct dopant/perturber interactions leading both to charge transfer and to heteromolecular dimer ion formation:

$$D^* + P \rightarrow D^+ + P^- \qquad (6.1)$$

$$D^* + P \rightarrow DP^+ + e^-, \qquad (6.2)$$

where D^* is a Rydberg state of the dopant molecule. Since the first process (i.e., Eq. (6.1))

of this pathway invokes electron attachment to the perturber, this mechanism should be enhanced in perturbers exhibiting a large electron attachment cross-section (e.g., *c*-C_4F_8 and SF_6). The second process (i.e., Eq. (6.2)) constitutes associative ionization, which should lead to a perturber-dependent onset energy as a result of dopant/perturber dimerization.

The second pathway, namely

$$D^* + D \longrightarrow D^+ + D^- \tag{6.3}$$

$$D^* + D \longrightarrow D_2^+ + e^- \tag{6.4}$$

$$D^* + D + P \longrightarrow D_2^+ + P + e^-, \tag{6.5}$$

differs significantly with regard to the dopant/perturber interactions. In the first process (i.e., Eq. (6.3)), electron attachment is now to the dopant rather than to the perturber. Therefore, if the dopant itself has a large electron attachment cross-section, subthreshold structure should be observed even when the perturber has a low electron attachment cross-section (e.g., Ar, N_2, CO_2 and CF_4). The second process (i.e., Eq. (6.4)) invokes associative ionization that is independent of the perturber, while the third process (i.e., Eq. (6.5)) constitutes associative ionization that is only stabilized by the perturber [104]. Therefore, the onset energy should remain constant even if the perturber is varied. Finally, for the case of a pure dopant that exhibits subthreshold photoionization structure (e.g., CH_3I [17,20,87,88]), pathway 2 reduces to Eqs. (6.3) and (6.4).

For either of the above pathways, the subthreshold photocurrent will be given by a sum of two contributions, namely

$$i = i_{ea} + i_{ai}, \tag{6.6}$$

where i_{ea} is the photocurrent contribution resulting from electron attachment, and i_{ai} is that resulting from associative ionization. If one now assumes that the electron attachment is

saturated (i.e., dependent only on the excited state number density ρ_{D^*}), and if one further assumes that $\rho_{D^*} \propto \rho_D$ in the linear absorption regime, the electron attachment contribution to the photocurrent for both pathways 1 and 2 reduces to

$$i_{ea} = k_{ea}^{(1,2)} \rho_D \,, \tag{6.7}$$

where $k_{ea}^{(1,2)}$ is the effective rate constant for saturated electron attachment in the two pathways (i.e., Eqs. (6.1) and (6.3)).

Pathways 1 and 2 differ with regard to the associative ionization contribution to the subthreshold photocurrent, however. If one again assumes that $\rho_{D^*} \propto \rho_D$ in the linear absorption regime, the associative ionization contribution from pathway 1 is given by

$$i_{ai} = k_{ai}^{(1)} \rho_D \rho_P \,, \tag{6.8}$$

while the same contribution from pathway 2 is given by

$$i_{ai} = k_{ai}^{(2)} \rho_D^2 + k_{ai}^{\prime(2)} \rho_D^2 \rho_P \,, \tag{6.9}$$

where the associative ionization effective rate constants $k_{ai}^{(1)}$, $k_{ai}^{(2)}$ and $k_{ai}^{\prime(2)}$ refer to Eqs. (6.2), (6.4) and (6.5), respectively.

By combining Eqs. (6.7) - (6.9), one finds that the total subthreshold photocurrent is

$$i = k_{ea}^{(1)} \rho_D + k_{ai}^{(1)} \rho_D \rho_P \,, \tag{6.10}$$

for pathway 1, and

$$i = k_{ea}^{(2)} \rho_D + k_{ai}^{(2)} \rho_D^2 + k_{ai}^{\prime(2)} \rho_D^2 \rho_P \,, \tag{6.11}$$

for pathway 2. Clearly, when a dopant/perturber system exhibits subthreshold photoionization, both pathways 1 and 2 may be operative simultaneously. However, in a system where both pathways are available, pathway 1 should dominate when $\rho_P \gg \rho_D$. Therefore, if the perturber has a large electron attachment cross-section and $\rho_P \gg \rho_D$, one should expect that the subthreshold photocurrent will be modeled by Eq. (6.10), with little

contribution from pathway 2. However, as ρ_D increases, contributions from pathway 2 will begin to appear and the total contribution to the photocurrent will be given by a sum of Eq. (6.10) and (6.11), or

$$i = \left(k'^{(2)}_{ai}\ \rho_D^2 + k^{(1)}_{ai}\ \rho_D\right)\rho_P + \left(k^{(2)}_{ai}\ \rho_D^2 + (k^{(1)}_{ea} + k^{(2)}_{ea})\ \rho_D\right). \qquad (6.12)$$

As will be shown below, the subthreshold photocurrent of dopant/perturber systems which can access both pathways 1 and 2 requires the use of Eq. (6.12) to accurately model the density dependence of the subthreshold structure over the entire density range.

If the perturber has a small electron attachment cross-section, on the other hand, one should expect that the subthreshold photocurrent will be modeled by Eq. (6.11), with little contribution from pathway 1. However, the accessibility of pathway 2 depends upon the nature of dopant/dopant interactions. If electron attachment to the dopant and homomolecular dopant dimerization are not favored, subthreshold photocurrent generated via pathway 2 is unlikely.

In what follows, a systematic density study of the subthreshold photoionization of CH_3I, C_2H_5I and C_6H_6 perturbed by Ar, CF_4, *c*-C_4F_8, CO_2, N_2 and SF_6 is presented. The perturbers Ar, CF_4, CO_2 and N_2 were selected because of their small electron affinities, which make these perturbers prime candidates for investigating pathway 2. The perturbers *c*-C_4F_8 and SF_6, on the other hand, were selected because of their large electron affinities, which make these perturbers ideal for investigating pathway 1. By varying the dopant number density ρ_D and the perturber number density ρ_P simultaneously, the pathway leading to subthreshold photoionization will be determined for each dopant/perturber system. The density dependent variation of the subthreshold structure will then be used to determine the effective rate constants for electron attachment and associative ionization. Finally, the effect of the

electron affinity (of the dopant or perturber) on the electron attachment rate constant $k_{ea}^{(1,2)}$ will be discussed, and the effect of the ground-state polarizability (of the dopant or perturber) on the associative ionization rate constants $k_{ai}^{(1,2)}$ and $k_{ai}^{\prime(2)}$ will be presented.

i. C_2H_5I [14,20]

In this Section, subthreshold photoionization results for pure C_2H_5I and C_2H_5I perturbed by Ar, CF_4, *c*-C_4F_8, CO_2, N_2 and SF_6 are reported for variations in both $\rho_{C_2H_5I}$ and ρ_P. For brevity, however, only representative subthreshold photoionization spectra are presented. From the density dependence of the subthreshold structure as a function of $\rho_{C_2H_5I}$ and ρ_P, a determination is made as to which pathway best models the observed subthreshold photocurrent. The density dependent variation of the subthreshold structure is then used to determine the effective rate constants for electron attachment and associative ionization in these systems.

a. Results

No subthreshold photoionization structure was observed in the subthreshold photoionization spectra of pure C_2H_5I and of C_2H_5I perturbed by Ar, CF_4, CO_2 and N_2, thereby indicating that pathway 2 is inaccessible for this dopant. However, C_2H_5I exhibits weak subthreshold photoionization structure when doped into *c*-C_4F_8 (cf. Fig. 6.7) and rich subthreshold photoionization structure when doped into SF_6 (cf. Figs. 6.8a and 6.8a′). (The C_2H_5I/*c*-C_4F_8 subthreshold photoionization structure is too weak to analyze. Therefore, a complete study of the density dependence of this structure was not attempted.) Figs. 6.8a and 6.8a′ present representative subthreshold photoionization spectra of C_2H_5I/SF_6 at constant SF_6 number density ρ_{SF_6} and constant C_2H_5I number density $\rho_{C_2H_5I}$, respectively, and the peak areas obtained from these spectra are plotted versus $\rho_{C_2H_5I}$ and ρ_{SF_6} in Figs. 6.8b and 6.8b′,

respectively. The linearity of the subthreshold photoionization intensity as a function of $\rho_{C_2H_5I}$ and ρ_{SF_6} indicates that the subthreshold photocurrent can be modeled by Eq. (6.10). Thus, these measurements show that the subthreshold photocurrent observed in C_2H_5I/SF_6 arises from pathway 1, with no contribution from pathway 2.

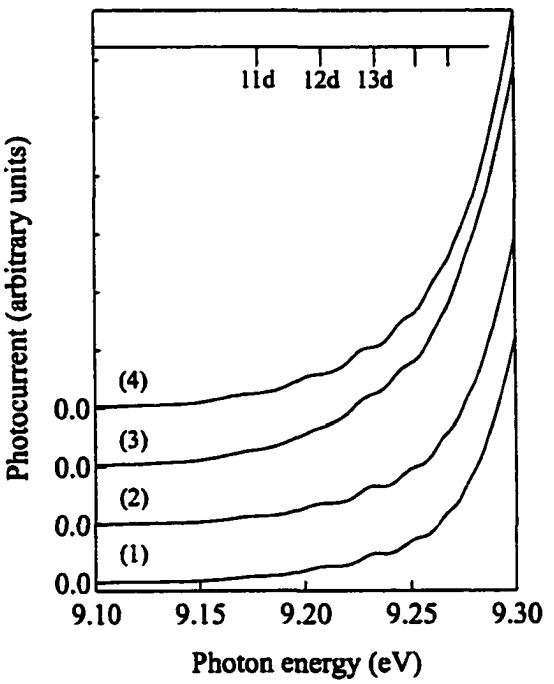

Fig. 6.7. Subthreshold photoionization spectra of 0.012 x 10^{19} cm^{-3} C_2H_5I in varying c-C_4F_8 number densities $\rho_{c\text{-}C_4F_8}$ (10^{19} cm^{-3}): (1) 0.36, (2) 0.73, (3) 1.4, and (4) 1.8.

b. Discussion

The determination of the effective rate constants for electron attachment and associative ionization requires a variation in both $\rho_{C_2H_5I}$ and ρ_{SF_6}. The evaluation of these constants begins by studying the density dependence of the subthreshold photocurrent when ρ_{SF_6} is varied at different constant values of $\rho_{C_2H_5I}$. For constant $\rho_{C_2H_5I}$, the total subthreshold photocurrent for pathway 1 (i.e., Eq. (6.10)), becomes

$$i = b_0 + b_1 \rho_P , \tag{6.13}$$

where P = SF_6, with the coefficients b_0 and b_1 being defined by

$$b_0 = k_{ea}^{(1)} \rho_D , \quad b_1 = k_{ai}^{(1)} \rho_D , \tag{6.14}$$

where D = C_2H_5I. Therefore, if b_0 and b_1 are obtained for various values of $\rho_{C_2H_5I}$, and if b_0 and b_1 are linear functions of $\rho_{C_2H_5I}$, then pathway 1 has been substantiated and the effective rate constants $k_{ea}^{(1)}$ and $k_{ai}^{(1)}$ can be obtained from Eq. (6.14). In Table 6.3, the values for b_0 and

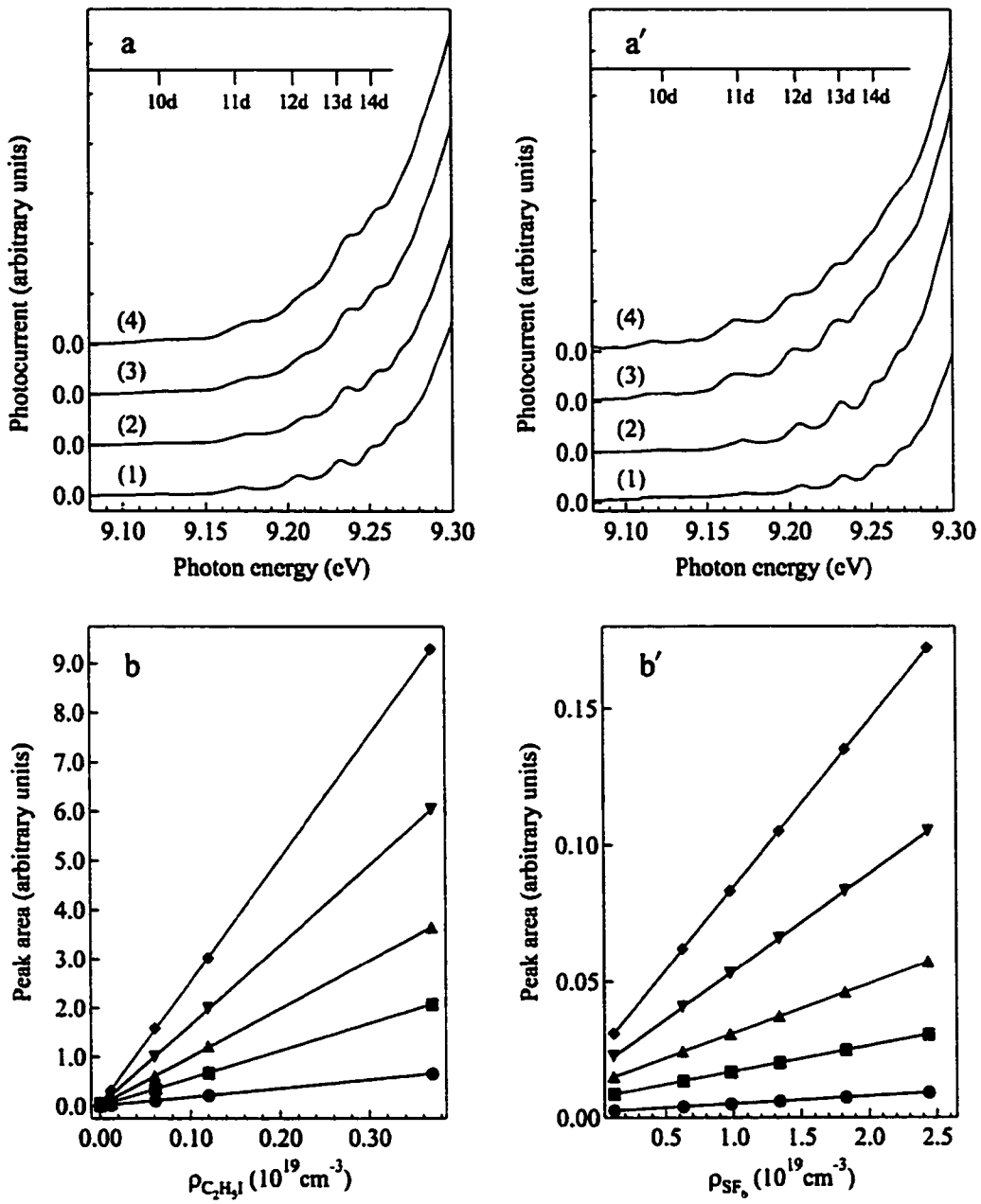

Fig. 6.8. Subthreshold photoionization spectra of C_2H_5I/SF_6: (a) photoionization of varying C_2H_5I number densities $\rho_{C_2H_5I}$ (10^{19} cm^{-3}) perturbed by 0.63×10^{19} cm^{-3} SF_6. (1) 0.00024, (2) 0.012, (3) 0.12 and (4) 0.37. (a′) Photoionization of 0.00024×10^{19} cm^{-3} C_2H_5I perturbed by varying SF_6 number densities ρ_{SF_6} (10^{19}cm^{-3}): (1) 0.12, (2) 0.63, (3) 1.8 and (4) 2.4. (b) Peak areas for the subthreshold structure shown in (a) plotted vs. $\rho_{C_2H_5I}$. (b′) Peak areas for the subthreshold structure shown in (a′) plotted vs. ρ_{SF_6}. In (b) and (b′): (●) 10d, (■) 11d, (▲) 12d, (▼) 13d, and (◆) 14d. The solid lines represent a linear least-square fits to Eq. (6.10). See Chapter 4 for experimental details.

b_1, obtained as described above, for various values of $\rho_{C_2H_5I}$ are given. (The peak areas used to evaluate b_0 and b_1 are given in Appendix 3.A.) These values are also plotted as functions of $\rho_{C_2H_5I}$ in Fig. 6.9. Clearly, b_0 and b_1 are linearly dependent upon $\rho_{C_2H_5I}$ and, therefore, Eq. (6.14) can be employed. The effective rate constants $k_{ea}^{(1)}$ and $k_{ai}^{(1)}$ obtained from a least-square linear regression of b_0 and b_1 are also given in Table 6.3.

Table 6.3. (a) The constant regression coefficient b_0 and (b) the linear regression coefficient b_1 determined from a pressure study of the subthreshold photoionization structure of C_2H_5I/SF_6 as a function of $\rho_{C_2H_5I}$ (10^{19} cm^{-3}).

a. b_0

$\rho_{C_2H_5I}$	10d	11d	12d	13d	14d
0.00024	0.0022	0.0053	0.011	0.018	0.023
0.012	0.011	0.037	0.064	0.091	0.12
0.061	0.056	0.19	0.32	0.46	0.60
0.12	0.11	0.37	0.63	0.91	1.2
0.37	0.34	1.2	2.0	2.8	
Effective rate constant (arbitrary units) [a]					
$k_{ea}^{(1)}$	1.0	3.1	5.1	7.3	9.4

b. b_1

$\rho_{C_2H_5I}$	10d	11d	12d	13d	14d
0.00024	0.0072	0.0010	0.017	0.026	0.041
0.012	0.014	0.047	0.091	0.18	0.30
0.061	0.073	0.24	0.46	0.92	1.6
0.12	0.14	0.45	0.91	1.7	3.0
0.37	0.44	1.4	2.8	5.5	
Effective rate constant (arbitrary units) [a]					
$k_{ai}^{(1)}$	1.2	3.9	7.6	15	25

[a]The effective rate constants $k_{ea}^{(1)}$ and $k_{ai}^{(1)}$ were determined by least-square linear fits to Eq. (6.14), as shown in Fig. 6.9.

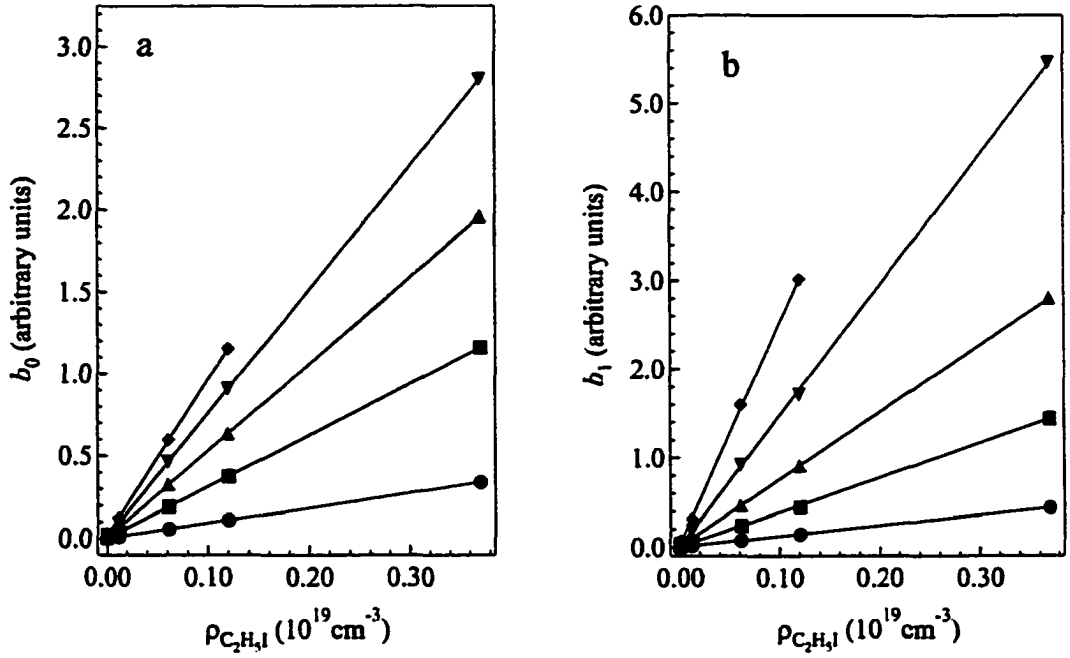

Fig. 6.9. (a) Constant and (b) linear regression coefficients for the subthreshold density dependence of C_2H_5I/SF_6 plotted vs. $\rho_{C_2H_5I}$. (●) 10d, (■) 11d, (▲) 12d, (▼) 13d, and (◆) 14d. The solid lines represent linear least-square fits to Eq. (6.14) (cf. Table 2). See text for discussion.

As discussed in Chapter 3.C.iii, the electron attachment cross-section scales as the principal quantum number n of the dopant Rydberg state. Since the electron attachment rate constant $k_{ea}^{(1)}$ is proportional to the electron attachment cross-section, $k_{ea}^{(1)}$ should also be linearly dependent on n. The associative ionization rate constant $k_{ai}^{(1)}$, on the other hand, should be proportional to n^7 (cf. Chapter 3.C.iv). That this is indeed the case is shown in Figs. 6.10a and 6.10b, respectively. The n dependence of these rate constants, when coupled with the analysis presented above, allows one to conclude that pathway 1 is sufficient to explain the behavior of the subthreshold photocurrent in C_2H_5I/SF_6.

ii. C_6H_6 [14,20]

In this Section, subthreshold photoionization results are reported for pure C_6H_6 and for C_6H_6 perturbed by Ar, CF_4, c-C_4F_8, CO_2, N_2 and SF_6. For the sake of brevity, only

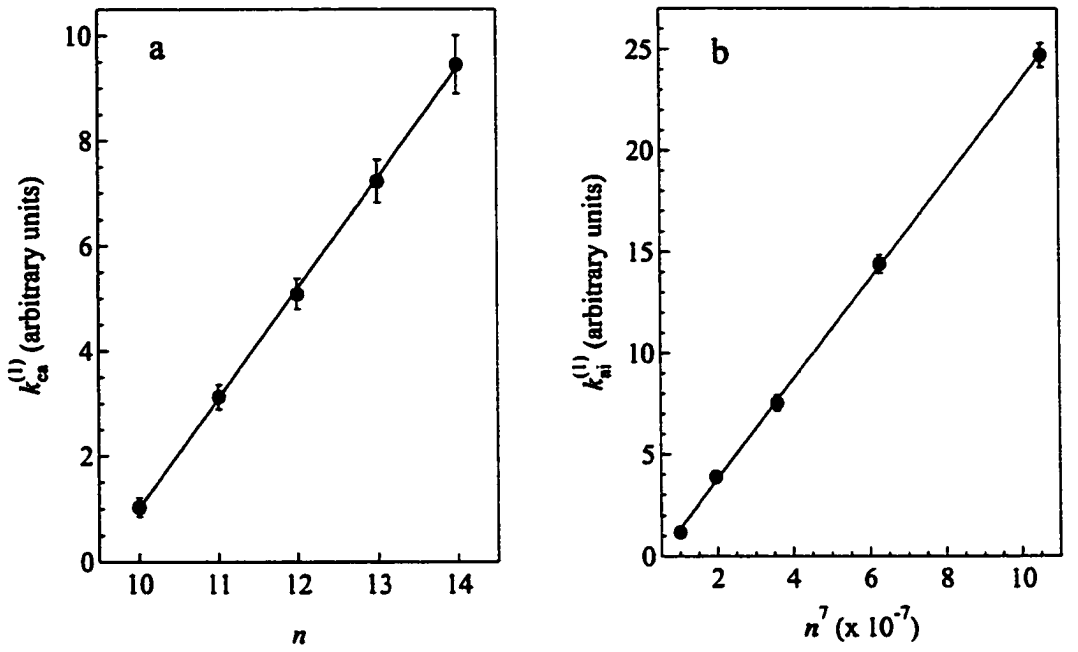

Fig. 6.10. (a) Effective rate constant $k_{ea}^{(1)}$ for the electron attachment mechanisms (i.e., Eq. (6.1)) in C_2H_5I/SF_6 (cf. Table 6.3) plotted vs. the excited-state principal quantum number n of C_2H_5I. (b) Effective rate constant $k_{ai}^{(1)}$ for the associative ionization mechanism (i.e., Eq. (6.2)) in C_2H_5I/SF_6 (cf. Table 6.3) plotted vs. n^7 of C_2H_5I. The solid lines are linear least-square fits to the data. The error bars for $k_{ea}^{(1)}$ and $k_{ai}^{(1)}$ result from the assumption of a variance of ± 1 standard deviation both in the fitting of the subthreshold peaks and in the regression analysis used to obtain these rate constants. See text for discussion.

representative subthreshold photoionization spectra are presented, however. Using procedures similar to the ones given above for C_2H_5I, the dopant and perturber number density dependence of the subthreshold photoionization structure are used to determine which pathway best models the observed subthreshold structure. The effective rate constants for electron attachment and associative ionization in these systems are then evaluated from the density dependent variation of the subthreshold structure.

a. Results

Subthreshold photoionization structure is not observed in the subthreshold spectra of pure C_6H_6 and in those of C_6H_6 perturbed by Ar, CF_4, CO_2 and N_2, which is analogous to the

behavior observed for the dopant C_2H_5I. Therefore, subthreshold photoionization in C_6H_6 cannot proceed through pathway 2. C_6H_6 perturbed by *c*-C_4F_8 possesses weak subthreshold photoionization structure (cf. Fig. 6.11), and C_6H_6 perturbed by SF_6 exhibits strong subthreshold photoionization structure (cf. Figs. 6.12a and 6.12a′). (The weakness of the C_6H_6/*c*-C_4F_8 subthreshold structure precludes a complete study of the density dependence of this structure.)

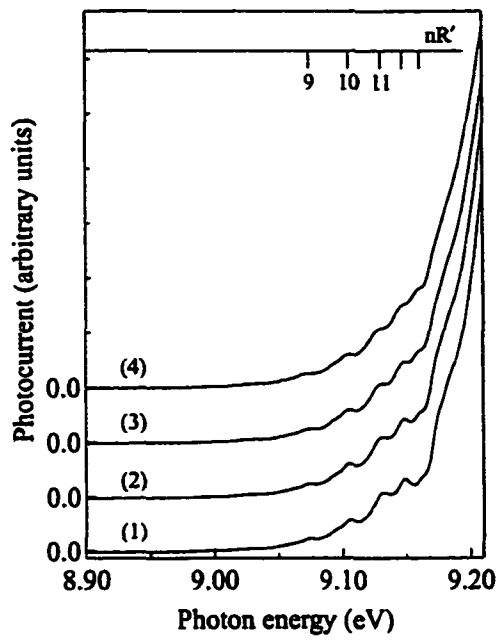

Fig. 6.11. Subthreshold photoionization spectra of 0.061 x 10^{19} cm^{-3} C_6H_6 perturbed by varying *c*-C_4F_8 number densities $\rho_{c\text{-}C_4F_8}$ (10^{19} cm^{-3}): (1) 0.65, (2) 0.97, (3) 1.3, and (4) 1.8. See Chapter 4 for experimental details.

Figs. 6.12a and 6.12a′ present subthreshold photoionization spectra of C_6H_6/SF_6 at constant ρ_{SF_6} and constant $\rho_{C_6H_6}$, respectively, and the peak areas obtained from these spectra are plotted versus $\rho_{C_6H_6}$ and ρ_{SF_6} in Figs. 6.12b and 6.12b′, respectively. The linearity of the subthreshold photoionization intensity as a function of $\rho_{C_6H_6}$ and ρ_{SF_6} in this system indicates that, similar to the case of C_2H_5I, the subthreshold photocurrent can be modeled exclusively by Eq. (6.10). Thus, these measurements show that the subthreshold photocurrent observed in C_6H_6/SF_6 arises from pathway 1, with no contribution from pathway 2.

b. Discussion

Since C_6H_6/SF_6 behaves like C_2H_5I/SF_6, the effective rate constants are evaluated in the manner described in Section E.i.b. Again, the effective rate constants are determined by

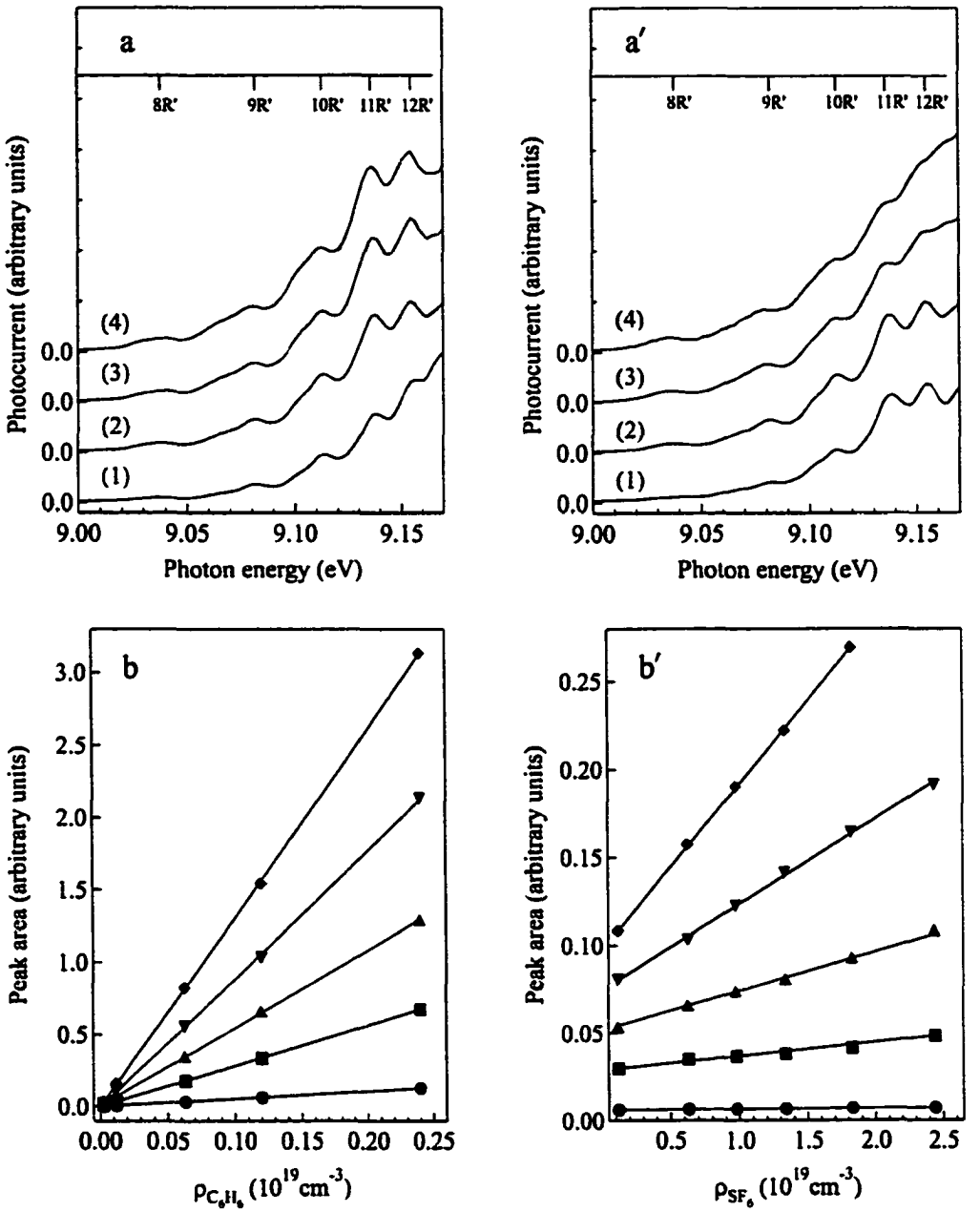

Fig. 6.12. Subthreshold photoionization spectra of C_6H_6/SF_6: **(a)** photoionization of varying C_6H_6 number densities $\rho_{C_6H_6}$ (10^{19} cm^{-3}) perturbed by 0.63 × 10^{19} cm^{-3} SF_6. (1) 0.0024, (2) 0.012, (3) 0.12 and (4) 0.24. **(a′)** Photoionization of 0.012 × 10^{19} cm^{-3} C_6H_6 perturbed by varying SF_6 number densities ρ_{SF_6} ($10^{19}cm^{-3}$): (1) 0.12, (2) 0.63, (3) 1.8 and (4) 2.4. **(b)** Peak areas for the subthreshold structure shown in **(a)** plotted vs. $\rho_{C_6H_6}$. **(b′)** Peak areas for the subthreshold structure shown in **(a′)** plotted vs. ρ_{SF_6}. In **(b)** and **(b′)**: (●) 8R', (■) 9R', (▲) 10R', (▼) 11R', and (◆) 12R'. The solid lines represent a linear least-square fits to Eq. (6.10). See Chapter 4 for experimental details.

ρ_{SF_6} at different constant values of $\rho_{C_6H_6}$, thereby confirming that Eqs. (6.13) and (6.14) continue to be the correct model equations. In Table 6.4, the values for b_0 and b_1, obtained as described above, for various values of $\rho_{C_6H_6}$ are given. (The peak areas used to evaluate b_0 and b_1 are given in Appendix 3.B.) These values are also plotted as functions of $\rho_{C_6H_6}$ in Fig. 6.13. Again b_0 and b_1 are linearly dependent on $\rho_{C_6H_6}$ and, therefore can be modeled

Table 6.4. (a) The constant regression coefficient b_0 and (b) the linear regression coefficient b_1 obtained from a pressure study of the subthreshold photoionization structure of C_6H_6/SF_6 as a function of $\rho_{C_6H_6}$ (10^{19} cm^{-3}).

a. b_0

$\rho_{C_6H_6}$	8R'	9R'	10R'	11R'	12R'
0.0024	0.0012	0.0058	0.010	0.015	0.019
0.012	0.0060	0.029	0.051	0.074	0.097
0.063	0.032	0.15	0.26	0.39	0.51
0.12	0.061	0.29	0.51	0.74	0.97
0.24	0.12	0.57	1.1	1.4	2.0
Effective rate constant (arbitrary units) [a]					
$k_{ea}^{(1)}$	0.50	2.4	4.3	6.2	8.1

b. b_1

$\rho_{C_6H_6}$	8R'	9R'	10R'	11R'	12R'
0.0024	0.00021	0.0041	0.0076	0.012	0.024
0.012	0.00047	0.0079	0.022	0.049	0.094
0.063	0.0025	0.041	0.12	0.25	0.49
0.12	0.0047	0.079	0.23	0.48	0.94
0.24	0.0094	0.16	0.44	0.98	1.8
Effective rate constant (arbitrary units) [a]					
$k_{ai}^{(1)}$	0.038	0.67	1.9	4.1	7.8

[a]The effective rate constants $k_{ea}^{(1)}$ and $k_{ai}^{(1)}$ are for least-square linear fits to Eq. (6.14).

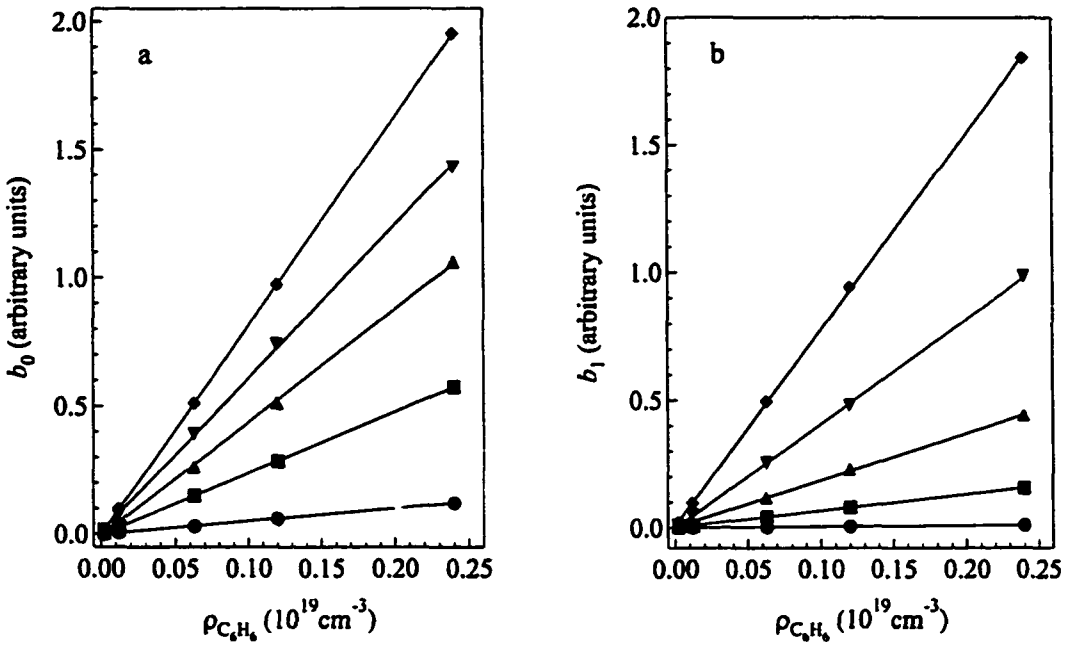

Fig. 6.13. (a) Constant and (b) linear regression coefficients for the subthreshold density dependence of C_6H_6/SF_6 plotted vs. $\rho_{C_6H_6}$. (●) 8R', (■) 9R', (▲) 10R', (▼) 11R', and (◆) 12R'. The solid lines represent linear least-square fits to Eq. (6.14) (cf. Table 6.4). See text for discussion.

using Eq. (6.14). The effective rate constants $k_{ea}^{(1)}$ and $k_{ai}^{(1)}$ obtained from a least-square linear regression of b_0 and b_1 are also given in Table 6.4.

As before, the electron attachment effective rate constant $k_{ea}^{(1)}$ and the associative ionization effective rate constant $k_{ai}^{(1)}$ should scale as n and n^7, respectively. In Fig. 6.14, this n dependence is shown to hold for C_6H_6/SF_6 and, when coupled with the analysis given above, implies that pathway 1 is sufficient to explain the behavior of subthreshold photoionization in this dopant/perturber system.

iii. CH_3I [17-20]

Subthreshold photoionization results for pure CH_3I and for CH_3I/P (P = Ar, CF_4, c-C_4F_8, CO_2, N_2 and SF_6) are presented in this Section for variations in ρ_{CH_3I} and ρ_P. For the sake of brevity, however, only representative subthreshold photoionization spectra are presented for

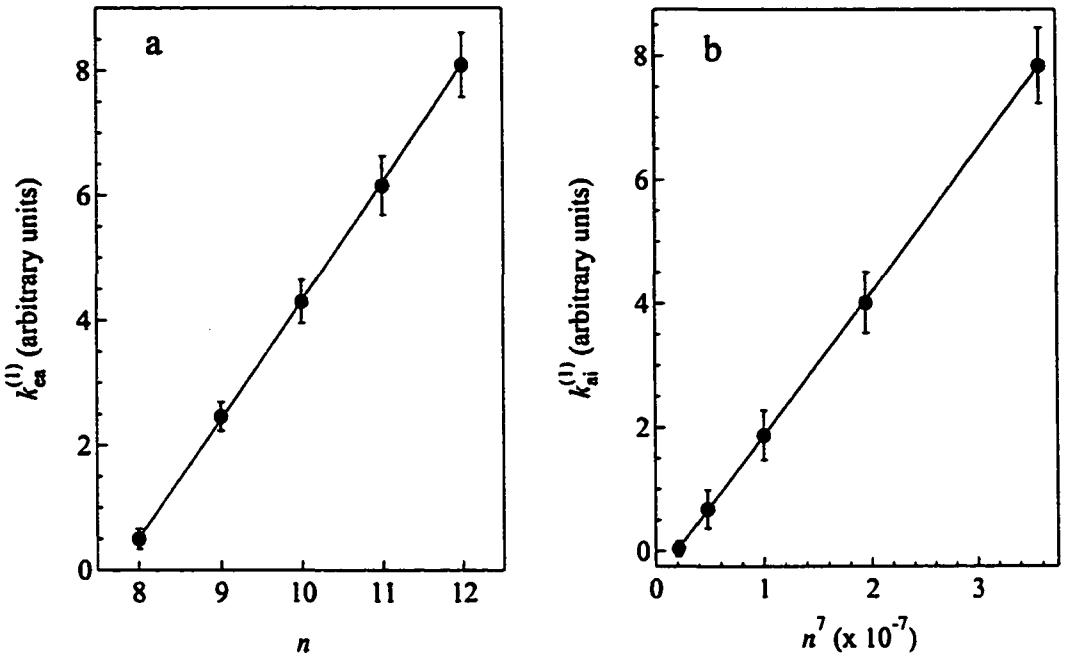

Fig. 6.14. (a) Effective rate constant $k_{ea}^{(1)}$ for the electron attachment mechanisms (i.e., Eq. (6.1)) in C_6H_6/SF_6 (cf. Table 6.4) plotted vs. the excited-state principal quantum number n of C_6H_6. (b) Effective rate constant $k_{ai}^{(1)}$ for the associative ionization mechanism (i.e., Eq. (6.2)) in C_6H_6/SF_6 (cf. Table 6.4) plotted vs. n^7 of C_6H_6. The solid lines are linear least-square fits to the data. The error bars for $k_{ea}^{(1)}$ and $k_{ai}^{(1)}$ result from the assumption of a variance of ± 1 standard deviation both in the fitting of the subthreshold peaks and in the regression analysis used to obtain these rate constants. See text for discussion.

each system. As in the cases of C_2H_5I and C_6H_6, the density dependence of the subthreshold structure as a function of ρ_{CH_3I} and ρ_P is used to determine which pathways best model the observed subthreshold photocurrent. The density dependent variation of the subthreshold structure is then used to determine the effective rate constants for electron attachment and associative ionization in these systems. The electron attachment rate constant $k_{ea}^{(1,2)}$ is shown to be linearly dependent on the electron affinity (of CH_3I or the perturber), whereas the associative ionization rate constants $k_{ai}^{(1,2)}$ and $k_{ai}^{\prime(2)}$ are shown to depend on the ground-state polarizability (of CH_3I or the perturber).

a. Results

Unlike C_2H_5I and C_6H_6, pure CH_3I is known to exhibit subthreshold photoionization structure which is quadratically dependent on ρ_{CH_3I} [17,20,87,88]. This subthreshold structure, which is shown in Fig. 6.15a, can be modeled through pathway 2 (in the absence of P). The peak areas from this structure, which are given in Table 6.5 and plotted versus ρ_{CH_3I} in Fig. 6.15b, can be analyzed with a least-square second-order polynomial regression on Eq. (6.11). This nonlinear regression leads directly to the electron attachment rate constant $k_{ea}^{(2)}$ and to the associative ionization rate constant $k_{ai}^{(2)}$ for each discrete CH_3I Rydberg state observed (n = 10 - 14), and the values for these rate constants are also given in Table 6.5.

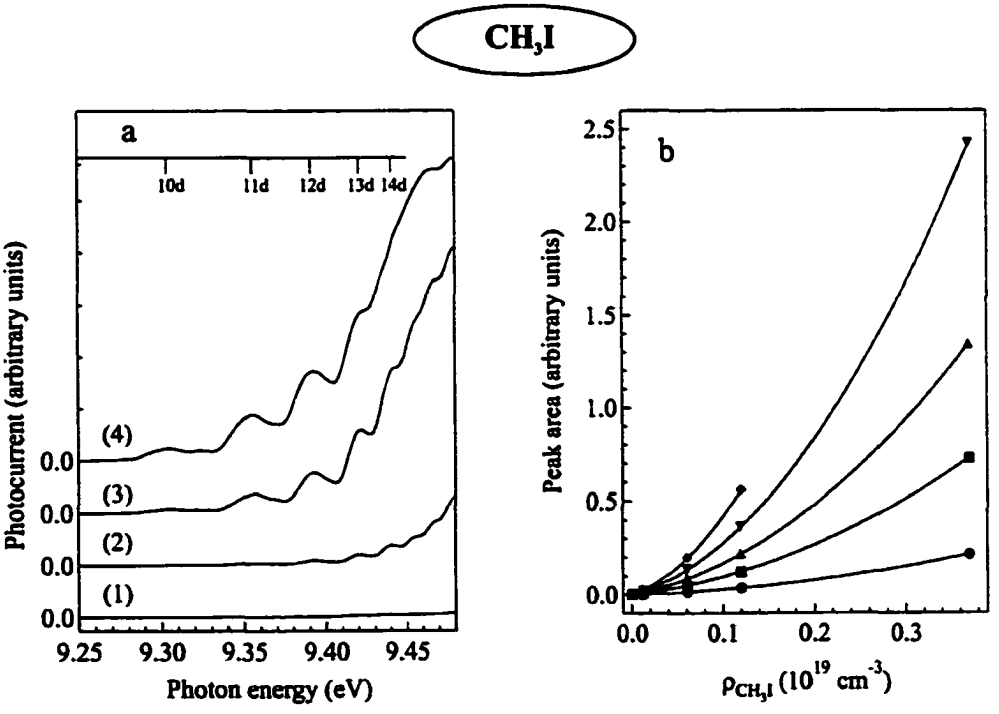

Fig. 6.15. Subthreshold photoionization spectra of CH_3I: **(a)** photoionization spectra of varying CH_3I number densities ρ_{CH_3I} ($10^{19}cm^{-3}$): (1) 0.00024, (2) 0.012, (3) 0.12, and (4) 0.37. **(b)** Peak areas for the subthreshold photoionization structure in **(a)** plotted vs. ρ_{CH_3I}. (●) 10d, (■) 11d, (▲) 12d, (▼) 13d, and (◆) 14d. The solid lines represent least-square second-order polynomial fits to Eq. (6.11) (cf. Table 6.5). See text for discussion. See Chapter 4 for experimental details.

Table 6.5. Peak areas (by gaussian fits to the photoionization spectra) for the subthreshold photoionization structure (cf. Fig. 6.15) of pure CH_3I at varying number densities ρ_{CH_3I} (10^{19} cm^{-3}).

ρ_{CH_3I}	10d	11d	12d	13d	14d
0.00024	0.00	0.00	0.00	0.00	0.00
0.025	0.00	0.0074	0.012	0.018	0.024
0.061	0.014	0.049	0.084	0.13	0.20
0.12	0.035	0.12	0.22	0.36	0.56
0.37	0.21	0.73	1.3	2.4	
Effective rate constants (arbitrary units)[a]					
$k_{ea}^{(2)}$	0.15	0.57	0.94	1.3	1.7
$k_{ai}^{(2)}$	1.2	3.7	7.7	14	25

[a]The effective rate constants were determined by least square second-order polynomial fits to Eq. (6.11) ($\rho_P = 0$), as shown in Fig. 6.15.

The subthreshold photoionization spectra of CH_3I/Ar at constant ρ_{Ar}, along with the peak areas of this structure plotted versus ρ_{CH_3I}, are presented in Figs. 6.16a and 6.16b. Analogous data are shown for CH_3I/Ar at constant ρ_{CH_3I} in Figs. 6.16a′ and 6.16b′. The quadratic dependence of the subthreshold photocurrent on ρ_{CH_3I} (cf. Fig. 6.16b), coupled with the linear dependence of this photocurrent on ρ_{Ar} (cf. Fig. 6.16b′), indicates that the CH_3I/Ar subthreshold photocurrent arises via pathway 2.

Similarly, the subthreshold photoionization spectra of CH_3I/CF_4 at constant ρ_{CF_4}, along with the peak areas of this structure plotted versus ρ_{CH_3I}, are presented in Figs. 6.17a and 6.17b. Analogous data are shown for CH_3I/CF_4 at constant ρ_{CH_3I} in Figs. 6.17a′ and 6.17b′. Again, the quadratic dependence of the subthreshold photocurrent on ρ_{CH_3I} and the linear dependence of this photocurrent on ρ_{CF_4} imply that the CH_3I/CF_4 subthreshold structure proceeds through pathway 2.

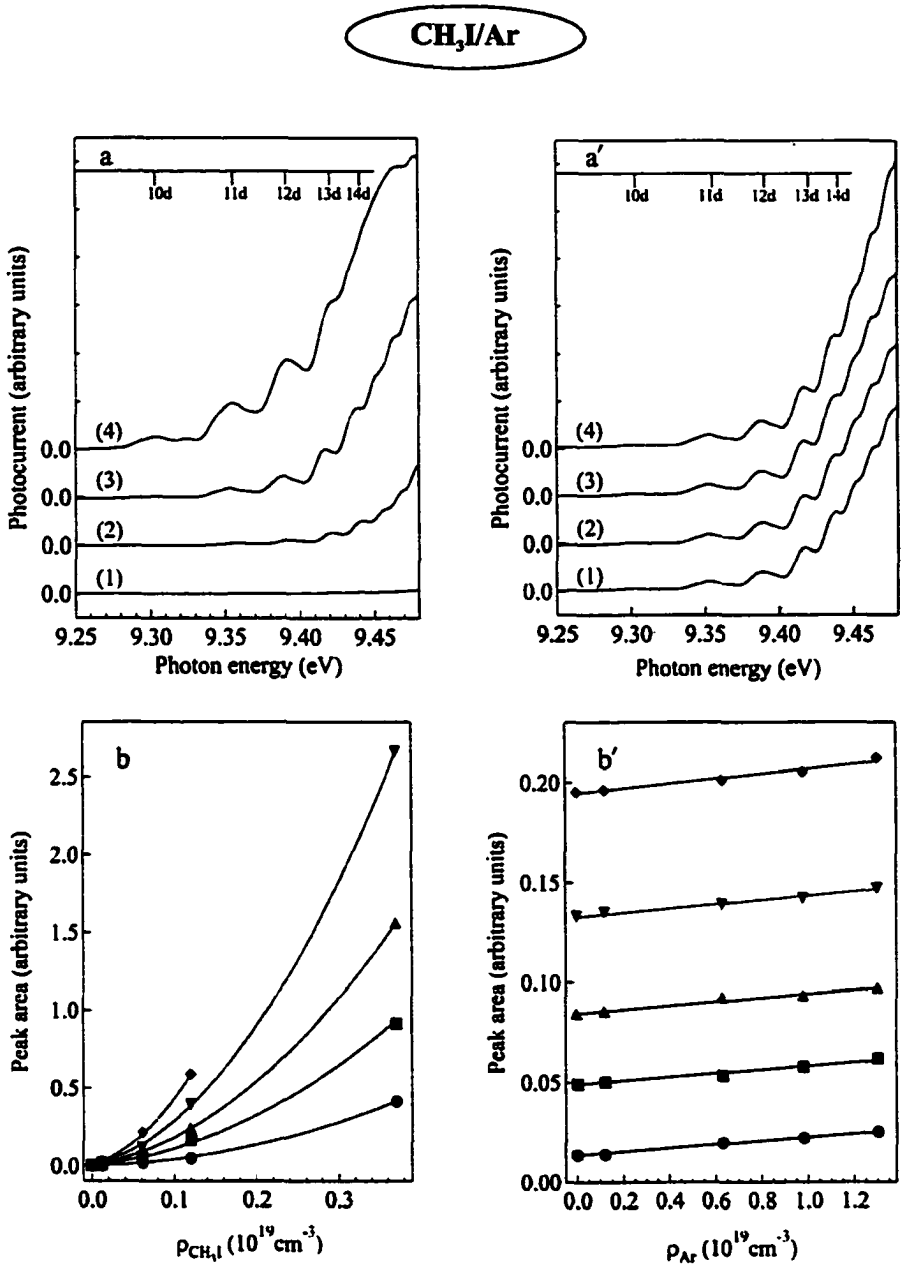

Fig. 6.16. Subthreshold photoionization spectra of CH_3I/Ar: (a) photoionization spectra of varying CH_3I number densities ρ_{CH_3I} ($10^{19}cm^{-3}$) perturbed by 0.63 × 10^{19} cm^{-3} Ar: (1) 0.00024, (2) 0.012, (3) 0.061, and (4) 0.37. (a′) Photoionization spectra of 0.061 × 10^{19} cm^{-3} CH_3I perturbed by varying Ar number densities ρ_{Ar}($10^{19}cm^{-3}$): (1) 0.12, (2) 0.63, (3) 0.98, and (4) 1.3. (b) Peak areas for the subthreshold photoionization structure in (a) plotted vs. ρ_{CH_3I}. (b′) Peak areas for the subthreshold photoionization structure in (a′) plotted vs. ρ_{Ar}. In (b) and (b′): (●) 10d, (■) 11d, (▲) 12d, (▼) 13d, and (◆) 14d. The solid lines represent linear least-square fits to Eq. (6.11). See text for discussion. See Chapter 4 for experimental details.

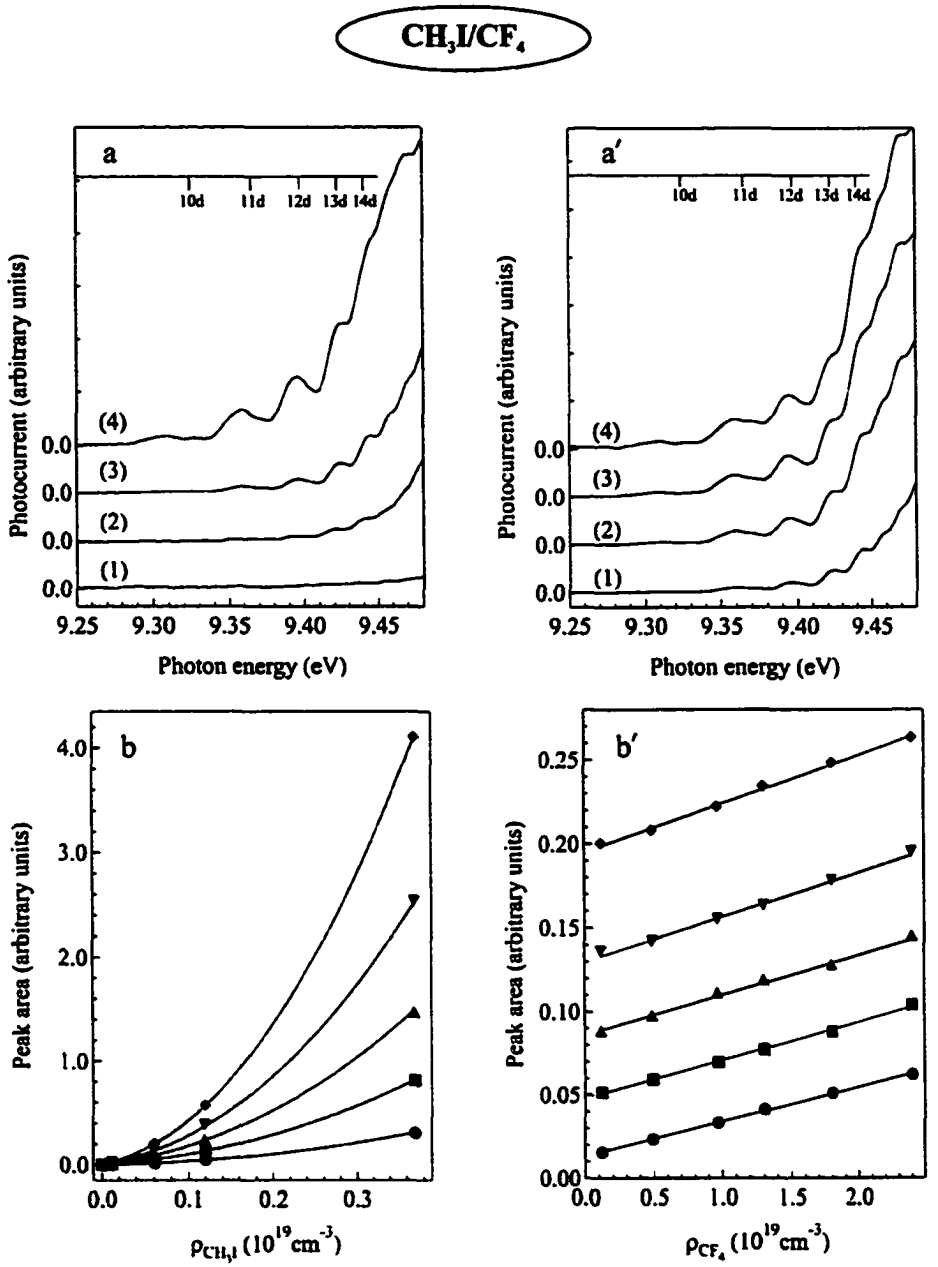

Fig. 6.17. Subthreshold photoionization of CH_3I/CF_4: (a) subthreshold photoionization spectra of varying ρ_{CH_3I} ($10^{19}cm^{-3}$) perturbed by 0.12×10^{19} cm^{-3} CF_4: (1) 0.00024, (2) 0.012, (3) 0.061, and (4) 0.37. (a′) Subthreshold photoionization spectra of 0.061×10^{19} cm^{-3} CH_3I perturbed by varying ρ_{CF_4} ($10^{19}cm^{-3}$): (1) 0.12, (2) 0.97, (3) 1.8, and (4) 2.4. (b) Peak areas for the subthreshold photoionization structure in (a) plotted vs. ρ_{CH_3I}. (b′) Peak areas for the subthreshold photoionization structure in (a′) plotted vs. ρ_{CF_4}. In (b) and (b′): (●) 10d, (■) 11d, (▲) 12d, (▼) 13d, and (◆) 14d. The solid lines represent least-square second-order polynomial fits to Eq. (6.11). See Chapter 4 for experimental details.

In Fig. 6.18a and 6.18b, the subthreshold photoionization spectra of CH_3I/CO_2 at constant ρ_{CH_3I} and the peak areas of this structure plotted versus ρ_{CO_2}, respectively, are presented. Similar data for CH_3I/N_2 are shown in Figs. 6.18a′ and 6.18b′. The strong absorption features of CO_2 and N_2 in this same energy region increase the difficulty of measuring subthreshold photoionization spectra for increasing ρ_{CH_3I}. However, the linearity of the peak areas as a function of perturber number density, coupled with the low electron affinities of N_2 and CO_2, indicates that the subthreshold photocurrent in these systems also proceeds through pathway 2.

Subthreshold photoionization spectra of CH_3I perturbed by c-C_4F_8 for constant $\rho_{c\text{-}C_4F_8}$ and constant ρ_{CH_3I} are shown in Figs. 6.19a and 6.19a′, respectively, and the peak areas obtained from these spectra are plotted versus $\rho_{c\text{-}C_4F_8}$ and ρ_{CH_3I} in Figs. 6.19b and 6.19b′, respectively. Analogous data for CH_3I perturbed by SF_6 are presented in Fig. 6.20. As in the case of CH_3I/Ar and CF_4, the quadratic dependence of this subthreshold structure on ρ_{CH_3I}, and the linear dependence on ρ_P (P = c-C_4F_8, SF_6), indicate that the subthreshold photocurrent follows pathway 2. However, the lower onset energy observed for CH_3I/c-C_4F_8 and SF_6, in comparison to CH_3I/Ar and CF_4 when ρ_{CH_3I} is small, suggests that pathway 1 is also accessible. Therefore, accurate modeling of the CH_3I/c-C_4F_8 and SF_6 subthreshold photocurrent over the entire density range requires the use of Eq. (6.12).

b. Discussion

The determination of the effective rate constants for electron attachment and associative ionization requires a variation in both ρ_{CH_3I} and ρ_P. We begin the evaluation of these constants by studying the density dependence of the subthreshold photocurrent when ρ_P is varied at different constant values of ρ_{CH_3I}. For constant ρ_{CH_3I}, the total subthreshold photocurrent for pathway 2 (i.e., Eq. (6.11)) and the sum of the two pathways (i.e., Eq.

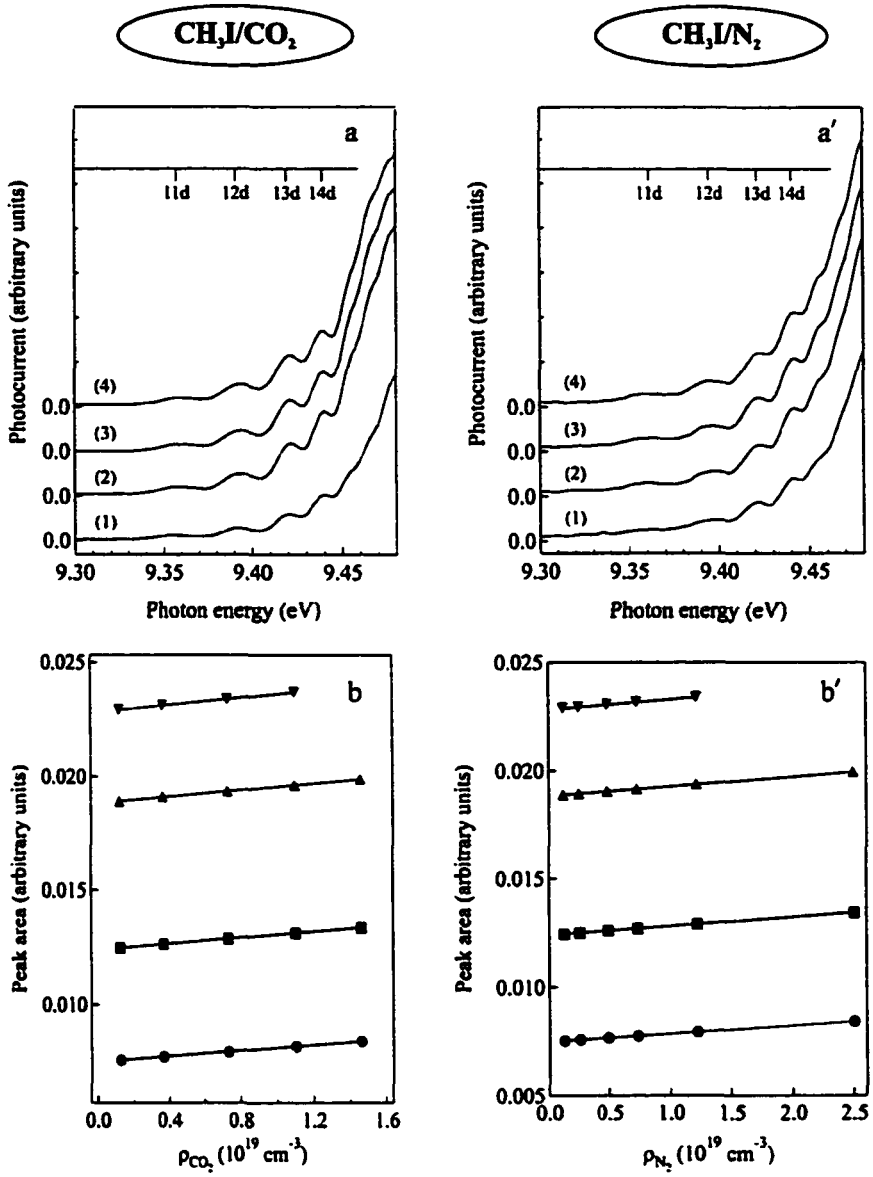

Fig. 6.18. (a) subthreshold photoionization spectra of 0.012 x 10^{19} cm^{-3} CH_3I perturber by varying CO_2 number densities ρ_{CO_2} (10^{19} cm^{-3}): (1) 0.12, (2) 0.73, (3) 1.1, and (4) 1.5. (a′) Subthreshold photoionization spectra of 0.012 × 10^{19} cm^{-3} CH_3I perturbed by varying N_2 number densities ρ_{N_2} ($10^{19}cm^{-3}$): (1) 0.12, (2) 0.49, (3) 1.2, and (4) 2.5. (b) Peak areas for the subthreshold photoionization structure in (a) plotted vs. ρ_{CO_2}. (b′) Peak areas for the subthreshold photoionization structure in (a′) plotted vs. ρ_{N_2}. In (b) and (b′): (●) 10d, (■) 11d, (▲) 12d, (▼) 13d, and (◆) 14d. The solid lines represent least-square second-order polynomial fits to Eq. (6.11). All spectra were taken in Cell 2 with a resolution of ~ 10 meV in the spectral range of interest. See Chapter 4 for experimental details.

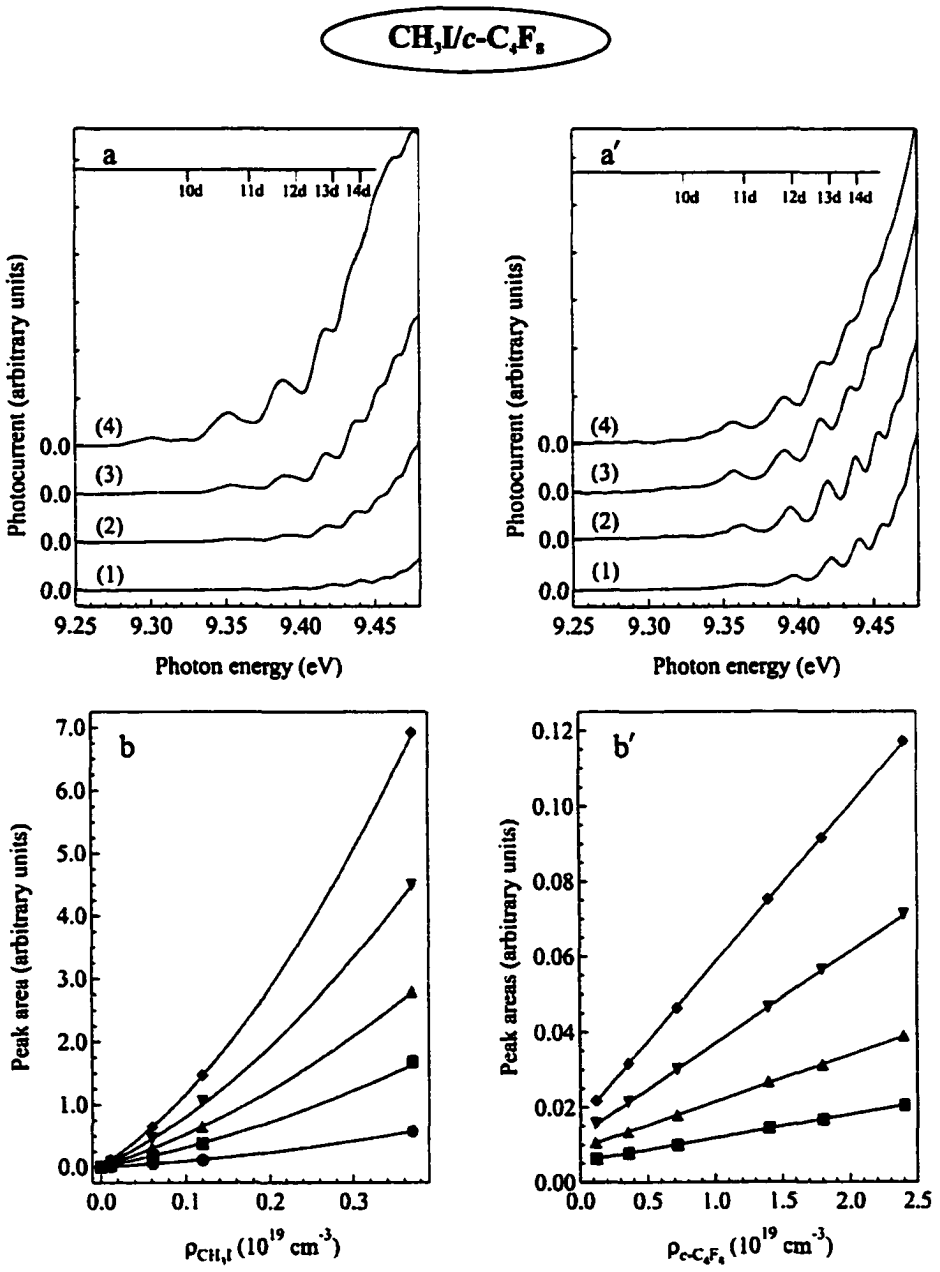

Fig. 6.19. Subthreshold photoionization of $CH_3I/c\text{-}C_4F_8$: **(a)** Subthreshold photoionization spectra of varying ρ_{CH_3I} ($10^{19}cm^{-3}$) perturbed by 0.12×10^{19} cm^{-3} $c\text{-}C_4F_8$: (1) 0.00024, (2) 0.012, (3) 0.061, and (4) 0.37. **(a′)** Subthreshold photoionization spectra of 0.00024×10^{19} cm^{-3} CH_3I perturbed by varying $\rho_{c\text{-}C_4F_8}$ ($10^{19}cm^{-3}$): (1) 0.12, (2) 0.72, (3) 1.8, and (4) 2.4. **(b)** Peak areas for the subthreshold photoionization structure in **(a)** plotted vs. ρ_{CH_3I}. **(b′)** Peak areas for the subthreshold photoionization structure in **(a′)** plotted vs. $\rho_{c\text{-}C_4F_8}$. In **(b)** and **(b′)**: (●) 10d, (■) 11d, (▲) 12d, (▼) 13d, and (◆) 14d. The solid lines represent least-square second-order polynomial fits to Eq. (6.12). See Chapter 4 for experimental details.

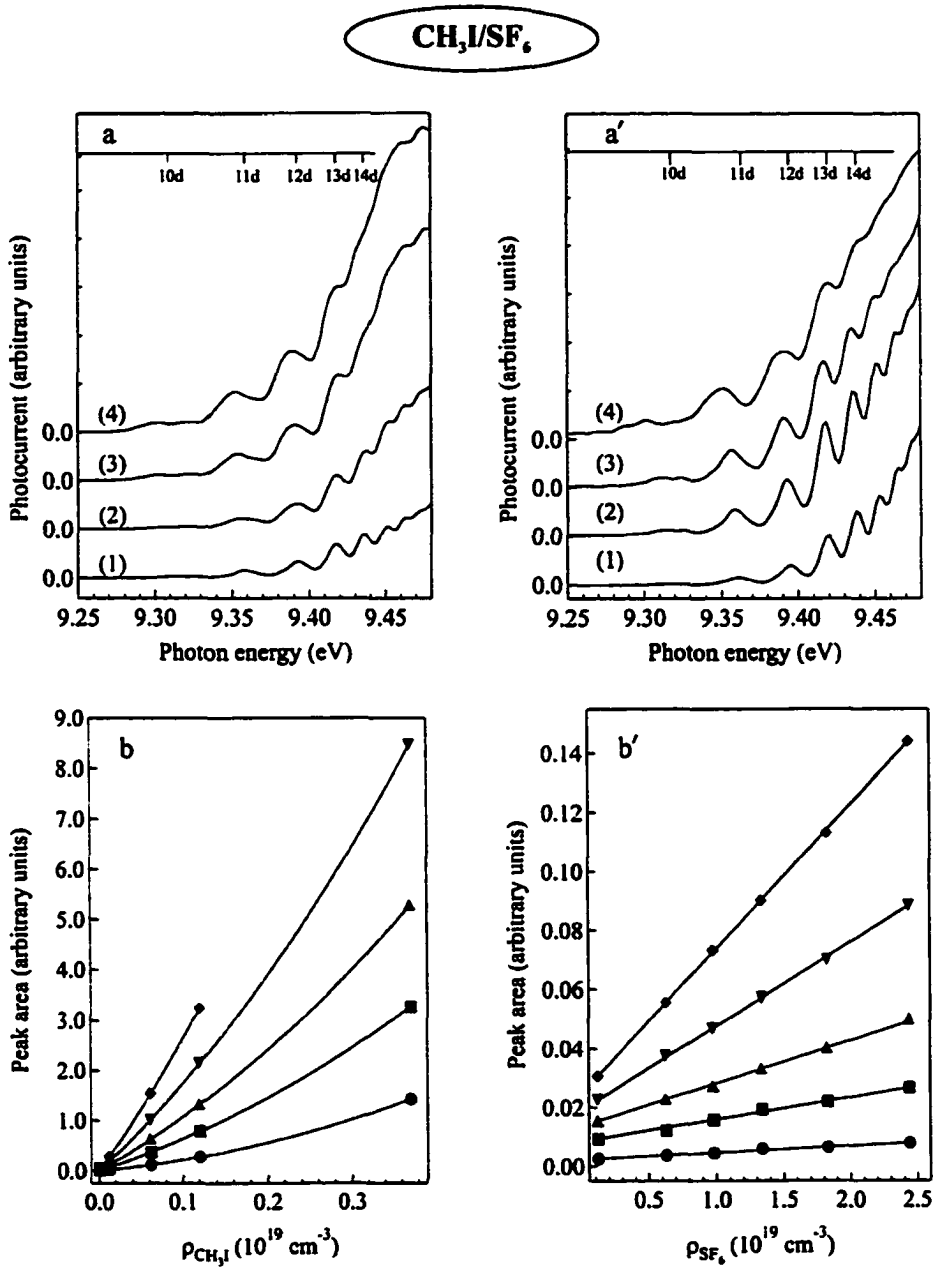

Fig. 6.20. Subthreshold photoionization spectra of CH_3I/SF_6: (a) photoionization spectra of varying CH_3I number densities ρ_{CH_3I} ($10^{19}cm^{-3}$) perturbed by 0.63×10^{19} cm^{-3} SF_6: (1) 0.00024, (2) 0.012, (3) 0.12, and (4) 0.37. (a') Photoionization spectra of 0.061×10^{19} cm^{-3} CH_3I perturbed by varying SF_6 number densities ρ_{SF_6} ($10^{19}cm^{-3}$): (1) 0.12, (2) 0.63, (3) 1.3, and (4) 2.4. (b) Peak areas for the subthreshold photoionization structure in (a) plotted vs. ρ_{CH_3I}. (b') Peak areas for the subthreshold photoionization structure in (a') plotted vs. ρ_{SF_6}. In (b) and (b'): (●) 10d, (■) 11d, (▲) 12d, (▼) 13d, and (◆) 14d. The solid lines represent least-square second-order polynomial fits to Eq. (6.12). See text for discussion. See Chapter 4 for experimental details.

(6.12)) reduces to the same form, namely Eq. (6.13). The ρ_{CH_3I} dependence of the regression coefficients b_0 and b_1 differs significantly for each pathway, however. For pathway 2, the coefficients b_0 and b_1 are

$$b_0 = k_{ea}^{(2)} \rho_{CH_3I} + k_{ai}^{(2)} \rho_{CH_3I}^2 , \; b_1 = k_{ai}^{\prime(2)} \rho_{CH_3I}^2 , \tag{6.15}$$

whereas for the sum of the two pathways, these coefficients become

$$b_0 = (k_{ea}^{(2)} + k_{ea}^{(1)}) \rho_{CH_3I} + k_{ai}^{(2)} \rho_{CH_3I}^2 , \; b_1 = k_{ai}^{(1)} \rho_{CH_3I} + k_{ai}^{\prime(2)} \rho_{CH_3I}^2 . \tag{6.16}$$

Since pathway 2 was invoked to explain the subthreshold photoionization structure observed in CH_3I/Ar, CF_4, CO_2 and N_2 (cf. Figs. 6.16 - 6.18), the ρ_{CH_3I} dependence of the coefficients b_0 and b_1 should be given by Eq. (6.15). Therefore, if b_0 and b_1 are obtained for various values of ρ_{CH_3I}, and if b_0 and b_1 show the correct quadratic dependence upon ρ_{CH_3I}, then pathway 2 has been substantiated, and the effective rate constants $k_{ea}^{(2)}$, $k_{ai}^{(2)}$ and $k_{ai}^{\prime(2)}$ can be determined. The values for b_0 and b_1, obtained as described above, for various values of ρ_{CH_3I} are given in Tables 6.6 (CH_3I/Ar) and 6.7 (CH_3I/CF_4), and are plotted as functions of ρ_{CH_3I} in Fig. 6.21. (The peak areas used to obtain b_0 and b_1 are given in Appendix 3.C.i (CH_3I/Ar) and 3.C.ii (CH_3I/CF_4).) A nonlinear least-square regression analysis on the data of Fig. 6.21 shows that b_0 and b_1 are quadratically dependent upon ρ_{CH_3I}. Evaluating b_0 and b_1 using Eq. (6.15) then leads to a determination of the effective rate constants $k_{ea}^{(2)}$, $k_{ai}^{(2)}$ and $k_{ai}^{\prime(2)}$, which are also given in Tables 6.6 (CH_3I/Ar) and 6.7 (CH_3I/CF_4). The electron attachment rate constant $k_{ea}^{(2)}$ obtained here should be equivalent to that determined directly from the analysis of the pure CH_3I spectra (cf. Fig. 6.15 and Table 6.5). Similarly, the value of the associative ionization constant $k_{ai}^{(2)}$ determined here should be equivalent to $k_{ai}^{(2)}$ obtained from pure CH_3I (cf. Fig. 6.15 and Table 6.5). In both cases, these rate constants agree remarkably well with one another. Although the necessary data needed to directly evaluate

Table 6.6. (a) The constant regression coefficient b_0 and (b) the linear regression coefficient b_1 determined from a pressure study of the subthreshold photoionization structure of CH_3I/Ar as a function of ρ_{CH_3I} (10^{19} cm^{-3}).

a. b_0

ρ_{CH_3I}	10d	11d	12d	13d	14d
0.00024	0.00	0.00	0.00	0.00	0.00
0.012	0.00	0.0074	0.012	0.018	0.024
0.061	0.013	0.049	0.084	0.11	0.19
0.12	0.040	0.14	0.22	0.37	0.56
0.37	0.21	0.73	1.4	2.4	
Effective rate constants (arbitrary units) [a]					
$k_{ea}^{(2)}$	0.15	0.57	0.94	1.3	1.7
$k_{ai}^{(2)}$	1.2	3.7	7.6	14	25

b. b_1

ρ_{CH_3I}	10d	11d	12d	13d	14d
0.00024	0.00	0.00	0.00	0.00	0.00
0.012	0.00	0.0035	0.0036	0.0040	0.0057
0.061	0.0087	0.0089	0.0095	0.011	0.012
0.12	0.033	0.035	0.037	0.039	0.045
0.37	0.32	0.33	0.35	0.38	
Effective rate constant (arbitrary units) [a]					
$k_{ai}'^{(2)}$	2.3	2.4	2.6	2.8	3.0

[a] The effective rate constants $k_{ea}^{(2)}$, $k_{ai}^{(2)}$ and $k_{ai}'^{(2)}$ were determined by least-square second-order polynomial fits to Eq. (6.15), as shown in Figs. 6.21a and 6.21b.

Table 6.7. (a) The constant regression coefficients b_0 and (b) the linear regression coefficients b_1 determined from a pressure study of the subthreshold photoionization structure of CH_3I/CF_4 as a function of ρ_{CH_3I} (10^{19} cm^{-3}).

a. b_0

ρ_{CH_3I}	10d	11d	12d	13d	14d
0.00024	0.00	0.00	0.00	0.00	0.00
0.012	0.00	0.0075	0.012	0.018	0.024
0.061	0.014	0.048	0.086	0.13	0.20
0.12	0.035	0.12	0.22	0.36	0.55
0.37	0.22	0.71	1.4	2.4	4.0
Effective rate constants (arbitrary units)[a]					
$k_{ea}^{(2)}$	0.15	0.58	0.92	1.3	1.7
$k_{ai}^{(2)}$	1.3	3.6	7.7	14	25

b. b_1

ρ_{CH_3I}	10d	11d	12d	13d	14d
0.00024	0.00	0.00	0.00	0.00	0.00
0.012	0.00	0.0082	0.0087	0.0094	0.010
0.061	0.021	0.023	0.024	0.026	0.029
0.12	0.080	0.083	0.089	0.095	0.11
0.37	0.76	0.79	0.83	0.92	0.99
Effective rate constant (arbitrary units)[a]					
$k'^{(2)}_{ai}$	5.5	5.8	6.1	6.7	7.3

[a]The effective rate constants $k_{ea}^{(2)}$, $k_{ai}^{(2)}$ and $k'^{(2)}_{ai}$ are for least-square second-order polynomial fits to Eq. (6.15), as shown in Figs. 6.21a′ and 6.21b′.

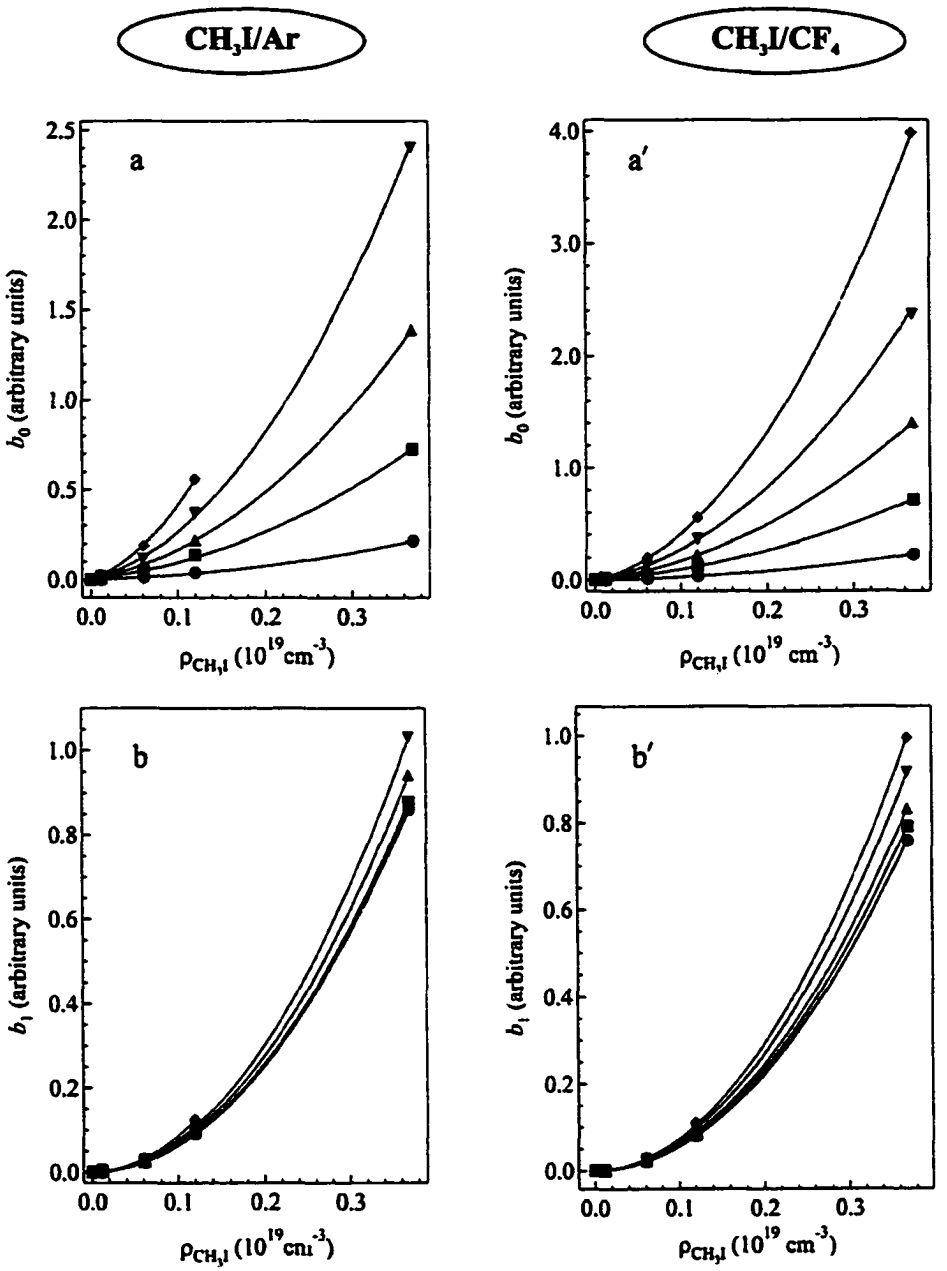

Fig. 6.21. **(a)** Constant and **(b)** linear regression coefficients (cf. Table 6.6) for the subthreshold density dependence of CH_3I/Ar plotted vs. ρ_{CH_3I}. **(a′)** Constant and **(b′)** linear regression coefficients (cf. Table 6.7) for the subthreshold density dependence of CH_3I/CF_4 plotted vs. ρ_{CH_3I}. (●) 10d, (■) 11d, (▲) 12d, (▼) 13d, and (◆) 14d. The solid lines represent least-square second-order polynomial fits to Eq. (6.15). See text for discussion.

all of the rate constants for CH_3I/N_2 and CH_3I/CO_2 were not obtained, the values for the effective rate constant $k'^{(2)}_{ai}$ for perturber stabilized associative ionization of CH_3I can be evaluated for N_2 and CO_2 by using the values of $k^{(2)}_{ea}$ and $k^{(2)}_{ai}$ determined from pure CH_3I (cf. Table 6.5). These values are given in Table 6.8. (The peak areas and regression coefficients b_0 and b_1 used to obtain these effective rate constants are given in Appendix 3.C.iii.)

Table 6.8. The effective rate constant for perturber-stabilized associative ionization $k'^{(2)}_{ai}$ for the perturbers CO_2 and N_2. See text for discussion.

Perturber	11d	12d	13d	14d
CO_2	3.6	3.9	4.3	4.8
N_2	2.4	2.6	2.8	3.0

As discussed above, an explanation of the density dependence of $CH_3I/c\text{-}C_4F_8$ and SF_6 should require both pathways 1 and 2 and, therefore, b_0 and b_1 are given by Eq. (6.16) in this case. In Fig. 6.22a and 6.22b, respectively, b_0 and b_1 are plotted as functions of ρ_{CH_3I} for the $CH_3I/c\text{-}C_4F_8$ system. Analogous data for the CH_3I/SF_6 system are presented in Figs. 6.22a′ and 6.22b′. The values of b_0 and b_1 are given in Table 6.9 ($CH_3I/c\text{-}C_4F_8$) and Table 6.10 (CH_3I/SF_6), along with the effective rate constants $k^{(1)}_{ea}$, $k^{(1)}_{ai}$, $k^{(2)}_{ai}$ and $k'^{(2)}_{ai}$ obtained from least-square second-order polynomial fits of b_0 and b_1 to Eq. (6.16). One must point out that, from the regression analysis of b_0, only $k^{(2)}_{ai}$ and the sum of the electron attachment rate constants $k^{(2)}_{ea} + k^{(1)}_{ea}$ are obtained. However, since $k^{(2)}_{ai}$ obtained from this analysis agrees, to within experimental error, with $k^{(2)}_{ai}$ as determined from pure CH_3I (cf. Table 6.5), CH_3I/Ar (cf. Table 6.6) and CH_3I/CF_4 (cf. Table 6.7), the $k^{(2)}_{ea}$ values determined from pure CH_3I have been used in order to obtain the $k^{(1)}_{ea}$ values reported here. (The peak areas used to obtain the b_0 and b_1 values presented in Tables 6.9 and 6.10 are given in Appendix 3.C.iv ($CH_3I/c\text{-}C_4F_8$) and 3.C.v (CH_3I/SF_6).)

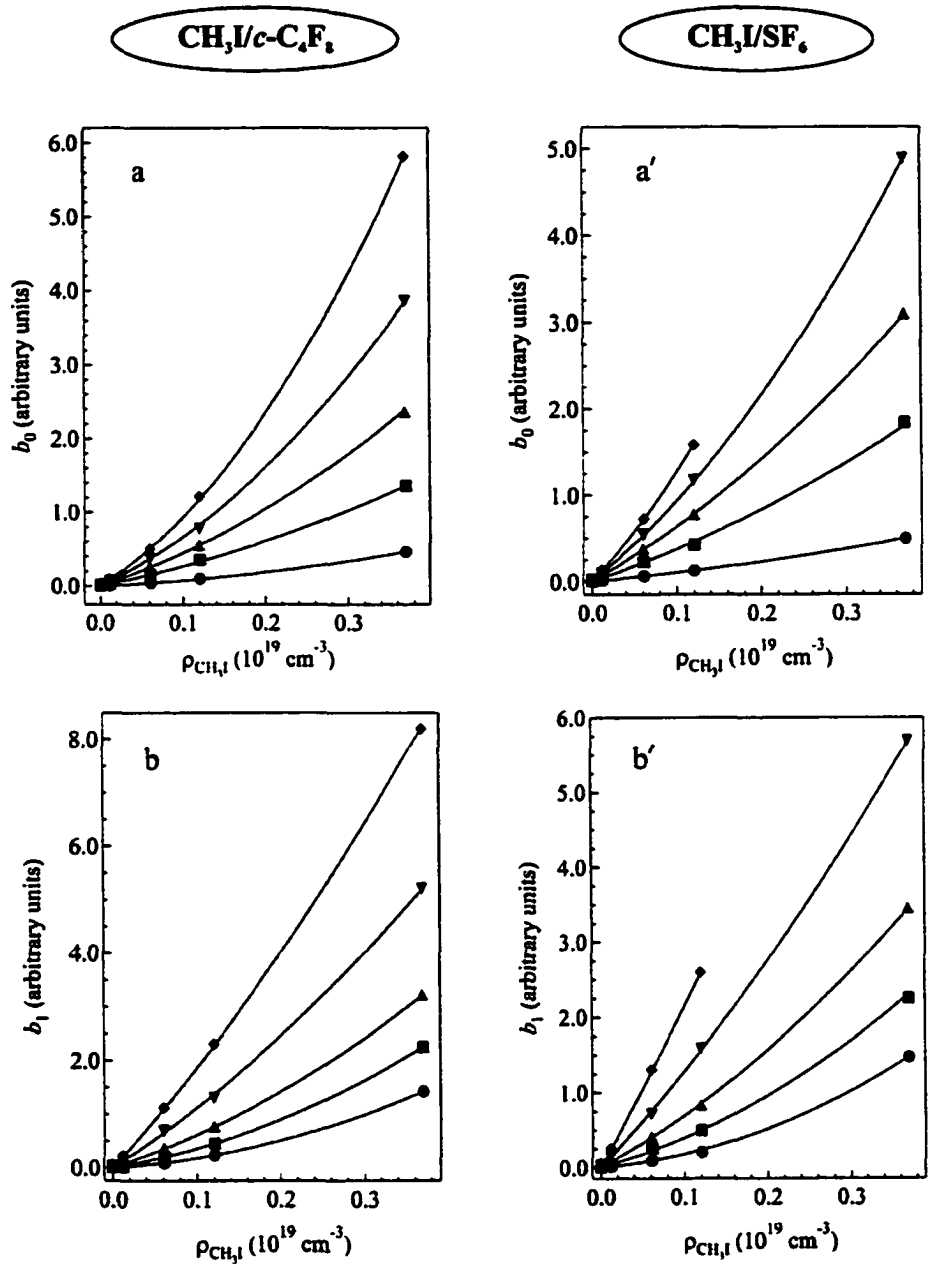

Fig. 6.22. **(a)** Constant and **(b)** linear regression coefficients (cf. Table 6.9) for the subthreshold density dependence of $CH_3I/c\text{-}C_4F_8$ plotted vs. ρ_{CH_3I}. **(a′)** Constant and **(b′)** linear regression coefficients (cf. Table 6.10) for the subthreshold density dependence of CH_3I/SF_6 plotted vs. ρ_{CH_3I}. (●) 10d, (■) 11d, (▲) 12d, (▼) 13d, and (◆) 14d. The solid lines represent least-square second-order polynomial fits to Eq. (6.16). See text for discussion.

Table 6.9. (a) The constant regression coefficients b_0 and (b) the linear regression coefficients b_1 determined from a pressure study of the subthreshold photoionization structure of $CH_3I/c\text{-}C_4F_8$ as a function of ρ_{CH_3I} (10^{19} cm^{-3}).

a. b_0

ρ_{CH_3I}	10d	11d	12d	13d	14d
0.00024	0.00	0.0055	0.0090	0.013	0.017
0.012	0.0075	0.028	0.046	0.065	0.086
0.061	0.041	0.15	0.26	0.37	0.51
0.12	0.090	0.33	0.56	0.83	1.2
0.37	0.46	1.4	2.4	3.9	5.8
Effective rate constants (arbitrary units)[a]					
$k_{ea}^{(1)}$	0.38	1.7	2.8	4.0	5.3
$k_{ai}^{(2)}$	1.1	3.7	7.5	14	24

b. b_1

ρ_{CH_3I}	10d	11d	12d	13d	14d
0.00024	0.00	0.0061	0.012	0.024	0.041
0.012	0.011	0.033	0.064	0.12	0.21
0.061	0.084	0.19	0.35	0.66	1.1
0.12	0.23	0.45	0.76	1.4	2.3
0.37	1.4	2.3	3.2	5.2	8.2
Effective rate constants (arbitrary units)[a]					
$k_{ai}^{(1)}$	0.80	2.6	5.2	10	17
$k_{ai}^{\prime(2)}$	8.9	9.3	9.9	11	12

The effective rate constants $k_{ai}^{(1)}$, $k_{ai}^{(2)}$ and $k_{ai}^{\prime(2)}$ are from least-square second-order polynomial fits to Eq. (6.16), as shown in Figs. 6.22a and 6.22b. The rate constant $k_{ea}^{(1)}$ results from subtracting the value for $k_{ea}^{(2)}$ obtained from pure CH_3I (cf. Table 6.5) from the first-order regression coefficient of the least-square fits of b_0 (see text for details).

Table 6.10. (a) The constant regression coefficient b_0 and (b) the linear regression coefficient b_1 determined from a pressure study of the subthreshold photoionization structure of CH_3I/SF_6 as a function of ρ_{CH_3I} (10^{19} cm^{-3}).

a. b_0

ρ_{CH_3I}	10d	11d	12d	13d	14d
0.00024	0.0010	0.0025	0.0094	0.018	0.025
0.012	0.011	0.042	0.067	0.099	0.13
0.061	0.060	0.23	0.37	0.54	0.72
0.12	0.13	0.43	0.77	1.2	1.6
0.37	0.49	1.8	3.1	4.9	
Effective rate constants (arbitrary units) [a]					
$k_{ea}^{(1)}$	0.77	2.9	4.7	6.6	8.7
$k_{ai}^{(2)}$	1.1	3.8	7.5	14	24

b. b_1

ρ_{CH_3I}	10d	11d	12d	13d	14d
0.00024	0.0056	0.0095	0.019	0.031	0.060
0.012	0.013	0.039	0.074	0.14	0.25
0.061	0.090	0.25	0.40	0.71	1.3
0.12	0.20	0.50	0.83	1.6	2.6
0.37	1.5	2.3	3.5	5.7	
Effective rate constants (arbitrary units) [a]					
$k_{ai}^{(1)}$	0.95	3.1	6.1	12	20
$k_{ai}^{\prime(2)}$	8.2	8.3	8.9	9.6	11

The effective rate constants $k_{ai}^{(1)}$, $k_{ai}^{(2)}$ and $k_{ai}^{\prime(2)}$ were determined by least-squares second-order polynomial fits to Eq. (6.16) as shown in Figs. 6.22a′ and 6.22b′. The rate constant $k_{ea}^{(1)}$ results from subtracting the value for $k_{ea}^{(2)}$ obtained from pure CH_3I (cf. Table 6.5) from the first-order regression coefficient of the least-square fits of b_0 (see text for discussion).

Similar to the C_2H_5I and C_6H_6 systems presented above, the n dependence of the effective rate constants for CH_3I/P (P = Ar, CF_4, c-C_4F_8, CO_2, N_2 and SF_6) can be used to validate further the above choice of pathways. Moreover, variations in the rate constants for different perturbers can also be investigated for the data presented in this Section. In Fig. 6.23a, the effective rate constants for electron attachment to CH_3I (i.e., $k_{ea}^{(2)}$ (CH_3I)), for electron attachment to c-C_4F_8 (i.e., $k_{ea}^{(1)}$ (c-C_4F_8)) and for electron attachment to SF_6 (i.e., $k_{ea}^{(1)}$ (SF_6)) are plotted versus n. The associative ionization rate constants for CH_3I homomolecular dimerization (i.e., $k_{ai}^{(2)}$ (CH_3I)), for CH_3I/c-C_4F_8 heteromolecular dimerization (i.e., $k_{ai}^{(1)}$ (c-C_4F_8)) and for CH_3I/SF_6 heteromolecular dimerization (i.e., $k_{ai}^{(1)}$ (SF_6)) are plotted as functions of n^7 in Fig. 6.23b. Likewise, in Fig. 6.23c, the perturber-stabilized associative ionization rate constants $k_{ai}^{\prime(2)}$ for CH_3I/P (P = Ar, CF_4, c-C_4F_8, CO_2, N_2 and SF_6) are plotted versus n^7. Clearly, $k_{ea}^{(1,2)}$ is linearly dependent on n, and $k_{ai}^{(1,2)}$ and $k_{ai}^{\prime(2)}$ are directly proportional to n^7. One can conclude, therefore, that electron attachment (i.e., Eqs. (6.1) and (6.3)) and associative ionization (i.e., Eqs. (6.2), (6.4) and (6.5)) are sufficient to explain the density dependence of the subthreshold photocurrent observed in CH_3I.

Fig. 6.23a also shows that $k_{ea}^{(1)}$ (SF_6) > $k_{ea}^{(1)}$ (c-C_4F_8) > $k_{ea}^{(2)}$ (CH_3I). If the electron attachment rate constant increases linearly with increasing stability of the molecular anion, then normalization of $k_{ea}^{(1,2)}$ to the electron affinity of the neutral species involved in anion formation (i.e., CH_3I, c-C_4F_8, and SF_6) should result in a single linear correlation. In Fig. 6.24a, we present $k_{ea}^{(1,2)}$ normalized in this way to electron affinity and plotted as a function of n. This figure shows, to within experimental error, that one correlation line does indeed result. (In Fig. 6.24a, $k_{ea}^{(2)}$ (CH_3I), $k_{ea}^{(1)}$ (c-C_4F_8) and $k_{ea}^{(1)}$ (SF_6) are normalized to the electron affinities given in Table 6.11.)

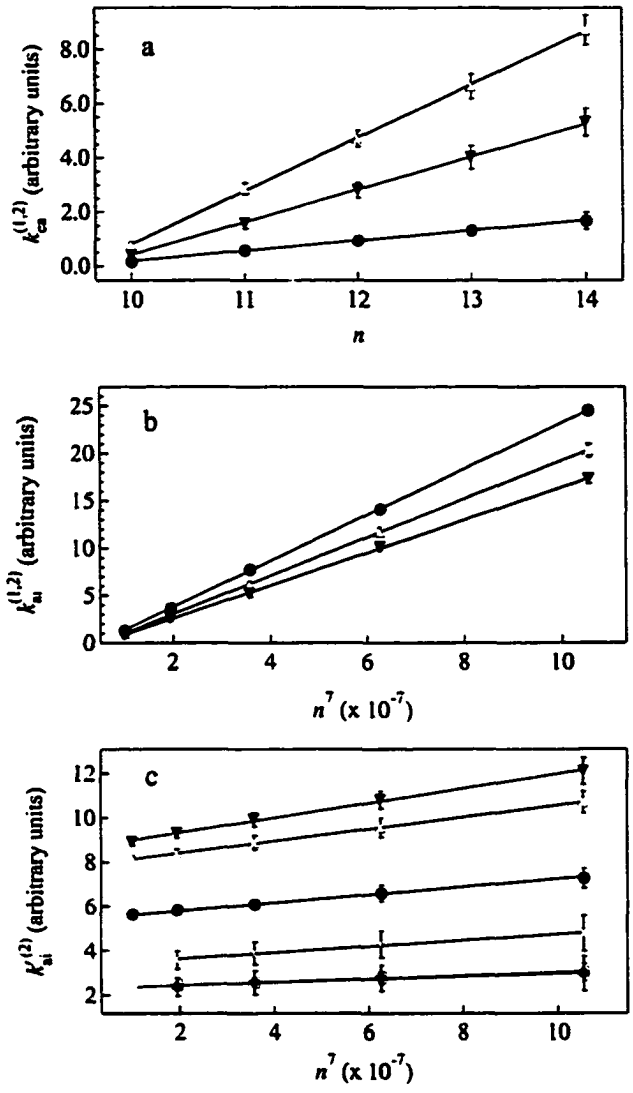

Fig. 6.23. **(a)** Effective rate constants $k_{ca}^{(1,2)}$ for electron attachment to c-C_4F_8 (i.e., Eq. (6.1) and Table 6.9), CH_3I (i.e., Eq. (6.3) and Table 6.5) and SF_6 (i.e., Eq. (6.3) and Table 6.10) plotted vs. CH_3I excited-state principal quantum number n. (▼) c-C_4F_8, (●) CH_3I and (△) SF_6. **(b)** Effective rate constants $k_{ai}^{(1,2)}$ for associative ionization of CH_3I with c-C_4F_8 (i.e., Eq. (6.2) and Table 6.9), with CH_3I (i.e., Eq. (6.4) and Table 6.5), and with SF_6 (i.e., Eq. (6.2) and Table 6.10) plotted vs. n^7. (▼) c-C_4F_8, (●) CH_3I and (△) SF_6. **(c)** Effective rate constants $k'^{(2)}_{ai}$ for the perturber-stabilized associative ionization of CH_3I (i.e., Eq. (6.5)) plotted vs. n^7. (□) Ar (cf. Table 6.6), (●) CF_4 (cf. Table 6.7), (▼) c-C_4F_8 (cf. Table 6.9), (◇) CO_2 (cf. Table 6.8), (◆) N_2 (cf. Table 6.8), and (△) SF_6 (cf. Table 6.10). The solid lines are linear least-square fits to the data. The error bars for the effective rate constants result from the assumption of a variance of ± 1 standard deviation in both the fitting of the subthreshold peaks and the regression analysis used to obtain these rate constants. See text for discussion.

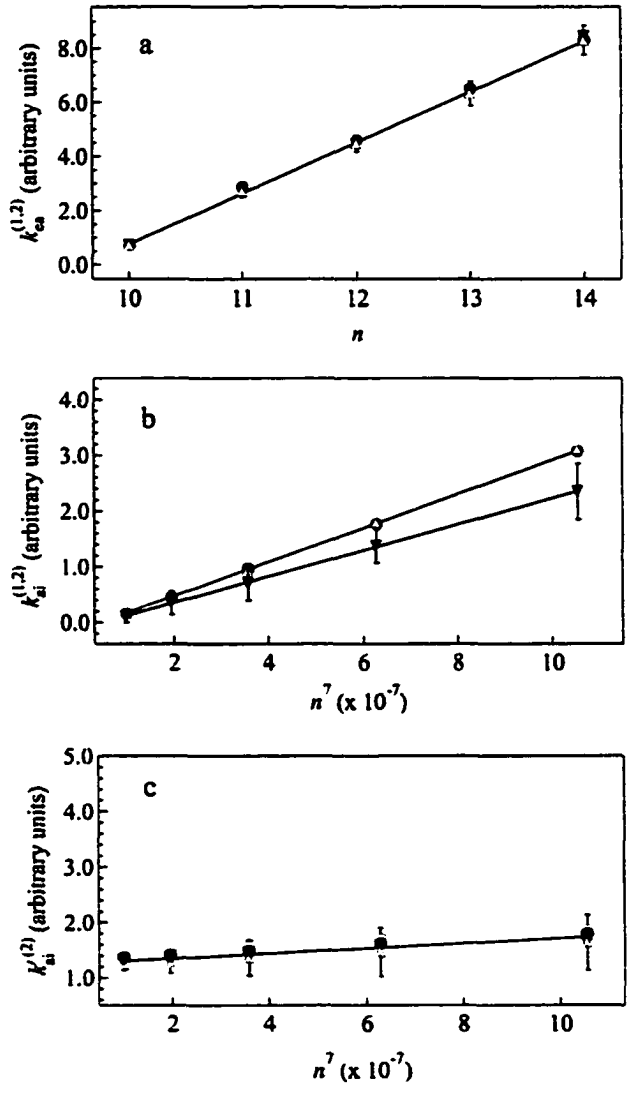

Fig. 6.24. **(a)** The effective rate constants $k_{ea}^{(1,2)}$ for c-C_4F_8 (▼), CH_3I (●) and SF_6 (△) normalized to the electron affinity of c-C_4F_8, CH_3I, and SF_6, respectively. **(b)** The effective rate constants $k_{ai}^{(1,2)}$ for c-C_4F_8 (▼), CH_3I (●) and SF_6 (△) normalized to the ground-state polarizability of c-C_4F_8, SF_6, and CH_3I, respectively. **(c)** The effective rate constants $k_{ai}^{\prime(2)}$ for Ar (□), CF_4 (●), c-C_4F_8 (▼), CO_2 (◇), N_2 (◆), and SF_6 (△) normalized to the ground-state polarizability of the perturber. The error bars shown for the effective rate constants are the maximum errors from Fig. 6.23. See Table 6.11 for the values of the electron affinities and ground-state polarizabilities used.

Table 6.11. Adiabatic electron affinities (EA) and ground-state polarizabilities (α) of CH_3I and the perturbers used in this work.

Molecule	EA (eV)	Ref.	α (10^{-24} cm^3)	Ref.
Ar	—		1.6411	[65,66]
CF_4	—		3.838	[139]
c-C_4F_8	0.630	[153]	7.37	[142]
CH_3I	0.20	[154]	7.97	[155]
CO_2	—		2.911	[156]
N_2	—		1.7403	[65,66]
SF_6	1.05	[157]	6.54	[144]

From Fig. 6.24b, $k_{ai}^{(2)}(CH_3I) > k_{ai}^{(1)}(SF_6) > k_{ai}^{(1)}(c\text{-}C_4F_8)$, thus indicating that homomolecular CH_3I dimerization (i.e., Eq. (6.4)) is more favorable than heteromolecular CH_3I/SF_6 dimerization which, in turn, is more favorable than heteromolecular $CH_3I/c\text{-}C_4F_8$ dimerization. The associative ionization rate must depend upon the polarizability of the ground-state molecule in the dimer pair (cf. Chapter 3.C.iv), albeit in ways that are sensitively dependent upon the nature of the potentials chosen to model these interactions. Therefore, if we assume that the dominant interactions are ion-induced dipole interactions [113], then $k_{ai}^{(1,2)}$ should be directly proportional to the polarizability of the ground-state molecule in the dimer pair. Fig. 6.24b shows that, when $k_{ai}^{(1,2)}$ is normalized to the ground-state polarizability in the manner described above, this does in fact hold for CH_3I and for CH_3I/SF_6, but not for $CH_3I/c\text{-}C_4F_8$. (In Fig. 6.24b, we have normalized to the polarizabilities given in Table 6.11.) Thus, dimerization involving c-C_4F_8 is not as efficient as dimerization involving the more spherical molecules CH_3I and SF_6.

Finally, under the assumption that the perturber-stabilized associative ionization rate constants are also linearly dependent on the ground-state polarizability of the perturber, $k_{ai}'^{(2)}$ should collapse to a single linear correlation for all perturbers. That this is the case for

CH_3I/P (P = Ar, CF_4, c-C_4F_8, CO_2, N_2 and SF_6) is shown in Fig. 6.24c (where the $k_{si}^{\prime(n)}$ values have been normalized to the polarizabilities given in Table 6.11).

F. Summary of Results

In this Chapter, subthreshold photoionization results for CH_3I, C_2H_5I and C_6H_6 perturbed by Ar, CF_4, c-C_4F_8, CO_2, N_2 and SF_6 for variations in temperature, dopant number density ρ_D and perturber number density ρ_P have been presented. The electron scattering lengths for the fluorinated gases CF_4, c-C_4F_8 and SF_6 were evaluated and shown to agree with the zero-kinetic-energy electron scattering lengths obtained from the perturber-induced energy shifts of the absorption and autoionization structure of the same dopants, thereby confirming that the subthreshold photocurrent arises from ionization of high-n Rydberg states.

Temperature studies showed that the subthreshold structure observed in these dopant/perturber systems did not arise from hot-band or rotational autoionization. The collisional transfer of translation energy was shown to follow a Boltzmann distribution, and to contribute only to the rising exponential background. Moreover, this collisional ionization was shown to be independent of the nature of the perturber, thereby demonstrating the absence of collisional transfer of vibrational or rotational energy from a molecular perturber to the excited-state dopant. Furthermore, photochemical rearrangement was ruled out as a possible mechanism on the basis of energetics.

By varying both ρ_D and ρ_P, pathway 1 (i.e., Eqs. (6.1), (6.2) and (6.10)), which depends upon direct dopant/perturber interactions, was shown to be sufficient to explain the origin and behavior of subthreshold photoionization in both C_2H_5I/SF_6 and C_6H_6/SF_6. The present analysis also concluded that the subthreshold photocurrent in CH_3I/P (P = Ar, CF_4, CO_2, N_2) can be modeled solely within the confines of pathway 2 (i.e., Eqs. (6.3) - (6.5) and (6.11)).

However, the subthreshold photoionization in CH_3I/P (P = c-C_4F_8, SF_6) proceeds through both pathways 1 and 2 simultaneously (i.e., Eqs. (6.1) - (6.5) and (6.12)).

By systematically varying ρ_D and ρ_P, the effective rate constants for the various processes leading to subthreshold photoionization were determined. The effective rate constant for electron attachment to CH_3I (i.e., $k_{ea}^{(2)}$) obtained from pure CH_3I was shown to agree well with that obtained from CH_3I/Ar and CH_3I/CF_4. Moreover, the CH_3I homomolecular dimerization effective rate constant (i.e., $k_{ai}^{(2)}$) obtained from pure CH_3I agrees with the same constant determined for CH_3I/Ar, CH_3I/CF_4, CH_3I/c-C_4F_8 and CH_3I/SF_6, thus demonstrating the consistency of these analyses.

It was shown that $k_{ea}^{(1,2)}$, $k_{ai}^{(1,2)}$ and $k_{ai}^{\prime(2)}$ scale in a simple fashion with respect to the principal quantum number n of the dopant Rydberg state. One can conclude, therefore, that the mechanisms of (saturated) electron attachment and associative ionization are sufficient to explain the behavior of the subthreshold photocurrent for all of the D/P systems presented here. Furthermore, for the dopant CH_3I, the variation in the effective rate constants for electron attachment $k_{ea}^{(1,2)}$ to CH_3I, to c-C_4F_8 and to SF_6 has been shown to scale linearly with electron affinity. The variation in the associative ionization rate constant $k_{ai}^{(1,2)}$ has been shown to be directly proportional to the polarizability of the ground-state molecule in the $CH_3I\cdots X$ dimer pair (X = CH_3I, SF_6). However, a comparison of $k_{ai}^{(1,2)}$ for CH_3I, c-C_4F_8 and SF_6 also showed that heteromolecular dimerization of CH_3I to c-C_4F_8 is less efficient than dimerization either to CH_3I or to SF_6. Finally, the perturber-stabilized associative ionization rate constant $k_{ai}^{\prime(2)}$ for CH_3I/P (P = Ar, CF_4, c-C_4F_8, CO_2, N_2, SF_6) has been shown to be linearly dependent on the ground-state polarizability of the perturber.

Chapter 7. Conclusion

In this Dissertation, perturber effects on the photoionization spectra of various dopants were used to probe the nature of dopant/perturber interactions. The presentation of these results began, in Chapter 2, with a brief introduction to Rydberg states, including the methods used to generate and study these highly excited states. Some of the various types of perturber effects on dopant Rydberg states were then reviewed in Chapter 3 in order to lay a foundation for the results presented in Chapters 5 and 6. Chapter 4 gave a description of the experimental equipment and procedures used throughout this work. In Chapter 5, the perturber-induced energy shifts of high-n dopant Rydberg states, determined from the absorption and autoionization spectra of the dopant, were used to evaluate the zero-kinetic-energy electron scattering lengths of CF_4, c-C_4F_8 and SF_6. To the best of our knowledge, these measurements represent the first experimental determination of the zero-kinetic-energy electron scattering lengths of CF_4 and c-C_4F_8, and the first determination of the zero-kinetic-energy electron scattering length of SF_6 using high-n dopant Rydberg states. The investigation of dopant/perturber interactions continued in Chapter 6 with the study of the subthreshold photoionization of various dopants as a function of temperature and number density (of the dopant and the perturber).

During the process of investigating the density effects on the subthreshold photoionization spectra of CH_3I, C_2H_5I and C_6H_6 in various perturbers (Ar, CF_4, c-C_4F_8, CO_2, N_2 and SF_6), the perturber-induced energy shifts of the subthreshold structure was used to evaluate the zero-kinetic-energy electron scattering lengths for the fluorinated gases CF_4, c-C_4F_8, and SF_6 in Chapter 6.B. Since the zero-kinetic-energy electron scattering lengths obtained from the subthreshold spectra agree well with those obtained in Chapter 5 from the

absorption and autoionization spectra, one can conclude that the observed subthreshold photoionization structure arises from the ionization of high-*n* Rydberg states.

Therefore, the main result of this work was to use the temperature dependent and density dependent behavior of subthreshold photocurrent, observed in various dopant/perturber systems, to probe the mechanisms leading to subthreshold photoionization. The dopants chosen for this study were CH_3I, C_2H_5I and C_6H_6 while the perturbers were Ar, CF_4, *c*-C_4F_8, CO_2, N_2 and SF_6. From the temperature study of this subthreshold structure, hot-band autoionization and rotational autoionization were ruled out as possible mechanisms (cf. Chapter 6.C) leading to subthreshold photoionization. Collisional transfer of rotational and vibrational energy from the perturber to the excited state dopant was dismissed because of the similarity of the subthreshold structure for both atomic and molecular perturbers. Moreover, photochemical rearrangement was excluded on the basis of energetics (cf. Chapter 6.D). Therefore, we proposed two possible pathways which could lead to subthreshold photoionization (cf. Chapter 6.E). Although both of these pathways invoke the processes of (saturated) electron attachment and associative ionization, the nature of the dopant/perturber interactions was different for each of the pathways.

The first pathway (i.e., Eqs. (6.1) - (6.2)) invoked direct dopant/perturber interactions in the form of electron attachment to the perturber and heteromolecular dopant/perturber dimerization. The second pathway (i.e., Eqs. (6.3) - (6.5)), on the other hand, invoked only indirect dopant/perturber interactions via perturber-stabilized homomolecular dopant dimerization. Subthreshold photoionization in C_2H_5I and C_6H_6 was shown to proceed only through pathway 1, whereas CH_3I was shown to be able to access both pathways 1 and 2. From these results, several qualitative observations were made:

(1) For a dopant/perturber system to be able to access pathway 1, the *perturber* must possess a large electron affinity and a large ground-state polarizability. Furthermore, the dopant and perturber must be able to form heteromolecular dimers in the static gas-phase system.

(2) The second pathway requires that the *dopant* have a large electron affinity and a large ground-state polarizability. Moreover, the dopant must be able to form homomolecular dimers in the static gas-phase system.

By systematically varying the dopant and perturber number densities, the effective rate constants for electron attachment and associative ionization were determined. The effective rate constant for electron attachment, $k_{ea}^{(1,2)}$, was shown to be inversely proportional to the velocity of the Rydberg electron (i.e., $k_{ea}^{(1,2)}$ was shown to scale linearly with n) and directly proportional to the electron affinity of the neutral ground-state molecule involved in the electron attachment process. Therefore, one can conclude that the stability of the molecular anion formed during electron attachment plays an important role in the probability of this process occurring. The effective rate constants for associative ionization, $k_{ai}^{(1,2)}$ and $k_{ai}^{\prime(2)}$, were shown to be proportional to the polarizability of the dopant Rydberg state (i.e., $k_{ai}^{(1,2)}$ and $k_{ai}^{\prime(2)}$ were shown to scale linearly with n^7). Moreover, the effective rate constant for perturber-stabilized associative ionization, $k_{ai}^{\prime(2)}$, was shown to be linearly dependent on the ground-state polarizability of the perturber. However, comparison of the associative ionization effective rate constant, $k_{ai}^{(1,2)}$, for CH_3I, c-C_4F_8 and SF_6 showed that heteromolecular dimerization of CH_3I with c-C_4F_8 is less efficient than dimerization either with CH_3I or with SF_6.

In order to probe further the applicability of pathways 1 and 2 as models of subthreshold photoionization, different dopants and perturbers should be considered. With this in mind, an attempt to measure subthreshold photoionization spectra of HI was made. However, HI

caused serious corrosion problems in our vacuum system which led to our discontinuation of these measurements. Initial results, however, showed that HI exhibited rich subthreshold photoionization structure which was quadratically dependent on the HI number density, indicating that pathway 2 is accessible for this system.

Examining the variation of the effective rate constant for electron attachment as a function of the perturber electron affinity, which might eventually lead to a new method for probing electron affinities, will require additional studies with different perturbers that can access pathway 1. Likewise, examination of the variation in the associative ionization rate constant, which might later be used to probe the type of interaction potential needed to model various dopant/perturber systems, will require additional studies with different dopants possessing different molecular symmetries, polarizabilities and electron affinities.

In conclusion, this work has demonstrated that the mechanisms of interaction between dopants and perturbers can be sensitively probed using number density effects on subthreshold photoionization structure. The excited-state mechanisms of electron attachment and associative ionization were shown to lead to subthreshold photoionization in the dopant/perturber systems examined here. Moreover, variations in subthreshold peak areas, as functions of dopant and perturber number density, provided a powerful means to determine effective rate constants for electron attachment and associative ionization. Finally, these effective rate constants were assessed with respect to dependence upon the principal quantum number of the dopant excited state, the ground-state polarizability of the perturber (or dopant) and the electron affinity of the perturber (or dopant).

References

1. G. H. Herzberg, *Molecular Spectra and Molecular Structure Vol. I and II* (Van Nostrand, New York, 1950, 1966).

2. M. B. Robin, *Higher Excited States of Polyatomic Molecules Vol. I, II and III* (Academic Press, 1974, 1975, 1985).

3. R. F. Stebbings and F. B. Dunning, editors, *Rydberg States of Atoms and Molecules* (Cambridge Univ. Press, Cambridge, 1983).

4. S. P. McGlynn, G. L. Findley and R. H. Huebner, editors, *Photophysics and Photochemistry in the Vacuum Ultraviolet* (D. Reidel, Dordrecht, 1985).

5. I. I. Sobel'man, L. A. Vainshtein and E. A. Yukov, *Excitation of Atoms and Broadening of Spectral Lines* (Springer-Verlag, Berlin, 1981).

6. A. M. Köhler, *Density Effects on Rydberg States and Ionization Energies of Molecules*, Ph.D. dissertation, Universität Hamburg, 1987.

7. J. Meyer, *Elektronische Eigenschaften dotierter Gase und Flüssigkeiten* (Electronic Properties of Dense Gases and Liquids), Ph.D. dissertation, Universität Hamburg, 1992.

8. C. Sándorfy, editor, *The Role of Rydberg States in Spectroscopy and Photochemistry* (Kluwer Academic Pub, Dordrecht, 1999).

9. T. F. Gallagher, *Rydberg Atoms* (Cambridge Univ. Press, Cambridge, 1994).

10. E. W. Schlag, *ZEKE Spectroscopy* (Cambridge Univ.Press, Cambridge, 1998).

11. E. Fermi, "Sopra lo spostamento per pressione delle righe elevate delle serie spettrali (Concerning the shift of the high lines of spectral series due to pressure effects)," Nuovo Cimento **11**, 157 (1934).

12. V. A. Alekseev and I. I. Sobel'man, "A spectroscopic method for the investigation of elastic scattering of slow electrons," Zh. Eksp. Teor. Fiz. **49**, 1274 (1965) [Sov. Phys. JETP **22**, 882 (1966)].

13. A. K. Al-Omari, R. Reininger and D. L. Huber, "Polarization energy distribution for impurity molecules in dense gases," J. Chem. Phys. **109**, 7663 (1998).

14. C. M. Evans, J. D. Scott, F. H. Watson and G. L. Findley, "Photoionization studies of C_2H_5I and C_6H_6 perturbed by Ar and SF_6," Chem. Phys. **260**, 225 (2000).

15. C. M. Evans, E. Morikawa and G. L. Findley, "Photoionization spectra of CH_3I and C_2H_5I perturbed by CF_4 and c-C_4F_8: Electron scattering in halocarbon gases," J. Phys. B, submitted.

16. C. M. Evans, R. Reininger and G. L. Findley, "Photoionization spectra of CH_3I perturbed by SF_6: Electron scattering in SF_6 gas," Chem. Phys. Lett. **297**, 127 (1998).

17. C. M. Evans, R. Reininger and G. L. Findley, "Subthreshold photoionization spectra of CH_3I perturbed by SF_6," Chem. Phys. **241**, 239 (1999).

18. C. M. Evans, R. Reininger and G. L. Findley, "Subthreshold photoionization of CH_3I in Ar, N_2 and CO_2," Chem. Phys. Lett. **322**, 465 (2000).

19. C. M. Evans and G. L. Findley, "Pressure studies of subthreshold photoionization: CH_3I perturbed by CF_4 and c-C_4F_8," Chem. Phys. Lett., in press.

20. C. M. Evans, E. Morikawa and G. L. Findley, "Pressure studies of subthreshold photoionization: CH_3I, C_2H_5I and C_6H_6 perturbed by Ar and SF_6," Chem. Phys., in press.

21. I. T. Steinberger, U. Asaf, G. Ascarelli, R. Reininger, G. Reisfeld and M. Reshotko, "Extrinsic photoconduction and Rydberg states due to a methyl iodide impurity in xenon," Phys. Rev. A **42**, 3135 (1990).

22. H. E. White, *Introduction to Atomic Spectra* (McGraw-Hill, New York, 1934).

23. G. D. Liveing and J. Dewar, "On the spectra of sodium and potassium," Proc. Roy. Soc. Lond. **29**, 398 (1879).

24. W. N. Hartley, "On Homologous Spectra," J. Chem. Soc. **43**, 390 (1883).

25. J. R. Rydberg, "On the structure of the line-spectra of the chemical elements," Phil. Mag. 5th Ser. **29**, 331 (1890).

26. A. R. P. Rau, "Elements of quantum defect theory. I. Introduction and formalism," in *Photophysics and Photochemistry in the Vacuum Ultraviolet*, S. P. McGlynn, G. L. Findley and R. H. Huebner, editors (D. Reidel, Dordrecht, 1985).

27. K. T. Lu, "Elements of quantum defect theory. II. A unified theory of Rydberg and autoionizing states," in *Photophysics and Photochemistry in the Vacuum Ultraviolet*, S. P. McGlynn, G. L. Findley and R. H. Huebner, editors (D. Reidel, Dordrecht, 1985).

28. C. H. Greene, "Elements of quantum defect theory. III. Diatomic molecules," in *Photophysics and Photochemistry in the Vacuum Ultraviolet*, S. P. McGlynn, G. L. Findley and R. H. Huebner, editors (D. Reidel, Dordrecht, 1985).

29. R. S. Freund, "High-Rydberg molecules," in *Rydberg States of Atoms and Molecules*, R. F. Stebbings and F. B. Dunning, editors (Cambridge Univ. Press, Cambridge, 1983).

30. S. Leach, "Superexcited and ionic state relaxation processes in vacuum ultraviolet excited polyatomic molecules," in *Photophysics and Photochemistry in the Vacuum Ultraviolet*, S. P. McGlynn, G. L. Findley and R. H. Huebner, editors (D. Reidel, Dordrecht, 1985).

31. H. Lefebvre-Brion, "Lifetimes of Rydberg states in small molecules," in *The Role of Rydberg States in Spectroscopy and Photochemistry*, C. Sándorfy, editor (Kluwer Academic Pub, Dordrecht, 1999).

32. G. L. Findley, J. A. Wilder, P. Hochmann and S. P. McGlynn, "Photophysics of highly-excited states," in *Photophysics and Photochemistry in the Vacuum Ultraviolet*, S. P. McGlynn, G. L. Findley and R. H. Huebner, editors (D. Reidel, Dordrecht, 1985).

33. D. M. Ortalano, *Coulomb States in Atoms and Solids*, Ph.D. dissertation, Louisiana State University, 1988.

34. J. D. Scott, "Perturbation spectroscopy," in *Photophysics and Photochemistry in the Vacuum Ultraviolet*, S. P. McGlynn, G. L. Findley and R. H. Huebner, editors (D. Reidel, Dordrecht, 1985).

35. D. D. Altenloh and B. R. Russell, "Electric field studies in the vacuum ultraviolet," in *Photophysics and Photochemistry in the Vacuum Ultraviolet*, S. P. McGlynn, G. L. Findley and R. H. Huebner, editors (D. Reidel, Dordrecht, 1985).

36. D. Kleppner, M. G. Littman and M. L. Zimmerman, "Rydberg atoms in strong fields," in *Rydberg States of Atoms and Molecules*, R. F. Stebbings and F. B. Dunning, editors (Cambridge Univ. Press, Cambridge, 1983).

37. S. Grimme and S. D. Peyerimhof, "Theoretical study of circular dichroism spectra in the vacuum ultraviolet," in *The Role of Rydberg States in Spectroscopy and Photochemistry*, C. Sándorfy, editor (Kluwer Academic Pub, Dordrecht, 1999).

38. A. K. Al-Omari, *Field ionization as a technique to determine electronic properties of fluids*, Ph.D. dissertation, University of Wisconsin – Madison, 1996.

39. D. Gauyacq, M. Raoult and N. Shafizadeh, "Dynamics of a Rydberg molecule in a n external magnetic field," in *The Role of Rydberg States in Spectroscopy and Photochemistry*, C. Sándorfy, editor (Kluwer Academic Pub, Dordrecht, 1999).

40. A. Gedanken, "Circular dichroism and magnetic circular dichroism studies int eh vacuum ultraviolet," in *Photophysics and Photochemistry in the Vacuum Ultraviolet*, S. P. McGlynn, G. L. Findley and R. H. Huebner, editors (D. Reidel, Dordrecht, 1985).

41. S. P. McGlynn, P. Brint, J. D. Scott and K. Rupnik, "Magnetic dichroism in the vacuum ultraviolet," in *The Role of Rydberg States in Spectroscopy and Photochemistry*, C. Sándorfy, editor (Kluwer Academic Pub, Dordrecht, 1999).

42. J. O. Hireschfelder, C. F. Curtiss and R. B. Bird, *Molecular Theory of Gases and Liquids* (Wiley, New York, 1954).

43. G. Baum, M. S. Lubell and W. Raith, "Measurement of spin-orbit perturbation in the P-state continuum of heavy alkali metal atoms. Potassium, rubidium and cesium," Phys. Rev. A **5**, 1073 (1972).

44. R. J. Exton, "Resonance broadening," J. Quant. Spectrosc. Radiat. Transfer **16**, 309 (1975).

45. P. M. Koch, "Rydberg studies using fast beams," in *Rydberg States of Atoms and Molecules*, R. F. Stebbings and F. B. Dunning, editors (Cambridge Univ. Press, Cambridge, 1983).

46. J. M. Raimond, M. Gross, C. Fabre, S. Haroche and H. H. Stroke, "Laser measurment of intensity ratio anomalies in principal series doublets of cesium Rydberg states: does the D1 line vanish?," J. Phys. B. **11**, L765 (1978).

47. W. C. Price, "The absorption of the halogen acids in the vacuum ultra-violet," Proc. R. Soc. Lond. Ser. A **167**, 216 (1938).

48. J. H. D. Eland and J. Berkowitz, "Photoionization mass spectrometry of HI and DI at high resolution," J. Chem. Phys. **67**, 5034 (1977).

49. H. T. Wang, W. S. Felps, G. L. Findley, A. R. P. Rau and S. P. McGlynn, "Molecular Rydberg states. XI. Quantum defect analogies between molecules and rare gases," J. Chem. Phys. **67**, 3940 (1977).

50. W. C. Price, "The far ultraviolet absorption spectra and ionization potentials of the alkyl halides, Part 1," J. Chem. Phys. **4**, 539 (1936).

51. P. Hochmann, P. H. Templet, H. -t. Wang and S. P. McGlynn, "Molecular Rydberg transitions. I. Low-energy Rydberg transitions in methyl halides," J. Chem. Phys. **62**, 2588 (1975).

52. S. Felps, P. Hochmann, P. Brint and S. P. McGlynn, "Molecular Rydberg transitions: The lowest-energy Rydberg transitions of *s*-type in CH_3X and CD_3X, X = Cl, Br and I," J. Molec. Spectr. **59**, 355 (1976).

53. T. N. Olney, G. Cooper and C. E. Brion, "Quantitative studies of the photoabsorption (4.5 – 488 eV) and photoionization (9 – 59.5 eV) of methyl iodide using dipole electron impact techniques," Chem. Phys. **232**, 211 (1998).

54. R. A. Boschi and D. R. Salahub, "The far ultra-violet spectra of some 1-iodoalkanes," Molec. Phys. **24**, 289 (1972).

55. W. C. Price, "The far ultraviolet absorption spectra and ionization potentials of the alkyl halides. Part II," J. Chem. Phys. **4**, 547 (1936).

56. M. A. Baig, J. P. Connerade and J. Hormes, "Autoionisation resonance in the photoabsorption spectrum of C_2H_5I," J. Phys. B: At. Mol. Phys. **19**, L343 (1986).

57. K. Wittle and S. P. McGlynn, "The orbital concept in molecular spectroscopy," Chem. Rev. **77**, 745 (1977).

58. E. Amaldi and E. Segrè, "Effetto della pressione sui termini elevati degli alcalini (Effect of pressure on the high terms of alkaline metals)," Nuovo Cimento **11**, 145 (1934).

59. T. Z. Ny and S. Y. Ch'en, "The displacement of principal series lines of rubidium by the addition of rare gases," Phys. Rev. **51**, 567 (1937).

60. C. Füchtbauer and W. V. Heesen, "Verbreiterung und Verschiebung von mittleren und höheren Kaliumserienlinien durch Helium von hohem Druck (Broadening and shift of middle and higher potassium series-lines by high pressure helium)," Z. Phys. **113**, 323 (1939).

61. C. Füchtbauer and G. Hansler, "Dichteabhängigkeit der Verschiebung hoher Alkaliserienlinien durch Fremdgase (Density-dependent shift of high alkali series-lines due to foreign gases)," Phys. Z. **41**, 555 (1940).

62. O. B. Firsov, "Effect of a foreign gas on the absorption spectrum near the limit of the series. I," Zh. Eksp. Teor. Fiz. **21**, 627 (1951); "Effect of a foreign gas on the absorption spectrum near the limit of the series. II," *ibid.* **21**, 634 (1951).

63. A. M. Köhler, R. Reininger, V. Saile and G. L. Findley, "Density effects on high-*n* molecular Rydberg states: CH_3I in He, Ne, Ar and Kr," Phys. Rev. A **35**, 79 (1987).

64. T. F. O'Malley, "Extrapolation of electron-rare gas atom cross-sections to zero energy," Phys. Rev. **130**, 1020 (1963).

65. A. C. Newell and R. D. Baird, "Absolute determination of refractive indices of gases at 47.7 Gigahertz," J. Appl. Phys. **36**, 3751 (1965).

66. R. H. Orcutt and R. H. Cole, "Dielectric constants of imperfect gases. III. Atomic gases, hydrogen and nitrogen," J. Chem. Phys. **46**, 697 (1967).

67. V. A. Alekseev and I. I. Sobel'man, "A spectroscopic method for the investigation of elastic scattering of slow electrons," Zh. Eksp. Teor. Fiz. **49**, 1274 (1965) [Sov. Phys. JETP **22**, 882 (1966)].

68. V. Weisskopf, "Zur Theorie der Kopplungsbreite und der Stoßdämpfung (On the theory of coupling width and impact damping)", Z. Phys. **75**, 287; "Zur Theorie der Kopplungsbreite (On the theory of coupling width)," Z. Phys. **77**, 398 (1932).

69. V. Weisskopf, "Die Breite der Spektrallinien in Gasen (The width of spectral lines in gases)," Phys. Z. **34**, 1 (1933).

70. A. M. Köhler, V. Saile, R. Reininger and G. L. Findley, "Sudden and adiabatic polarization effects in doped rare gases," Phys. Rev. Lett. **60**, 2727 (1988).

71. J. Meyer, R. Reininger and U. Asaf, "Spectral shift of autoionizing high-*n* Rydberg states of CH_3I in dense Ar: a photoionization study," Chem. Phys. Lett. **173**, 384 (1990).

72. J. Meyer, R. Reininger, U. Asaf and I. T. Steinberger, "Autoionization spectra of CH_3I in dense gaseous methane, ethane and propane observed by photoconduction," J. Chem. Phys. **94**, 1820 (1991).

73. U. Asaf, I. T. Steinberger, J. Meyer and R. Reininger, "Electron scattering in dense CO_2 gas: Photoionization spectra of CH_3I perturbed by CO_2," J. Chem. Phys. **95**, 4070 (1991).

74. U. Asaf, W. S. Felps, K. Rupnik, S. P. McGlynn and G. Ascarelli, "Density effects on high-*n* Rydberg states: CH_3I and C_6H_6 in H_2 and Ar," J. Chem. Phys. **91**, 5170 (1989).

75. U. Asaf, J. Meyer, R. Reininger and I. T. Steinberger, "High Rydberg states of methyl iodide perturbed by nitrogen: A mutual cancellation of shift terms," J. Chem. Phys. **96**, 7885 (1992).

76. A. K. Al-Omari, R. Reininger and D. L. Huber, "Temperature effect on the ionization potential line-shape of NO doped into dense gaseous argon," Chem. Phys. Lett. **273**, 402 (1997).

77. A. K. Al-Omari, R. Reininger and D. L. Huber, "Polarization energy distribution of a positive ion in liquid argon," Phys. Rev. Lett. **74**, 820 (1995).

78. H. Margenau, "Theory of pressure effects of foreign gases on spectral lines," Phys. Rev. **48**, 755 (1935).

79. A. Jablonski, "General theory of pressure broadening of spectral lines," Phys. Rev. **68**, 78 (1945).

80. M. B. Robin and N. A. Kuebler, "Pressure effects on vacuum ultraviolet spectra," J. Molec. Spectr. **33**, 274 (1970).

81. H. Margenau and W. W. Watson, "Pressure effects on spectral lines," Rev. Mod. Phys. **8**, 22 (1936).

82. S. -Y. Ch'en and M. Takeo, "Broadening and shift of spectral lines due to the presence of foreign gases," Rev. Mod. Phys. **29**, 20 (1957).

83. A. Royer, "Shift, width and asymmetry of pressure-broadened spectral lines at intermediate densities," Phys. Rev. A **22**, 1625 (1980).

84. N. Allard and J. Kielkopf, "The effect of neutral nonresonant collisions on atomic spectral lines," Rev. Mod. Phys. **54**, 1103 (1982).

85. J. Meyer, U. Asaf and R. Reininger, "Vibrational autoionization of hot bands in methyl iodide," Phys. Rev. A **46**, 1673 (1992).

86. M. Matsuzawa, "Theoretical studies of collisions of Rydberg atoms with molecules," in *Rydberg States of Atoms and Molecules*, R. F. Stebbings and F. B. Dunning, editors (Cambridge Univ. Press, Cambridge, 1983).

87. V. S. Ivanov and F. I. Vilesov, "Bimolecular ionization of excited CH_3I molecules," Opt. Spectrosc. **36**, 602 (1974) [Opt. Spektrosk. **36**, 1023 (1974)].

88. V. S. Ivanov and F. I. Vilesov, "Near-threshold photoionization processes in methyl halides," Opt. Spectrosc. **39**, 487 (1975) [Opt. Spektrosk. **39**, 857 (1975)].

89. R. S. Berry and S. E. Nielsen, "Dynamic coupling phenomena in molecular excited states. I. General formation and vibronic coupling hydrogen," Phys. Rev. A **1**, 383 (1970); "Dynamic coupling phenomena in molecular excited states. II. Autoionization and predissociation in H_2, HD and D_2," Phys. Rev. A **1**, 395 (1970).

90. J. Berkowitz and J. P. Greene, "Vibrational autoionization in PF_3: Doing violence to the propensity rule," J. Chem. Phys. **81**, 4328 (1994).

91. M. Broyer, J. Chevaleyre, G. Delacretaz, S. Martin and L. Wöste, "K_2 Rydberg state analysis by two- and three-photon ionization," Chem. Phys. Lett. **99**, 206 (1983).

92. P. J. Miller, W. A. Chupka and J. H. D. Elland, "Vibrationally autoionizing Rydberg states of NH_3," Chem. Phys. **122**, 395 (1988).

93. J. Berkowitz and B. Ruscic, "Electric field effects in the photoionization of N_2 near threshold," J. Chem. Phys. **93**, 1741 (1990).

94. F. X. Campos, Y. Jiang and E. R. Grant, "Triple-resonance spectroscopy of the higher excited states of NO_2. III. $|\Delta v| > 1$ autoionization and vibronic coupling," J. Chem. Phys. **94**, 5897 (1991).

95. B. Ruscic and J. Berkowitz, "Photoionization of HBr and DBr near threshold," J. Chem. Phys. **93**, 1747 (1990).

96. F. B. Dunnings and R. F. Stebbings, "Thermal-energy collisions of Rydberg atoms with molecules," in *Rydberg States of Atoms and Molecules*, R. F. Stebbings and F. B. Dunning, editors (Cambridge Univ. Press, Cambridge, 1983).

97. G. W. Foltz, C. J. Latimer, G. J. Hildebrandt, F. G. Kellert, K. A. Smith, W. B. West, F. B. Dunning and R. F. Stebbings, "Ionization of xenon atoms in high Rydberg states by collisions with molecules," J. Chem. Phys. **67**, 1352 (1977).

98. G. B. Zollars, C. W. Walter, F. Lu, C. B. Johnson, K. A. Smith and F. B. Dunning, "Ionization of K (*n*d)–SF_6 and K (*n*d)–CCl_4 collisions at intermediate *n*," J. Chem. Phys. **84**, 5589 (1986).

99. I. M. Beterov, F. L. Vosilenko, I. I. Riabstev, B. M. Smirnov and N. V. Fateyev, "Collisional chemionization of highly excited sodium atoms with electronegative molecular sulfur hexafluoride," Z. Phys. D **7**, 55 (1987).

100. Z. Zheng, K. A. Smith and F. B. Dunning, "Postattachment interactions in K (*n*d)–SF_6 collisions at intermediate *n*," J. Chem. Phys. **89**, 6295 (1988).

101. K. Harth, M. -W. Ruf and H. Hotop, "Electron trasfer from laser excited Rydberg atoms to molecules. Absolute rate constants at low and intermediate principal quantum numbers," Z. Phys. D **14**, 149 (1989).

102. I. Dimicoli and R. Botter, "Ionizing reaction cross-sections in the collision of argon atoms in high Rydberg states with various molecules," J. Chem. Phys. **74**, 2346 (1981); "Ion-pair formation in the collision of high Rydberg argon atoms with SF_6 and C_6F_6 and negative ion lifetimes," J. Chem. Phys. **74**, 2355 (1981).

103. W. T. Naff, C. D. Cooper and R. N. Compton, "Transient negative-ion states in alicyclic and aromatic fluorocarbon molecules," J. Chem. Phys. **49**, 2784 (1968).

104. A. Rosa and I. Szamrej, "Thermal electron capture in the mixtures of halocarbons and environmental gases," J. Phys. Chem. A **104**, 67 (2000).

105. J. A. Hornbeck and J. P. Molnar, "Mass spectrometric studies of molecular ions in the noble gases," Phys. Rev. A **84**, 621 (1951).

106. P. M. Dehmer and E. D. Poliakoff, "Photoionization of the argon dimer," Chem. Phys. Lett. **77**, 326 (1981).

107. P. M. Dehmer, "Photoionization of Ar_2 at high resolutions," J. Chem. Phys. **76**, 1263 (1982).

108. S. T. Pratt and P. M. Dehmer, "Photoionization of the krypton (Kr_2) dimer," Chem. Phys. Lett. **87**, 533 (1982).

109. P. M. Dehmer and S. T. Pratt, "Systematics of Rydberg structure in the spectra of the rare gas dimers between the $^2P_{3/2}$ and $^2P_{1/2}$ fine structure thresholds," J. Chem. Phys. **75**, 5265 (1981).

110. S. T. Pratt and P. M. Dehmer, "Photoionization of the neon-rare gas dimers neon-argon (NeAr), neon-krypton (NeKr), and neon-xenon (NeXe)," J. Chem. Phys. **76**, 3433 (1982).

111. P. M. Dehmer and S. T. Pratt, "Photoionization of argon-krypton, argon-xenon, and krypton-xenon and bond dissociation energies of the rare gas dimers," J. Chem. Phys. **77**, 4804 (1982).

112. D. J. Trevor, *Photoelectron Photoion Molecular Beam Spectroscopy*, Ph.D. dissertation, University of California, Berkeley, 1980.

113. P. M. Dehmer and S. T. Pratt, "VUV spectroscopy of rare-gas van der Waals dimers," in *Photophysics and Photochemistry in the Vacuum Ultraviolet*, S. P. McGlynn, G. L. Findley and R. H. Huebner, editors (D. Reidel, Dordrecht, 1985).

114. C. Higgs, K. A. Smith, F. B. Dunning and R. F. Stebbings, "A study on ℓ-changing in atomic xenon (nf)–neutral collisions at thermal energies," J. Chem. Phys. **75**, 745 (1981).

115. F. G. Kellert, K. A. Smith, R. D. Rundel, F. B. Dunning and R. F. Stebbings, "Collisions of xenon (nf) Rydberg atoms with ammonia," J. Chem. Phys. **72**, 3179 (1980).

116. M. Seya, "A new mounting of concave grating suitable for a spectrometer," Sci. Light **2**, 8 (1952). T. Namioka, "Theory of the concave grating. III. Seya-Namioka monochromator," J. Opt. Soc. Am. **49**, 951 (1959). U. Gerhardt, E. Diet and N. Rehfeld, "Integrated optical system for the vacuum UV region," in *3rd International Conference on Vacuum Radiation Physics* (Tokyo, 1971) p. 1 – 2.

117. *An Invitation to See the Light*, University of Wisconsin Synchrotron Radiation Center, or www.src.wisc.edu/facilities/beamlines/list/083.html.

118. N. Knoblauch, A. Strobel, I. Fischer and V. E. Bondybey, "Two-photon ionization and dissociation of ethyl iodide," J. Chem. Phys. **103**, 5417 (1995).

119. R. L. Whetten, S. G. Grubb, C. E. Otis, A. C. Albrecht and E. R. Grant, "Higher excited states of benzene: Polarized ultraviolet two-photon absorption spectroscopy," J. Chem. Phys. **82**, 1115 (1985)

120. S. G. Grubb, C. E. Otis, R. L. Whetten, E. R. Grant and A. C. Albrecht, "Higher excited states of benzene: Symmetry assignments of six gerade Rydberg series by four-photon absorption spectroscopy," J. Chem. Phys. **82**, 1135 (1985).

121. M. T. do N. Varella, A. P. P. Natalense, M. H. F. Bettega, and M. A. P. Lima, "Low-energy electron scattering by CF_4, CCl_4, $SiCl_4$, $SiBr_4$ and SiI_4," Phys. Rev. A **60**, 3684 (1999).

122. R. K. Jones, "Absolute total cross sections for the scattering of low energy electrons by CCl_4, CCl_3F, CCl_2F_2, $CClF_3$, and CF_4," J. Chem. Phys. **84**, 813 (1986).

123. L. G. Christophorou, J. K. Olthoff and M. V. V. S. Rao, "Electron interactions with CF_4," J. Phys. Chem. Ref. Data **25**, 1341 (1996).

124. A. A. Christodoulides, L. G. Christophorou, R. Y. Pai and C. M. Tung, "Electron attachment to perfluorocarbon compounds. I. *c*-C_4F_6, 2-C_4F_6, 1,3-C_4F_6, *c*-C_4F_8 and 2-C_4F_8," J. Chem. Phys. **70**, 1156 (1979).

125. T. M. Miller, A. E. S. Miller, J. F. Paulson and X. Liu, "Thermal electron attachment to SF_4 and SF_6," J. Chem. Phys. **100**, 8841 (1994).

126. F. A. Gianturco, R. R. Lucchese, and N. Sanna, "On the scattering of low energy electrons by sulfur hexafluoride," J. Chem. Phys. 102, 5743 (1995).

127. G. P. Karwasz, R. S. Brusa, A. Piazza and A. Zecca, "Total cross sections for electron scattering on chloromethanes: formulation of the additivity rule," Phys. Rev. A **59**, 1341 (1999).

128. Y. H. Jiang, J. F. Sun and L. Wan, "Total cross sections for electron scattering by polyatomic molecules at 10 – 1000 eV: H_2S, SiH_4, CH_4, CF_4, CCl_4, SF_6, C_2H_4, CCl_3F, $CClF_3$, and CCl_2F_2," Phys. Rev. A **52**, 398 (1995).

129. A. V. Phelps and R. J. Van Brunt, "Electron transport, ionization, attachment, and dissociation coefficients in sulfur hexafluoride and its mixtures," J. Appl. Phys. 64, 4269 (1988).

130. H. -X. Wan, J. H. Moore, J. K. Olthoff and R. J. Van Brunt, "Electron scattering and dissociative attachment by sulfur hexafluoride and its electrical-discharge by-products," Plasma Chem. Plasma Process. 13, 1 (1993)

131. I. Sauers, L. G. Christophorou, and S. M. Spyrou, "Negative ion formation in compounds relevant to sulfur hexafluoride decomposition in electrical discharges," Plasma Chem. Plasma Process. 13, 17 (1993).

132. R. A. Morris, T. M. Miller, A. A. Viggiano, J. F. Paulson, S. Solomon and G. Reid, "Effects of electron and ion reactions on atmospheric lifetimes of fully fluorinated compounds," J. Geophys. Res. **100**, 1287 (1995).

133. D. E. Hunton, A. A. Viggiano, W. Swider, J. F. Paulson and C. Sherman, "Mass-spectrometric measurements of sulfur hexafluoride chemical releases from sounding rockets," J. Geophys. Res. 92, 8827 (1987).

134. D. M. Manos and D. L. Flamm, *Plasma Etching* (Academic Press, Boston, 1989).

135. L. E. Kline and M. J. Kushner, "Computer-simulation of materials processing plasma discharges," Crit. Rev. Solid State Mater. Sci **16**, 1 (1989).

136. R. E. Weston, Jr., "Electron capture by SF_6 and subsequent dissociation: a chemical activation mechanism," J. Phys. Chem. 99, 13150 (1995).

137. J. W. Gallagher, E. C. Beaty, J. Dutton and L. C. Pitchford, "An annotated compilation and appraisal of electron swarm data in electronegative gases," J. Phys. Chem. Ref. Data **12**, 109 (1983).

138. R. Reininger, E. Morikawa and V. Saile, "Polarization energy of an ion in a medium: benzene doped into rare gases," Chem. Phys. Lett. **159**, 276 (1989).

139. T. K. Bose, J. S. Sochanski and R. H. Cole, "Dielectric and pressure virial coefficients of imperfect gases. V. Octapole moments of methane and carbon tetrafluoride," J. Chem. Phys. **57**, 3592 (1972).

140. J. A. Tossell and J. W. Davenport, "MS-$X\alpha$ calculation of the elastic electron scattering cross-sections and x-ray absorption spectra of CX_4 and SiX_4 (X = H, F, Cl)," J. Chem. Phys. **80**, 813 (1984); Erratum **83**, 4824 (1985).

141. J. W. Davenport, W. Ho and J. R. Schrieffer, "Theory of vibrationally inelastic electron scattering from oriented molecules," Phys. Rev. B **17**, 3115 (1978).

142. L. Kevan and J. H. Futrell, "Determination of collision rate constants of fluorocarbon ions by ion cyclotron resonance," J. Chem. Soc. Faraday Trans. 2 **68**, 1742 (1972).

143. J. E. Sanabia, G. D. Cooper, J. A. Tossell and J. H. Moore, "Total electron scattering cross-sections for CHF_3, C_2F_6, C_3F_8 and *c*-C_4F_8," J. Chem. Phys. **108**, 389 (1998).

144. R. D. Nelson and R. H. Cole, "Dielectric properties of sulfur hexafluoride-chlorotrifluoromethane gas mixtures at nearly liquid densities," J. Chem. Phys. **54**, 4033 (1971).

145. D. Spence and G. J. Schulz, "Temperature dependence of electron attachment at low energies for polyatomic molecules," J. Chem. Phys. **58**, 1800 (1973), as quoted in [126].

146. K. Watanabe, "Photoionization and total absorption cross-section of gases. I. Ionization potentials of several molecules. Cross-sections of NH_3 and NO," J. Chem. Phys. **22**, 1564 (1954).

147. R. A. W. Johnstone and F. A. Mellon, "Electron-impact ionization and appearance potentials," J. Chem. Soc. Faraday Trans. 2 **68**, 1209 (1972).

148. S. Tsuda and W. H. Hamill, "Structure in ionization efficiency curves near threshold from alkanes and alkyl halides," J. Chem. Phys. **41**, 2713 (1964).

149. R. H. Martin, F. W. Lampe and R. W. Taft, "An electron-impact study of ionization and dissociation in methoxy- and halogen-substituted methanes," J. Am. Chem. Soc. **88**, 1353 (1966).

150. T. N. Olney, G. Cooper and C. E. Brion, "Quantitative studies of the photoabsorption (4.5–488 eV) and photoionization (9–59.5 eV) of methyl iodide using dipole electron impact techniques," Chem. Phys. **232**, 211 (1998).

151. A. P. Irsa, "Electron impact studies on C_2H_5Cl, C_2H_5Br and C_2H_5I," J. Chem. Phys. **26**, 18 (1957).

152. T. Baer, "Gas phase heats of formation of $C_2H_5^+$ and $C_3H_7^+$," J. Am. Chem. Soc. **102**, 2482 (1980).

153. T. M. Miller, R. A. Morris, A. E. S. Miller, A. A. Viggiano and J. F. Paulson, "Observation of Thermal Electron Detachment from cyclo-$C_4F_8^-$ in FALP Experiments," Int. J. Mass. Spectrom. Ion. Proc. **135**, 195 (1994).

154. P.S. Drzaic, J. Marks, J. I. Brauman, in *Gas Phase Ion Chemistry Vol. 3*, M. T. Bowers, ed. (Academic Press, Orlando, 1984), p. 167.

155. A. A. Maryott and F. Buckley, "Table of dielectric constants and electric dipole moments of substances in the gaseous state," U. S. NBS No. 537 (1953).

156. T. K. Bose and R. H. Cole, "Dielectric and pressure virial coefficients of imperfect gases. II. Carbon dioxide–argon mixtures," J. Chem. Phys. **52**, 140 (1970).

157. E. P. Grimsrud, S. Chowdhury and P. Kebarle, "Electron affinity of SF_6 and perfluoromethylcyclohexane. The unusual kinetics of electron transfer reactions $A^- + B^- + A$, where A = SF_6 or perfluorinated cycloalkanes," J. Chem. Phys. **85**, 4989 (1985).

Appendix 1. Energy Positions of High-*n* Rydberg States

A. Photoabsorption and Autoionization [14-16]

Table A1.1. *n*d and *n*d′ Rydberg state energies (eV) of C_2H_5I, as well as $I_1 \equiv I(\tilde{X}_1\ ^2E_{1/2})$ and $I_2 \equiv I(\tilde{X}_2\ ^2E_{1/2})$ obtained by fitting the assigned spectra (cf. Fig. 5.1) to the Rydberg equation, in selected Ar number densities ρ_{Ar} (10^{20} cm^{-3}). (The errors in the energies are ± 3 meV.)

ρ_{Ar}	10d	11d	12d	13d		I_1
0.024	9.123	9.169	9.204	9.231		9.348
0.13	9.122	9.168	9.203	9.230		9.347
0.24	9.121	9.167	9.203	9.229		9.346
0.66	9.120	9.165	9.201	9.227		9.345
1.2	9.117	9.163	9.199	9.223		9.340
2.4	9.110	9.158	9.194	9.218		9.336
3.8	9.104	9.149	9.186	9.215		9.329
4.9	9.100	9.146	9.183	9.207		9.324
ρ_{Ar}	10d′	11d′	12d′	13d′	14d′	I_2
0.024	9.704	9.753	9.787	9.813	9.834	9.931
0.13	9.704	9.752	9.786	9.812	9.833	9.930
0.24	9.703	9.751	9.785	9.811	9.832	9.929
0.66	9.701	9.750	9.784	9.810	9.831	9.928
1.2	9.697	9.747	9.780	9.806	9.828	9.923
2.4	9.691	9.741	9.775	9.801	9.823	9.918
3.8	9.684	9.736	9.769	9.794		9.912
4.9	9.677	9.729	9.763	9.789		9.909

Table A1.2. *n*d and *n*d′ Rydberg state energies (eV) of CH_3I, as well as $I_1 \equiv I(^2E_{3/2})$ and $I_2 \equiv I(^2E_{1/2})$ obtained by fitting the assigned spectra (cf. Fig. 5.3) to the Rydberg equation, in selected CF_4 number densities ρ_{CF_4} (10^{20} cm^{-3}). (The errors in the energies are ± 3 meV.)

ρ_{CF_4}	9d	10d	11d	12d	13d	14d	I_1
0.013	9.253	9.317	9.364	9.398	9.423	9.441	9.537
0.039	9.253	9.317	9.364	9.398	9.423	9.441	9.537
0.073	9.252	9.316	9.364	9.398	9.423	9.441	9.537
0.15	9.252	9.315	9.363	9.397	9.422	9.440	9.536
0.18	9.252	9.315	9.363	9.397	9.422	9.440	9.536
0.23	9.251	9.314	9.362	9.396	9.421	9.439	9.535
0.74	9.249	9.312	9.359	9.394	9.418	9.437	9.533
1.3	9.243	9.307	9.355	9.389	9.412	9.432	9.528
ρ_{CF_4}	9d′	10d′	11d′	12d′	13d′	14d′	I_2
0.013	9.867	9.938	9.986	10.021	10.046	10.065	10.163
0.039	9.867	9.938	9.986	10.021	10.046	10.065	10.163
0.073	9.867	9.938	9.985	10.021	10.045	10.065	10.163
0.15	9.866	9.938	9.984	10.020	10.044	10.064	10.162
0.18	9.866	9.937	9.984	10.020	10.044	10.064	10.162
0.23	9.865	9.936	9.983	10.019	10.043	10.063	10.161
0.74	9.862	9.934	9.980	10.016	10.040	10.060	10.159
1.3	9.856	9.925	9.974	10.010	10.035	10.055	10.155

Table A1.3 *n*d and *n*d′ Rydberg state energies (eV) of C_2H_5I, as well as $I_1 \equiv I(\tilde{X}_1\ ^2E_{1/2})$ and $I_2 \equiv I(\tilde{X}_2\ ^2E_{1/2})$ obtained by fitting the assigned spectra (cf. Fig. 5.3) to the Rydberg equation, in selected CF_4 number densities ρ_{CF_4} (10^{20} cm^{-3}). (The errors in the energies are ± 3 meV.)

ρ_{CF_4}	9d	10d	11d	12d	13d		I_1
0.24	9.050	9.120	9.168	9.202	9.228		9.346
1.2	9.043	9.113	9.160	9.195	9.221		9.339
2.4	9.034	9.104	9.151	9.185	9.211		9.329
4.6	9.014	9.083	9.130	9.152			9.309
6.1	9.000	9.070	9.117				9.296
ρ_{CF_4}	9d′	10d′	11d′	12d′	13d′	14d′	I_2
0.24	9.630	9.701	9.750	9.784	9.810	9.831	9.930
1.2	9.623	9.692	9.740	9.775	9.803	9.822	9.921
2.4	9.613	9.684	9.733	9.767	9.793	9.814	9.913
4.6	9.593	9.665	9.713	9.747	9.773		9.894
6.1	9.580	9.651	9.700				9.880

Table A1.4. *n*d′ Rydberg state energies (eV) of CH_3I, as well as $I_2 \equiv I(^2E_{1/2})$ obtained by fitting the assigned spectra (cf. Fig. 5.5) to the Rydberg equation, in selected *c*-C_4F_8 number densities $\rho_{c\text{-}C_4F_8}$ (10^{19} cm^{-3}). (The errors in the energies are ± 3 meV.)

$\rho_{c\text{-}C_4F_8}$	9d′	10d′	11d′	12d′	13d′	14d′	I_2
0.12	9.867	9.938	9.987	10.022	10.047	10.065	10.163
0.36	9.867	9.937	9.986	10.021	10.046	10.064	10.162
0.73	9.866	9.937	9.985	10.020	10.045	10.063	10.161
1.4	9.865	9.935	9.984	10.018	10.043	10.061	10.158
1.8	9.863	9.933	9.982	10.017	10.042	10.060	10.157
2.4	9.862	9.932	9.981	10.016	10.040	10.057	10.153

Table A1.5 *n*d′ Rydberg state energies (eV) of CH_3I, as well as $I_2 \equiv I(^2E_{1/2})$ obtained by fitting the assigned spectra (cf. Fig. 5.7) to the Rydberg equation, in selected SF_6 number densities ρ_{SF_6} (10^{19} cm^{-3}). (The errors in the energies are ± 3 meV.)

ρ_{SF_6}	9d′	10d′	11d′	12d′	I_2
0.12	9.868	9.938	9.988	10.022	10.164
0.96	9.867	9.937	9.987	10.022	10.162
2.0	9.866	9.936	9.986	10.020	10.162
5.0	9.863	9.933	9.980	10.013	10.153
9.8	9.856	9.923	9.968	10.002	10.139

B. Subthreshold Photoionization [14,17]

Table A1.6. *n*d Rydberg state energies (eV) of CH_3I, as well as $I_1 \equiv I(^2E_{3/2})$ obtained by fitting the assigned spectra (cf. Fig. 6.1a) to the Rydberg equation, in selected CF_4 number densities ρ_{CF_4} (10^{19} cm^{-3}). (The errors in the energies are ± 3 meV.)

ρ_{CF_4}	10d	11d	12d	13d	14d	I_1
0.12	9.325	9.370	9.402	9.425	9.443	9.538
0.49	9.325	9.369	9.401	9.425	9.443	9.538
0.97	9.324	9.369	9.401	9.424	9.442	9.537
1.3	9.324	9.369	9.400	9.424	9.442	9.537
1.8	9.323	9.368	9.400	9.423	9.441	9.536
2.4	9.323	9.368	9.399	9.423	9.441	9.536

Table A1.7. *n*d Rydberg state energies (eV) of CH_3I, as well as $I_1 \equiv I\ (^2E_{3/2})$ obtained by fitting the assigned spectra (cf. Fig. 6.2a) to the Rydberg equation, in selected *c*-C_4F_8 number densities $\rho_{c\text{-}C_4F_8}$ (10^{19} cm^{-3}). (The errors in the energies are ± 3 meV.)

$\rho_{c\text{-}C_4F_8}$	11d	12d	13d	14d	I_1
0.12	9.365	9.398	9.423	9.441	9.538
0.36	9.364	9.398	9.422	9.440	9.537
0.73	9.363	9.396	9.421	9.439	9.536
1.4	9.361	9.394	9.419	9.437	9.534
1.8	9.360	9.393	9.418	9.436	9.533
2.4	9.358	9.392	9.416	9.434	9.531

Table A1.8. *n*d Rydberg state energies (eV) of CH_3I, as well as $I_1 \equiv I\ (^2E_{3/2})$ obtained by fitting the assigned spectra (cf. Fig. 6.3a) to the Rydberg equation, in selected SF_6 number densities ρ_{SF_6} (10^{19} cm^{-3}). (The errors in the energies are ± 3 meV.)

ρ_{SF_6}	11d	12d	13d	14d	I_1
0.13	9.363	9.397	9.423	9.441	9.538
0.49	9.362	9.396	9.422	9.441	9.536
0.73	9.361	9.395	9.422	9.440	9.535
1.2	9.360	9.395	9.421		9.534
1.8	9.359	9.393	9.421		9.533
2.4	9.353	9.390	9.417		9.530

Table A1.9. *n*d Rydberg state energies (eV) of C_2H_5I, as well as $I_1 \equiv I\ (\tilde{X}_1\ ^2E_{3/2})$ obtained by fitting the assigned spectra (cf. Fig. 6.3b) to the Rydberg equation, in selected SF_6 number densities ρ_{SF_6} (10^{19} cm^{-3}). (The errors in the energies are ± 3 meV.)

ρ_{SF_6}	10d	11d	12d	13d	14d	I_1
0.12	9.122	9.171	9.203	9.228	9.249	9.349
0.49	9.120	9.169	9.203	9.227	9.249	9.348
0.73	9.119	9.167	9.201	9.226	9.248	9.347
1.5	9.117	9.166	9.200	9.225	9.246	9.346
2.2	9.116	9.165	9.198	9.223		9.343

Table A1.10. nR' Rydberg state energies (eV) of C_6H_6, as well as $I_1 \equiv I(^2E_{1g})$ obtained by fitting the assigned spectra (cf. Fig. 6.3c) to the Rydberg equation, in selected SF_6 number densities ρ_{SF_6} (10^{19} cm^{-3}). (The errors in the energies are ± 3 meV.)

ρ_{SF_6}	8R′	9R′	10R′	11R′	12R′	I_1
0.13	9.030	9.079	9.110	9.134	9.153	9.244
0.24	9.029	9.078	9.110	9.134	9.153	9.243
0.49	9.028	9.077	9.109	9.133	9.152	9.242
0.72	9.027	9.076	9.108	9.132	9.151	9.241
1.1	9.027	9.075	9.107	9.131	9.150	9.240
2.2	9.025	9.074	9.106	9.130		9.239

Appendix 2. Exponential Background Data from Subthreshold Photoionization

A. Regression Coefficients

Table A2.1. The regression coefficients χ for the exponential least-square fit (i.e., $e^{-\chi\Delta E}$) to the background of the CH_3I/P (P = Ar, CF_4, c-C_4F_8, CO_2, N_2 and SF_6) ionization threshold.

0.012×10^{-19} cm^{-3} CH_3I/0.49×10^{19} cm^{-3} Ar

Temperature (K)	χ (arbitrary units)	T χ (arbitrary units)
233	0.313	72.9
298	0.245	73.0
348	0.210	73.0

0.012×10^{-19} cm^{-3} CH_3I/0.72×10^{19} cm^{-3} CF_4

Temperature (K)	χ (arbitrary units)	T χ (arbitrary units)
276	0.261	72.0
298	0.243	72.3
353	0.208	72.2

0.00024×10^{-19} cm^{-3} CH_3I/0.72×10^{19} cm^{-3} c-C_4F_8

Temperature (K)	χ (arbitrary units)	T χ (arbitrary units)
300	0.247	74.1
320	0.232	74.2
354	0.209	74.0

0.012×10^{-19} cm^{-3} CH_3I/0.12×10^{19} cm^{-3} CO_2

Temperature (K)	χ (arbitrary units)	T χ (arbitrary units)
224	0.329	73.7
262	0.282	73.8
298	0.248	73.9
332	0.222	73.7
350	0.211	73.8

0.012×10^{-19} cm^{-3} CH_3I/0.72×10^{19} cm^{-3} N_2

Temperature (K)	χ (arbitrary units)	T χ (arbitrary units)
233	0.310	72.2
298	0.242	72.1
332	0.218	72.3

0.012×10^{-19} cm^{-3} CH_3I/0.12×10^{19} cm^{-3} SF_6

Temperature (K)	χ (arbitrary units)	T χ (arbitrary units)
243	0.307	74.6
273	0.274	74.8
301	0.248	74.6
332	0.224	74.5

B. Area of Exponential Background

Table A2.2. The area of the least-square fits to the exponential background of the threshold region of CH_3I perturbed by Ar, CF_4, *c*-C_4F_8, CO_2, N_2 and SF_6 at 298 K as a function of perturber number density ρ_P (10^{19} cm^{-3}). The CF_4 spectra and *c*-C_4F_8 spectra (cf. Appendix 2.A) used for this measurement were taken in Cell 1 with a resolutions of ~ 8 meV in the energy region of interest. All other spectra were taken in Cell 2 with a resolution of ~ 10 meV in the energy region of interest.

ρ_P	P =	Ar	CF_4	*c*-C_4F_8	CO_2	N_2	SF_6
0.12		8.4	8.4	8.4	8.4	8.4	8.4
0.24		8.5	—	—	—	8.5	8.5
0.36		—	—	8.6	8.6	—	—
0.39		—	8.7	—	—	—	—
0.49		8.7	—	—	—	8.7	8.7
0.73		8.9	8.8	8.9	8.8	8.9	8.9
0.98		—	—	—	—	—	9.0
1.1		—	—	—	9.1	—	—
1.2		9.2	—	—	—	9.2	9.3
1.5		—	9.4	9.4	9.4	—	—
1.8		—	9.7	9.7	—	—	—
2.3		—	10	10	—	10	—

Appendix 3. Subthreshold Photoionization Peak Areas

A. C_2H_5I/SF_6 [14,20]

Table A3.1. Peak areas (by gaussian fits to the photoionization spectra) for the subthreshold photoionization structure of 0.00024 x 10^{19} cm^{-3} C_2H_5I in varying SF_6 number densities ρ_{SF_6} (10^{19} cm^{-3}).

ρ_{SF_6}	10d	11d	12d	13d	14d
0.12	0.0031	0.0065	0.013	0.021	0.028
0.63	0.0067	0.012	0.022	0.034	0.049
0.98	0.0093	0.015	0.028	0.043	0.063
1.3	0.012	0.019	0.034	0.053	0.078
1.8	0.015	0.024	0.042	0.066	0.098
2.4	0.020	0.030	0.052	0.081	0.12
Regression coefficients					
b_0	0.0022	0.0053	0.011	0.018	0.023
b_1	0.0072	0.010	0.017	0.026	0.041

The regression coefficients b_0 and b_1 were determined by least-square linear fits to Eq. (6.13).

Table A3.2. Peak areas (by gaussian fits to the photoionization spectra) for the subthreshold photoionization structure of 0.012 x 10^{19} cm^{-3} C_2H_5I in varying SF_6 number densities ρ_{SF_6} (10^{19} cm^{-3}).

ρ_{SF_6}	10d	11d	12d	13d	14d
0.12	0.013	0.043	0.075	0.11	0.15
0.63	0.020	0.067	0.12	0.20	0.31
0.98	0.025	0.083	0.15	0.27	0.42
1.3	0.030	0.10	0.19	0.33	0.52
1.8	0.037	0.12	0.23	0.42	
2.4	0.046	0.15	0.29	0.52	
Regression coefficients					
b_0	0.011	0.037	0.064	0.091	0.12
b_1	0.014	0.047	0.091	0.18	0.30

The regression coefficients b_0 and b_1 were determined by least-square linear fits to Eq. (6.13).

Table A3.3. Peak areas (by gaussian fits to the photoionization spectra) for the subthreshold photoionization structure of 0.061 x 10^{19} cm^{-3} C_2H_5I in varying SF_6 number densities ρ_{SF_6} (10^{19} cm^{-3}).

ρ_{SF_6}	10d	11d	12d	13d	14d
0.12	0.065	0.22	0.38	0.57	0.78
0.63	0.10	0.34	0.62	1.0	1.6
0.98	0.13	0.42	0.78	1.3	2.1
1.3	0.15	0.51	0.94	1.7	2.7
1.8	0.19	0.63	1.2	2.1	
2.4	0.23	0.77	1.5	2.7	
Regression coefficients					
b_0	0.056	0.19	0.32	0.46	0.60
b_1	0.073	0.24	0.46	0.92	1.6

The regression coefficients b_0 and b_1 were determined by least-square linear fits to Eq. (6.13).

Table 3.4. Peak areas (by gaussian fits to the photoionization spectra) for the subthreshold photoionization structure of 0.12 x 10^{19} cm^{-3} C_2H_5I in varying SF_6 number densities ρ_{SF_6} (10^{19} cm^{-3}).

ρ_{SF_6}	10d	11d	12d	13d	14d
0.12	0.13	0.43	0.75	1.1	1.6
0.63	0.20	0.67	1.2	2.0	3.1
0.98	0.25	0.83	1.5	2.6	4.0
1.3	0.30	1.0	1.9	3.3	5.2
1.8	0.37	1.2	2.3	4.2	
2.4	0.46	1.5	2.9		
Regression coefficients					
b_0	0.11	0.37	0.63	0.91	1.2
b_1	0.14	0.45	0.91	1.7	3.0

The regression coefficients b_0 and b_1 were determined by least-square linear fits to Eq. (6.13).

Table A3.5. Peak areas (by gaussian fits to the photoionization spectra) for the subthreshold photoionization structure of 0.37 x 10^{19} cm^{-3} C_2H_5I in varying SF_6 number densities ρ_{SF_6} (10^{19} cm^{-3}).

ρ_{SF_6}	10d	11d	12d	13d
0.12	0.39	1.3	2.3	3.5
0.63	0.62	2.1	3.7	6.2
0.98	0.77	2.6	4.7	8.2
1.3	0.93	3.1	5.7	10
1.8	1.1	3.8	7.1	
2.4	1.4	4.7	8.8	
Regression coefficients				
b_0	0.34	1.2	2.0	2.8
b_1	0.44	1.4	2.8	5.5

The regression coefficients b_0 and b_1 were determined by least-square linear fits to Eq. (6.13).

B. C_6H_6/SF_6 [14,20]

Table A3.6. Peak areas (by gaussian fits to the photoionization spectra) for the subthreshold photoionization structure of 0.0024 x 10^{19} cm^{-3} C_6H_6 in varying SF_6 number densities ρ_{SF_6} (10^{19} cm^{-3}).

ρ_{SF_6}	8R′	9R′	10R′	11R′	12R′
0.12	0.0012	0.0063	0.011	0.016	0.022
0.63	0.0013	0.0084	0.015	0.023	0.034
0.98	0.0014	0.0098	0.017	0.027	0.043
1.3	0.0015	0.011	0.020	0.031	0.051
1.8	0.0016	0.013	0.024	0.037	0.063
2.4	0.0017	0.016	0.029	0.044	
Regression coefficients					
b_0	0.0012	0.0058	0.010	0.015	0.019
b_1	0.00021	0.0041	0.0076	0.012	0.024

The regression coefficients b_0 and b_1 were determined by least-square linear fits to Eq. (6.13).

Table A3.7. Peak areas (by gaussian fits to the photoionization spectra) for the subthreshold photoionization structure of 0.012 x 10^{19} cm^{-3} C_6H_6 in varying SF_6 number densities ρ_{SF_6} (10^{19} cm^{-3}).

ρ_{SF_6}	8R′	9R′	10R′	11R′	12R′
0.12	0.0061	0.030	0.054	0.080	0.11
0.63	0.0063	0.034	0.066	0.11	0.16
0.98	0.0065	0.037	0.074	0.12	0.19
1.3	0.0066	0.039	0.082	0.14	0.22
1.8	0.0069	0.043	0.092	0.16	0.27
2.4	0.0071	0.048	0.11	0.19	
Regression coefficients					
b_0	0.0060	0.029	0.051	0.074	0.097
b_1	0.00047	0.0079	0.022	0.049	0.094

The regression coefficients b_0 and b_1 were determined by least-square linear fits to Eq. (6.13).

Table A3.8. Peak areas (by gaussian fits to the photoionization spectra) for the subthreshold photoionization structure of 0.063 x 10^{19} cm^{-3} C_6H_6 in varying SF_6 number densities ρ_{SF_6} (10^{19} cm^{-3}).

ρ_{SF_6}	8R′	9R′	10R′	11R′	12R′
0.12	0.032	0.16	0.29	0.42	0.57
0.63	0.033	0.18	0.35	0.55	0.82
0.98	0.034	0.19	0.39	0.64	0.99
1.3	0.035	0.21	0.43	0.73	1.2
1.8	0.036	0.23	0.48	0.86	
2.4	0.037	0.25	0.56	1.0	
Regression coefficients					
b_0	0.032	0.15	0.26	0.39	0.51
b_1	0.0025	0.041	0.12	0.25	0.49

The regression coefficients b_0 and b_1 were determined by least-square linear fits to Eq. (6.13).

Table A3.9. Peak areas (by gaussian fits to the photoionization spectra) for the subthreshold photoionization structure of 0.12 x 10^{19} cm^{-3} C_6H_6 in varying SF_6 number densities ρ_{SF_6} (10^{19} cm^{-3}).

ρ_{SF_6}	8R′	9R′	10R′	11R′	12R′
0.12	0.061	0.30	0.54	0.80	1.1
0.63	0.063	0.33	0.66	1.0	1.5
0.98	0.065	0.37	0.74	1.2	1.9
1.3	0.066	0.39	0.81	1.4	2.2
1.8	0.069	0.43	0.92	1.6	
2.4	0.071	0.48	1.1		
Regression coefficients					
b_0	0.061	0.29	0.51	0.74	0.97
b_1	0.0047	0.079	0.23	0.48	0.94

The regression coefficients b_0 and b_1 were determined by least-square linear fits to Eq. (6.13).

Table A3.10. Peak areas (by gaussian fits to the photoionization spectra) for the subthreshold photoionization structure of 0.24 x 10^{19} cm^{-3} C_6H_6 in varying SF_6 number densities ρ_{SF_6} (10^{19} cm^{-3}).

ρ_{SF_6}	8R′	9R′	10R′	11R′	12R′
0.12	0.12	0.59	1.2	1.5	2.2
0.63	0.13	0.67	1.4	2.0	3.1
0.98	0.13	0.73	1.5	2.4	3.8
1.3	0.13	0.78	1.7	2.7	
1.8	0.14	0.86	1.9		
2.4	0.14	0.96	2.2		
Regression coefficients					
b_0	0.12	0.57	1.1	1.4	2.0
b_1	0.0094	0.16	0.44	0.98	1.8

The regression coefficients b_0 and b_1 were determined by least-square linear fits to Eq. (6.13).

C. CH_3I/P

i. CH_3I/Ar [18,20]

Table A3.11. Peak areas (by gaussian fits to the photoionization spectra) for the subthreshold photoionization structure of 0.012 x 10^{19} cm^{-3} CH_3I in varying Ar number densities ρ_{Ar} (10^{19} cm^{-3}).

ρ_{Ar}	10d	11d	12d	13d	14d
0.00	0.00	0.0074	0.012	0.018	0.024
0.12	0.00	0.0075	0.012	0.018	0.024
0.63	0.00	0.0077	0.013	0.018	0.024
0.98	0.00	0.0078	0.013	0.019	0.025
1.3	0.00	0.0079	0.013	0.019	0.025
Regression coefficients					
b_0	0.00	0.0074	0.012	0.018	0.024
b_1	0.00	0.00035	0.00036	0.00040	0.00057

The regression coefficients b_0 and b_1 were determined by least-square linear fits to Eq. (6.13).

Table A3.12. Peak areas (by gaussian fits to the photoionization spectra) for the subthreshold photoionization structure of 0.061 x 10^{19} cm^{-3} CH_3I in varying Ar number densities ρ_{Ar} (10^{19} cm^{-3}).

ρ_{Ar}	10d	11d	12d	13d	14d
0.00	0.014	0.049	0.084	0.13	0.20
0.12	0.015	0.050	0.086	0.13	0.20
0.63	0.019	0.055	0.090	0.14	0.20
0.98	0.022	0.058	0.094	0.14	0.21
1.3	0.025	0.061	0.097	0.15	0.21
Regression coefficients					
b_0	0.013	0.049	0.084	0.11	0.19
b_1	0.0087	0.0089	0.0095	0.011	0.012

The regression coefficients b_0 and b_1 were determined by least-square linear fits to Eq. (6.13).

Table A3.13. Peak areas (by gaussian fits to the photoionization spectra) for the subthreshold photoionization structure of 0.12 x 10^{19} cm^{-3} CH_3I in varying Ar number densities ρ_{Ar} (10^{19} cm^{-3}).

ρ_{Ar}	10d	11d	12d	13d	14d
0.00	0.040	0.14	0.22	0.36	0.56
0.12	0.044	0.15	0.22	0.37	0.56
0.63	0.061	0.17	0.24	0.39	0.58
0.98	0.073	0.18	0.25	0.40	0.60
1.3	0.085	0.19	0.27	0.42	0.62
Regression coefficients					
b_0	0.040	0.14	0.22	0.37	0.56
b_1	0.033	0.035	0.037	0.039	0.045

The regression coefficients b_0 and b_1 were determined by least-square linear fits to Eq. (6.13).

Table A3.14. Peak areas (by gaussian fits to the photoionization spectra) for the subthreshold photoionization structure of 0.37 x 10^{19} cm^{-3} CH_3I in varying Ar number densities ρ_{Ar} (10^{19} cm^{-3}).

ρ_{Ar}	10d	11d	12d	13d
0.00	0.21	0.73	1.4	2.4
0.12	0.25	0.77	1.5	2.5
0.63	0.41	0.93	1.7	2.7
0.98	0.52	1.1	1.8	2.8
1.3	0.64	1.2	1.9	2.9
Regression coefficients				
b_0	0.21	0.73	1.4	2.4
b_1	0.32	0.33	0.35	0.38

The regression coefficients b_0 and b_1 were determined by least-square linear fits to Eq. (6.13).

ii. CH_3I/CF_4 [19]

Table A3.15. Peak areas (by gaussian fits to the photoionization spectra) for the subthreshold photoionization structure of 0.012 x 10^{19} cm^{-3} CH_3I in varying CF_4 number densities ρ_{CF_4} (10^{19} cm^{-3}).

ρ_{CF_4}	10d	11d	12d	13d	14d
0.12	0.00	0.0076	0.012	0.017	0.024
0.49	0.00	0.0080	0.013	0.018	0.024
0.97	0.00	0.0083	0.013	0.018	0.025
1.3	0.00	0.0086	0.014	0.019	0.025
1.8	0.00	0.0090	0.014	0.019	0.026
2.4	0.00	0.0094	0.015	0.020	0.026
Regression coefficients					
b_0	0.00	0.0075	0.012	0.018	0.024
b_1	0.00	0.00082	0.00087	0.00094	0.0010

The regression coefficients b_0 and b_1 were determined by least-square linear fits to Eq. (6.13).

Table A3.16. Peak areas (by gaussian fits to the photoionization spectra) for the subthreshold photoionization structure of 0.061 x 10^{19} cm^{-3} CH_3I in varying CF_4 number densities ρ_{CF_4} (10^{19} cm^{-3}).

ρ_{CF_4}	10d	11d	12d	13d	14d
0.12	0.016	0.052	0.088	0.14	0.20
0.49	0.023	0.059	0.098	0.14	0.21
0.97	0.033	0.070	0.11	0.15	0.22
1.3	0.041	0.077	0.12	0.16	0.23
1.8	0.051	0.088	0.13	0.18	0.25
2.4	0.062	0.10	0.15	0.20	0.26
Regression coefficients					
b_0	0.014	0.048	0.086	0.13	0.20
b_1	0.021	0.023	0.024	0.026	0.029

The regression coefficients b_0 and b_1 were determined by least-square linear fits to Eq. (6.13).

Table A3.17. Peak areas (by gaussian fits to the photoionization spectra) for the subthreshold photoionization structure of 0.12 x 10^{19} cm^{-3} CH_3I in varying CF_4 number densities ρ_{CF_4} (10^{19} cm^{-3}).

ρ_{CF_4}	10d	11d	12d	13d	14d
0.12	0.044	0.13	0.24	0.37	0.57
0.49	0.073	0.16	0.26	0.41	0.60
0.97	0.11	0.21	0.31	0.46	0.66
1.3	0.15	0.23	0.34	0.49	0.69
1.8	0.18	0.27	0.38	0.53	
2.4	0.23	0.32	0.44	0.58	
Regression coefficients					
b_0	0.035	0.12	0.22	0.36	0.55
b_1	0.080	0.083	0.089	0.095	0.11

The regression coefficients b_0 and b_1 were determined by least-square linear fits to Eq. (6.13).

Table A3.18. Peak areas (by gaussian fits to the photoionization spectra) for the subthreshold photoionization structure of 0.37 x 10^{19} cm^{-3} CH_3I in varying CF_4 number densities ρ_{CF_4} (10^{19} cm^{-3}).

ρ_{CF_4}	10d	11d	12d	13d	14d
0.12	0.31	0.81	1.5	2.5	4.1
0.49	0.59	1.1	1.8	2.8	4.4
0.97	0.95	1.5	2.2	3.3	4.9
1.3	1.2	1.8	2.5	3.6	5.3
1.8	1.6	2.1	2.9	4.1	
2.4	2.0	2.6	3.4	4.6	
Regression coefficients					
b_0	0.22	0.71	1.4	2.4	4.0
b_1	0.76	0.79	0.83	0.92	0.99

The regression coefficients b_0 and b_1 were determined by least-square linear fits to Eq. (6.13).

iii. CH_3I/CO_2 and N_2 [18]

Table A3.19. Peak areas (by gaussian fits to the photoionization spectra) for the subthreshold photoionization structure of 0.012 x 10^{19} cm^{-3} CH_3I in varying CO_2 number densities ρ_{CO_2} (10^{19} cm^{-3}).

ρ_{CO_2}	10d	11d	12d	13d	14d
0.12	0.00	0.0076	0.012	0.018	0.022
0.36	0.00	0.0077	0.013	0.019	0.023
0.73	0.00	0.079	0.013	0.019	0.023
1.1	0.00	0.082	0.014	0.020	0.024
1.5	0.00	0.084	0.014	0.020	
Regression coefficients					
b_0	0.00	0.0075	0.012	0.018	0.023
b_1	0.00	0.00062	0.00066	0.00072	0.00079

The regression coefficients b_0 and b_1 were determined by least-square linear fits to Eq. (6.13).

Table A3.20. Peak areas (by gaussian fits to the photoionization spectra) for the subthreshold photoionization structure of 0.012 x 10^{19} cm^{-3} CH_3I in varying N_2 number densities ρ_{N_2} (10^{19} cm^{-3}).

ρ_{N_2}	10d	11d	12d	13d	14d
0.12	0.00	0.0075	0.012	0.018	0.022
0.25	0.00	0.0076	0.012	0.018	0.022
0.49	0.00	0.0077	0.013	0.019	0.023
0.73	0.00	0.0078	0.013	0.019	0.023
1.2	0.00	0.0079	0.014	0.020	0.024
2.5	0.00	0.0084	0.014	0.020	
Regression coefficients					
b_0	0.00	0.0075	0.012	0.019	0.023
b_1	0.00	0.0037	0.0042	0.0045	0.0048

The regression coefficients b_0 and b_1 were determined by least-square linear fits to Eq. (6.13).

iv. $CH_3I/c\text{-}C_4F_8$ [19]

Table A3.21. Peak areas (by gaussian fits to the photoionization spectra) for the subthreshold photoionization structure of 0.00024 x 10^{19} cm^{-3} CH_3I in varying $c\text{-}C_4F_8$ number densities $\rho_{c\text{-}C_4F_8}$ (10^{19} cm^{-3}).

$\rho_{c\text{-}C_4F_8}$	10d	11d	12d	13d	14d
0.12	0.00	0.0063	0.010	0.016	0.022
0.36	0.00	0.0077	0.013	0.021	0.032
0.72	0.00	0.010	0.018	0.030	0.046
1.4	0.00	0.014	0.027	0.047	0.076
1.8	0.00	0.017	0.031	0.056	0.092
2.4	0.00	0.021	0.039	0.071	0.12
Regression coefficients					
b_0	0.00	0.0055	0.0090	0.013	0.017
b_1	0.00	0.0061	0.012	0.024	0.041

The regression coefficients b_0 and b_1 were determined by least-square linear fits to Eq. (6.13).

Table A3.22. Peak areas (by gaussian fits to the photoionization spectra) for the subthreshold photoionization structure of 0.012 x 10^{19} cm^{-3} CH_3I in varying $c\text{-}C_4F_8$ number densities $\rho_{c\text{-}C_4F_8}$ (10^{19} cm^{-3}).

$\rho_{c\text{-}C_4F_8}$	10d	11d	12d	13d	14d
0.12	0.0089	0.032	0.054	0.080	0.11
0.36	0.012	0.040	0.068	0.11	0.16
0.72	0.015	0.051	0.091	0.15	0.24
1.4	0.023	0.075	0.14	0.24	0.39
1.8	0.027	0.086	0.16	0.29	0.46
2.4	0.034	0.11	0.20	0.36	0.59
Regression coefficients					
b_0	0.0075	0.028	0.046	0.065	0.086
b_1	0.011	0.033	0.064	0.12	0.21

The regression coefficients b_0 and b_1 were determined by least-square linear fits to Eq. (6.13).

Table A3.23. Peak areas (by gaussian fits to the photoionization spectra) for the subthreshold photoionization structure of 0.061 x 10^{19} cm^{-3} CH_3I in varying c-C_4F_8 number densities $\rho_{c\text{-}C_4F_8}$ (10^{19} cm^{-3}).

$\rho_{c\text{-}C_4F_8}$	10d	11d	12d	13d	14d
0.12	0.052	0.18	0.30	0.45	0.65
0.36	0.071	0.22	0.38	0.61	0.91
0.72	0.10	0.29	0.51	0.84	1.3
1.4	0.16	0.43	0.76	1.3	2.1
1.8	0.19	0.50	0.89	1.6	2.5
2.4	0.24	0.62	1.1	2.0	3.2
Regression coefficients					
b_0	0.041	0.15	0.26	0.37	0.51
b_1	0.084	0.19	0.35	0.66	1.1

The regression coefficients b_0 and b_1 were determined by least-square linear fits to Eq. (6.13).

Table A3.24. Peak areas (by gaussian fits to the photoionization spectra) for the subthreshold photoionization structure of 0.12 x 10^{19} cm^{-3} CH_3I in varying c-C_4F_8 number densities $\rho_{c\text{-}C_4F_8}$ (10^{19} cm^{-3}).

$\rho_{c\text{-}C_4F_8}$	10d	11d	12d	13d	14d
0.12	0.12	0.38	0.65	1.0	1.5
0.36	0.17	0.49	0.83	1.3	2.0
0.72	0.25	0.65	1.1	1.8	2.8
1.4	0.42	0.97	1.6	2.8	4.4
1.8	0.50	1.1	1.9	3.3	5.2
2.4	0.64	1.4	2.4	4.1	6.6
Regression coefficients					
b_0	0.090	0.33	0.56	0.83	1.2
b_1	0.23	0.45	0.76	1.4	2.3

The regression coefficients b_0 and b_1 were determined by least-square linear fits to Eq. (6.13).

Table A3.25. Peak areas (by gaussian fits to the photoionization spectra) for the subthreshold photoionization structure of 0.37 x 10^{19} cm^{-3} CH_3I in varying c-C_4F_8 number densities $\rho_{c\text{-}C_4F_8}$ (10^{19} cm^{-3}).

$\rho_{c\text{-}C_4F_8}$	10d	11d	12d	13d	14d
0.12	0.57	1.6	2.8	4.5	6.9
0.49	0.94	2.2	3.6	5.7	8.8
0.97	1.5	3.0	4.7	7.6	12
1.3	2.6	4.6	7.0	11	17
1.8	3.2	5.4	8.2	13	
2.4	3.7	6.7	10	16	
Regression coefficients					
b_0	0.46	1.4	2.4	3.9	5.8
b_1	1.4	2.3	3.2	5.2	8.2

The regression coefficients b_0 and b_1 were determined by least-square linear fits to Eq. (6.13).

v. CH_3I/SF_6 [17,20]

Table A3.26. Peak areas (by gaussian fits to the photoionization spectra) for the subthreshold photoionization structure of 0.00024 x 10^{19} cm^{-3} CH_3I in varying SF_6 number densities ρ_{SF_6} (10^{19} cm^{-3}).

ρ_{SF_6}	10d	11d	12d	13d	14d
0.12	0.0017	0.0036	0.012	0.021	0.032
0.63	0.0043	0.0086	0.023	0.038	0.066
0.98	0.0065	0.011	0.028	0.047	0.084
1.3	0.0087	0.015	0.034	0.061	0.10
1.8	0.011	0.021	0.044	0.075	0.12
2.4	0.016	0.026	0.055	0.092	0.17
Regression coefficients					
b_0	0.0010	0.0025	0.0094	0.018	0.025
b_1	0.0056	0.0095	0.019	0.031	0.060

The regression coefficients b_0 and b_1 were determined by least-square linear fits to Eq. (6.13).

Table A3.27. Peak areas (by gaussian fits to the photoionization spectra) for the subthreshold photoionization structure of 0.012 x 10^{19} cm^{-3} CH_3I in varying SF_6 number densities ρ_{SF_6} (10^{19} cm^{-3}).

ρ_{SF_6}	10d	11d	12d	13d	14d
0.12	0.013	0.047	0.078	0.12	0.16
0.63	0.019	0.067	0.12	0.19	0.28
0.98	0.024	0.080	0.14	0.24	0.37
1.3	0.028	0.094	0.17	0.29	0.46
1.8	0.034	0.11	0.20	0.36	0.58
2.4	0.042	0.14	0.25	0.45	0.73
Regression coefficients					
b_0	0.011	0.042	0.069	0.098	0.13
b_1	0.013	0.039	0.074	0.14	0.25

The regression coefficients b_0 and b_1 were determined by least-square linear fits to Eq. (6.13).

Table A3.28. Peak areas (by gaussian fits to the photoionization spectra) for the subthreshold photoionization structure of 0.0061 x 10^{19} cm^{-3} CH_3I in varying SF_6 number densities ρ_{SF_6} (10^{19} cm^{-3}).

ρ_{SF_6}	10d	11d	12d	13d	14d
0.12	0.071	0.25	0.42	0.63	0.87
0.63	0.12	0.37	0.63	1.0	1.5
0.98	0.15	0.44	0.77	1.3	2.0
1.3	0.18	0.52	0.91	1.6	2.4
1.8	0.22	0.63	1.1	1.9	3.1
2.4	0.28	0.77	1.4	2.4	3.8
Regression coefficients					
b_0	0.060	0.23	0.37	0.54	0.72
b_1	0.090	0.25	0.40	0.71	1.3

The regression coefficients b_0 and b_1 were determined by least-square linear fits to Eq. (6.13).

Table A3.29. Peak areas (by gaussian fits to the photoionization spectra) for the subthreshold photoionization structure of 0.12 x 10^{19} cm^{-3} CH_3I in varying SF_6 number densities ρ_{SF_6} (10^{19} cm^{-3}).

ρ_{SF_6}	10d	11d	12d	13d	14d
0.12	0.15	0.53	0.88	1.4	1.9
0.49	0.27	0.78	1.3	2.1	2.7
0.97	0.35	0.96	1.6	2.7	4.1
1.3	0.44	1.1	1.9	3.3	5.0
1.8	0.55	1.4	2.3	4.0	
2.4	0.69	1.7	2.9	5.0	
Regression coefficients					
b_0	0.13	0.43	0.77	1.2	1.6
b_1	0.20	0.50	0.83	1.6	2.6

The regression coefficients b_0 and b_1 were determined by least-square linear fits to Eq. (6.13).

Table A3.30. Peak areas (by gaussian fits to the photoionization spectra) for the subthreshold photoionization structure of 0.37 x 10^{19} cm^{-3} CH_3I in varying SF_6 number densities ρ_{SF_6} (10^{19} cm^{-3}).

ρ_{SF_6}	10d	11d	12d	13d
0.12	0.67	2.1	3.5	5.6
0.49	1.4	3.3	5.3	8.5
0.97	1.9	4.1	6.5	10
1.3	2.5	4.9	7.7	13
1.8	3.2	6.0	9.4	
2.4	4.1	7.4	12	
Regression coefficients				
b_0	0.49	1.8	3.1	4.9
b_1	1.5	2.3	3.5	5.7

The regression coefficients b_0 and b_1 were determined by least-square linear fits to Eq. (6.13).

Vita

Cherice Marie Evans was born on November 8, 1975, in Baytown, Texas, and is the only child of James E. Evans and Nita B. Evans. She moved to Negreet, Louisiana, when she was five years old and graduated from Florien High School (Florien, Louisiana) in 1993. She then matriculated at the University of Louisiana at Monroe (Monroe, Louisiana) [formerly Northeast Louisiana University] on scholarship and received the bachelor of science degree in chemistry in December 1996. During this time she began to do research with Dr. Gary L. Findley (Professor of Chemistry, University of Louisiana at Monroe), and chose to continue her studies at the University of Louisiana at Monroe for the master of science degree in chemistry. On receiving this degree in May 1998, for a thesis entitled *Analytic Solutions to the Lotka-Volterra Model for Sustained Chemical Oscillations*, she chose to pursue the doctor of philosophy degree in chemistry at Louisiana State University under the direction of Dr. John D. Scott (Adjunct Professor of Chemistry, Louisiana State University), and with the continued guidance of Dr. Gary L. Findley. She passed her general examinations during the Fall term 1999 and is currently a candidate for the degree of Doctor of Philosophy in chemistry.

DOCTORAL EXAMINATION AND DISSERTATION REPORT

Candidate: Cherice Marie Evans

Major Field: Chemistry

Title of Dissertation: Subthreshold Photoionization in Molecular Dopant/ Perturber Systems

Approved:

John D Scott
Major Professor and Chairman

Dean of the Graduate School

EXAMINING COMMITTEE:

Neil R. Keates

J Marcos Fernandez

Erwin D Poliakoff

Sean P. McGlynn

Date of Examination:

February 14, 2001